SYNTHESIS, ELECTRICAL CONDUCTIVITY AND

NONSTOICHIOMETRY OF DOPED LAYERED

PEROVSKITES

by

Carlos Justo Navas Pérez

B.A., Chemistry and Mathematics

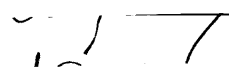Clark University, Worcester, Massachusetts (1993)

SUBMITTED TO THE DEPARTMENT OF CHEMISTRY

IN PARTIAL FULFILLMENT OF THE REQUIREMENTS

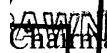FOR THE DEGREE OF DOCTOR OF PHILOSOPHY

at the

MASSACHUSETTS INSTITUTE OF TECHNOLOGY

February 1999

© 1999 Massachusetts Institute of Technology

Signature of Author _____

Department of Chemistry
January 13, 1999

Certified by _____

Prof. Harry L. Tuller
Thesis Supervisor

Accepted by _____

MASSACHUSETTS INSTITUTE

Prof. Dietmar Seyferth
Chairman, Departmental Committee on Graduate Students

Science

This doctoral thesis has been examined by a Committee of the Department of Chemistry as follows:

Prof. Dietmar Seyferth _____
Chairman

Prof. Harry L. Tuller_____
Thesis Supervisor

Prof. Alan Davison_____

SYNTHESIS, ELECTRICAL CONDUCTIVITY AND NONSTOICHIOMETRY OF DOPED LAYERED PEROVSKITES

by

Carlos Justo Navas Pérez

SUBMITTED TO THE DEPARTMENT OF CHEMISTRY
IN PARTIAL FULFILLMENT OF THE REQUIREMENTS
FOR THE DEGREE OF DOCTOR OF PHILOSOPHY

at the

MASSACHUSETTS INSTITUTE OF TECHNOLOGY

February 1999

ABSTRACT

As part of an ongoing study of alternative electrolyte and electrode materials to serve as components in Solid Oxide Fuel Cells, a series of doped layered perovskites, of general formula $Sr_3Ti_{2-x}M_xO_{7-\delta}$ (M=Al, Ga, In, Co, Fe, Mn), were synthesized and their electrical conductivity characterized as a function of temperature and oxygen partial pressure. For fixed-valent dopants, p-type conductivity predominates at $p(O_2) > 10^{-5}$ atm, followed by a $p(O_2)$-independent electrolytic regime, and n-type electronic conductivity at very low $p(O_2)$. The electrolytic regime exhibits low magnitudes of oxygen ion conductivity (ca. 10^{-6} S/cm at 700 °C) and high activation energies (1.4-1.5 eV). Solid solutions with transition metals display significantly higher conductivities. For M= Co, a p-type conductivity region at high $p(O_2)$ is observed, followed by an ionic regime at intermediate $p(O_2)$ characterized by high ionic conductivity (10^{-2} S/cm at 700 °C for $Sr_3Ti_{1.2}Co_{0.8}O_{7-\delta}$) and low activation energy (0.64 eV). The magnitude of the conductivity increases with increasing Co content. Iodometric titration measurements demonstrate the predominance of Co(IV) in air. The identification of the electrolytic regime is

also corroborated by measurements of the chemical diffusion coefficient at high $p(O_2)$'s. For M= Fe, the trend is similar, except that the conductivity shows no dependence on Fe content. The electrical conductivity for M=Co, Fe is explained and modeled by an isolated-defect chemical model. In contrast, for M= Mn, the conductivity shows a slight increase, reaches a maximum and then decreases with decreasing $p(O_2)$. This behavior points to the importance of electronic conductivity in the Mn defect band.

Thesis Supervisor: Prof. Harry L. Tuller

Title: Professor of Ceramics and Electronic Materials

Acknowledgments

I would like to thank Prof. Hanno zur Loye for taking me into his group and providing me with the opportunity to carry out fun and challenging research in his lab. I came into his group not knowing a thing about solid state chemistry and the three years I spent under his supervision were an outstanding learning experience.

I am indebted to Prof. Harry Tuller for a number of things. First, he was willing to take me under his wing on very short notice and welcomed me into his group with open arms. Secondly, I feel my experience as a graduate student at MIT would not have been the same without the perspective from a materials scientist and defect chemist-specialist such as he.

Past and present members of the zur Loye and Tuller groups, in general, were instrumental at one time or another in helping me along the way, and they are too numerous to mention each by name. In particular, Kurt Kendall guided me during the first part of my thesis work and taught me much about oxygen ion conductivity, both in theory and practice. His patience and continuous explanations and help deserve special recognition here. Jason Sprague and Ofer Porat also helped me a lot at the beginning of my tenure in the Tuller group. The insight of Dirk Wilmer on the iodometric titration measurements is also very much appreciated.

I have had the luck of sharing my graduate experience with a number of students that made it all a lot of fun. They were simply wonderful people with whom I shared the good, the bad and the ugly. Dave Bem, Kurt Kendall, Joel Houmes, Jennifer Pell and Hans Olsen provided companionship during lunch hour, insight into American culture, and some great stories I will never forget. Jason Sprague taught me that the USA is all about "convenience", and has been a

7

friend throughout the years in the Tuller group. Also Greg Farrey and Sossity Sheets, with whom I shared an office, were always welcome friendly faces.

I have also been lucky in that I have been able to enjoy life outside of the lab, something no graduate student should do without. Kurt, Dave, Ron Gal and Hans Olsen were kind enough to show me the Boston bar scene after getting a few free beers courtesy of Dave at the Thirsty Ear. My roommates Jed Goldstone, Chris Long (Stoph) and Chris Morse were always very entertaining and provided a fun and relaxing atmosphere at home.

I really do not know where I would be without Giovanna. During the last 3 years, she was there for me in every way someone can be there for someone else. At the very least, I owe her my sanity during all those times that I was frustrated with lab work, and they were not just a few. She is, without a doubt, the best that has ever happened to me. Te quiero. Baci.

Por último, a mis padres les debo el haberme dado la oportunidad de llegar hasta aquí. Dudo que haya muchos padres que se separen de su único hijo durante 10 años (y suma y sigue), hagan todos los sacrificios que ellos han hecho, con tal de darme una buena educación. No os podéis imaginar lo orgulloso que estoy de vosotros. Os quiero.

Table of Contents

Table of Figures

13

A mis padres

Por haberme guiado en el camino de la vida

A Giovanna

Per avermi insegnato che bella è la vita

Chapter 1. Introduction

In the face of the ever-growing demand for energy in the 21st century, two major problems have been the focus of attention. The first of these is the depletion of the fossil fuel supply, the main source of energy in the world today. The second is the threat of global warming, greenhouse effects and other environmental problems caused by the indiscriminate use of fossil fuels that recently have been front-page news, as illustrated by the conference on global warming held at the end of 1997 in Kyoto, Japan. For these reasons, alternative sources of energy are of great economic and social, as well as academic, interest.

An alternative to conventional sources of energy that has garnered more public attention in the past few years is the fuel cell.[1-5] A fuel cell is a device that transforms chemical energy directly into electrical energy, thus achieving higher energy efficiencies and significantly lower pollutant emissions than those of other energy-generating sources. It functions by combining an oxidant (typically oxygen from the air) and a fuel (typically H_2 from a variety of sources) electrochemically across an ion-conducting ceramic membrane. Although fuel cells have been known for years, their importance has increased recently due to their potential for transportation applications.[6, 7]

Several types of fuel cells are known, and are typically identified according to the electrolyte of use. One type, known as the Solid Oxide Fuel Cell (SOFC), has been under intense scrutiny during the past few decades as an alternate power source for stationary applications.[8-13] SOFCs offer a number of advantages over other types of fuel cells. In particular, they may be

used with a variety of fuels (e.g. hydrocarbons and alcohols), although hydrocarbons are generally used, and offer especially high-energy conversion efficiencies (*ca.* 50-60%).[14]

A solid oxide fuel cell is composed of two porous ceramic electrodes separated by a solid oxide electrolyte (hence the name). Fuel, typically H_2 or CO, and O_2 combine electrochemically across the solid electrolyte, producing a DC current (under closed circuit conditions). Oxygen is reduced at the cathode, forming oxide ions which travel across the solid electrolyte to the anode, where they oxidize the fuel and produce H_2O or CO_2, liberating electrons which flow through an external circuit to the cathode.

Current SOFC components and designs have encountered some problems. First, they have to be operated at 900-1000 °C to achieve the necessary oxygen fluxes.[15, 16] This results in reactions among the cell components which are detrimental to the cell performance.[17] For example, the cathode and electrolyte materials ($La_{1-x}Sr_xMnO_3$ and yttria-stabilized zirconia, respectively) react at the interface to produce a third phase, $La_2Zr_2O_7$, which is significantly less conductive than the electrolyte material at 1000 °C.[18] Secondly, at such high temperatures, incompatibility of thermal expansion coefficients leads to loss of cell integrity.[19] Because of these concerns, new fuel cell designs[13] and components[20] that can operate at lower temperatures are being sought.

The basic design of a solid oxide fuel cell incorporates a solid electrolyte, an anode, a cathode and an interconnect. The solid electrolyte and the electrode materials require 100% oxide ion conduction and mixed ionic/electronic conduction, respectively. A novel design by Tuller[21] proposes a monostructural template, whereby the electrical properties of a given cell component can be tuned by using an appropriate dopant cation. This would result in a graded monolithic SOFC with clear advantages over conventional designs. The stability of the cell should improve

as the problem of detrimental reactions between adjacent cell components is greatly minimized because they all have the same structure. In addition, thermal expansion mismatch is greatly minimized compared to existing systems, thus providing more durable cells.

The ionic conduction process is believed to occur via a hopping mechanism, whereby an oxide ion moves by jumping from an occupied lattice site to a vacant site.[16] Consequently, materials to be used for these components must contain oxygen vacancies in their structure. To this end, researchers have concentrated on crystal structures where it is possible to introduce oxygen vacancies into the material by doping with aliovalent cations, and thus obtain new materials that exhibit high oxygen ion conductivities. For example, Ishihara *et. al.* were able to synthesize a series of oxygen ion conductors based on doped $LaGaO_3$, a material with the perovskite structure.[22] The highest oxygen ion conductivity was observed for the composition $La_{0.9}Sr_{0.1}Ga_{0.8}Mg_{0.2}O_{3-y}$ (10^{-2} S/cm at 700 °C). Similar examples are provided by doped ZrO_2 and Bi_2O_3, as well as other related fluorite-type materials.[23]

An intergrowth structure made up in part of Bi_2O_3 and perovskite layers can also be appropriately doped to obtain new materials with enhanced ionic conductivity. These layered materials, the so-called Aurivillius phases,[24-26] have been the main subject of research in the zur Loye group. For example, Kendall *et. al.* have synthesized a new series of $n=2$ Aurivillius phases (where n refers to the number of perovskite layers), with general formula $Bi_2Sr_2M_2M'O_{11.5}$ (M=Nb, Ta; M'=Al, Ga), by carrying out substitutions for the B-site cation in the perovskite layers and characterized their electrical properties.[27, 28] An ionic conductivity of 10^{-2} S/cm at 800 °C was reported for the composition $Bi_2Sr_2Nb_2GaO_{11.5}$. Further studies determined that these materials are pure ionic conductors down to 10^{-6} atm. Below this pressure, electronic conduction sets in, presumably due to the reduction of Bi^{3+}.

From the above discussion, it is clear that flexible structures, which can fairly easily be doped, such as the perovskite structure, are good candidates for improved ionic conductors. Similarly, layered systems such as the Aurivillius phases have been shown to exhibit good levels of ionic conductivity. However, it would be of use to come up with other layered materials that are lacking the Bi^{3+} cation in order to avoid possible reduction, as this flaw makes these compounds unsuitable for use as SOFC electrolytes. A combination of all these requirements is satisfied by a family of layered materials, the so-called Ruddlesden-Popper phases.

The Ruddlesden-Popper phases, of general formula $A_{n+1}B_nO_{3n+1}$, were first identified by Ruddlesden and Popper in 1957.[29, 30] Their structure is made up of n ABO_3 perovskite layers sandwiched between an AO rock salt type layer. The first synthesized phase was $Sr_3Ti_2O_7$, but other analogs have recently been reported, namely $Sr_3M_2O_{7-\delta}$, M=Co, Fe, Mn.[31-34] These studies illustrate that a large number of different cations may be introduced into both sites, giving a large array of possibilities to tune the desired properties. We should be able to take advantage of the structural versatility of the perovskite structure[22, 27, 28, 35] to carry out aliovalent cation substitutions in the perovskite layer of the Ruddlesden-Popper phases. Some studies have also reported that some related cobaltates and ferrates are good electronic conductors. This suggested to us a line of research based on the study of solid solutions of general formula $Sr_3Ti_{2-x}M_xO_7$ (M=Al, Ga, Co, Fe or Mn).

The idea behind this approach was to synthesize a family of new doped, oxygen-deficient, layered structures, analogous to the Aurivillius phases previously studied in the zur Loye group. Substitutions with fixed-valent cations in their maximum oxidation state (e.g. Al^{3+}, Ga^{3+}) for Ti^{4+} in $Sr_3Ti_2O_7$ were used in order to synthesize possible electrolyte materials. At the same time, doping with transition metal cations (Co, Fe, Mn) was conceived with a similar idea in mind,

with the added advantage that presumably there would also be a significant electronic conductivity component. Consequently, our interest in these novel material systems stems from their potential as ionic and mixed/ionic electronic conductors. Possible applications obviously include their use as components in the monolithic SOFC design.

This thesis provides an account of our efforts to synthesize and characterize the electrical properties of these new Ruddlesden-Popper phases. The research has attempted to correlate experimental results with standard defect chemical models. Consequently, the electrical properties are discussed in terms of the defect chemistry and oxygen nonstoichiometry in the materials studied herein.

References

1. Lindstrom, O., *Chemtech,* **1988**, 490-497.

2. Krumpelt, M., Kumar, R. and Myles, K. M., *J. Power Sources,* **1994**, *49*, 37-51.

3. Wald, M. L., *Fuel cell will supply power to a test house*, New York Times, New York City, June 17, 1998.

4. Naughton, K., *Detroit's impossible dream?*, Business Week, March 2, 1998, pp. 66-67.

5. Symonds, P. C., Coy, P. and Naughton, K., *How to build a clean machine*, Business Week, May 27, 1996, pp. 90-91.

6. Nonobe, Y. and Kimura, Y., *Toyota Technical Review,* **1998**, *47*, 67-72.

7. Gottschalk, M. A., *Will fuel cells power an automotive revolution?*, Design News, 6/22/98, pp. 86-96.

8. Minh, N. Q., *J. Amer. Ceramic. Soc.,* **1993**, *76*, 563-588.

9. Minh, N. Q., *Chemtech,* **1991**, 120-126.

10. Minh, N. Q. and Takahashi, T., in *Science and Technology of Ceramic Fuel Cells,* Elsevier, New York, 1995, pp. 15-40.

11. Sasaki, H., Otoshi, S., Suzuki, M., Sogi, T., Kajimura, A., Sugiura, N. and Ippommatsu, M., *Solid State Ionics,* **1994**, *72*, 253-256.

12. Tuller, H. L. and Moon, P. K., *Mater. Sci Eng. B- Solid State M.,* **1988**, *1*, 171-191.

13. Riess, I., van der Put, P. J. and Schoonman, J., *Solid State Ionics,* **1995**, *82*, 1-4.

14. Badwal, S. P. S. and Foger, K., *Ceramics International,* **1996**, *22*, 257-265.

15. Dell, R. M. and Hooper, A., in *Solid Electrolytes,* P. Hagenmüller and W. van Gool, Eds. (Academic Press, New York, 1978), pp. 291-312.

16. Riess, I., in *Science and Technology of Fast Ion Conductors,* H. L. Tuller and M. Balkanski, Eds. (Plenum Press, New York, 1987), pp. 23-50.

17. Kawada, T., Sakai, N., Yokokawa, H. and Dokiya, M., *Solid State Ionics,* **1992**, *50*, 189-196.

18. Labrincha, J. A., Frade, J. R. and Marques, F. M. B., *J. Mater. Sci.,* **1993**, *28*, 3809-3915.

19. Kilner, J. A., *Bol. Soc. Esp. Ceram. Vidrio,* **1998**, *37*, 247-255.

20. Hagenmuller, P., in *Superionic Solids and Solid Electrolytes,* A. L. Laskar and S. Chandra, Eds. (Academic Press, New York, 1989), pp. 679-704.

21. Tuller, H. L., Kramer, S. A. and Spears, M. A. , *Solid Electrolyte-Electrode System for an Electrochemical Cell;* U.S. Patent# 5,401,461, 1995.

22. Ishihara, T., Matsuda, H. and Takita, Y., *J. Am. Chem. Soc.,* **1994**, *116*, 3801-3803.

23. Etsell, T. H. and Flengas, S. N., *Chem. Rev.,* **1970**, *70*, 339-376.

24. Aurivillius, B., *Arkiv. Kemi,* **1949**, *1*, 463-480.

25. Aurivillius, B., *Arkiv. Kemi,* **1949**, *1*, 499-512.

26. Aurivillius, B., *Arkiv. Kemi,* **1950**, *2*, 519-527.

27. Kendall, K. R., Thomas, J. K. and zur Loye, H. C., *Chem. Mater.,* **1995**, *7*, 50-57.

28. Kendall, K. R., Navas, C. and zur Loye, H.-C., *$Bi_2Sr_2M'_2M''O_{11.5}$ [(M' = Nb, Ta) and (M'' = Al, Ga)], Synthesis and Characterization of oxygen-deficient Aurivillius Phases*, G.-A. Nazri, J.-M. Tarascon and M. Armand, Eds., (MRS, Materials Research Society Symposium Proceedings: Solid State Ionics IV, Boston, MA, 1995), Vol. 369, pp. 355-360.

29. Ruddlesden, S. N. and Popper, P., *Acta Cryst.,* **1957**, *10*, 538-539.

30. Ruddlesden, S. N. and Popper, P., *Acta Cryst.,* **1958**, *11*, 54-55.

31. Gallagher, P. K., *Inorg. Chem.,* **1965**, *4*, 965.

32. Dann, S. E., Weller, M. T. and Currie, D. B., *J. Solid State Chem.,* **1992**, *97*, 179-185.

33. Dann, S. E. and Weller, M. T., *J. Solid State Chem.,* **1995**, *115*, 499-507.

34. Mizutani, *J. Chem. Soc. (Japan) Ind. Ed.,* **1970**, *73*, 1097-1103.

35. Takahashi, T. and Iwahara, H., *Energy Convers.,* **1971**, 105-111.

Chapter 2. Background

2.1. Applications

This thesis deals almost exclusively with high-temperature oxide ceramics. Such solid-state materials have found a wide range of applications, such as battery components, piezoelectrics, sensors, etc. In particular, we are concerned here with ionic conductors and mixed ionic and electronic conductors. By far, the biggest interest and largest potential market for these materials corresponds to fuel cells. However, other applications are also of importance. In this section, I will provide an overview of these applications.

2.1.1. Fuel cells

Today it is clear that other sources of energy must be found if the world is to sustain the energy needs of its increasing population. Current energy sources (e.g. coal and oil) are not perpetual. Instead, natural gas and hydrogen seem to be preferred as the energy sources for the future. Whether this scenario becomes reality or not will depend primarily on the costs associated with power generation and distribution. In this respect, the fuel cell holds great promise as the power generator of the future.

The concept of fuel cells has been around since the late 19th century, when Sir William Grove first postulated their feasibility. However, despite their simplicity and great promise, fuel cells have not been fully developed and deployed in applications that affect our everyday lives, due to materials and design costs. Only programs like the NASA-sponsored Apollo space

missions of the 1960s, which operated on large budgets, were able to incorporate fuel cells for more efficient on-board energy use.

A fuel cell is a device that converts chemical energy directly into electrical energy. In principle, any reaction with a negative free energy can be used to operate a fuel cell, so that its voltage output would be

$$E = -\Delta G / nF \tag{2.1}$$

where n is the number of transferred electrons, and F is the Faraday constant. In practice, the process involves the electrochemical combination of an oxidant (typically oxygen from the air), and a fuel (typically hydrogen) across an ion-conducting membrane. A cell consists of a cathode, where the oxidant is reduced, e.g.

$$\tfrac{1}{2}O_2 + 2e^- \rightarrow O^{2-} \tag{2.2}$$

and an anode, where the fuel is oxidized, e.g.

$$H_2 \rightarrow 2H^+ + 2e^- \tag{2.3}$$

so that combining both reactions gives

$$H_2 + \tfrac{1}{2}O_2 \rightarrow H_2O \tag{2.4}$$

with the 2 electrons being transferred externally from anode to cathode, closing the circuit. The principle of operation is illustrated in Figure 2.1.

Most fuel cells involve the use of proton-conducting membranes of one type or another. These cells tend to operate at lower temperatures due to kinetic considerations. Other options involve the transfer of the oxide ion, either by combining it with CO_2 (molten carbonate fuel cell) or by using an oxide ion conductor (see Figure 2.1). These types of fuel cells operate at higher temperatures and will be discussed in the section 2.1.1.2.

26

Figure 2.1. Schematic of a fuel cell. In this case, a Solid Oxide Fuel Cell is shown
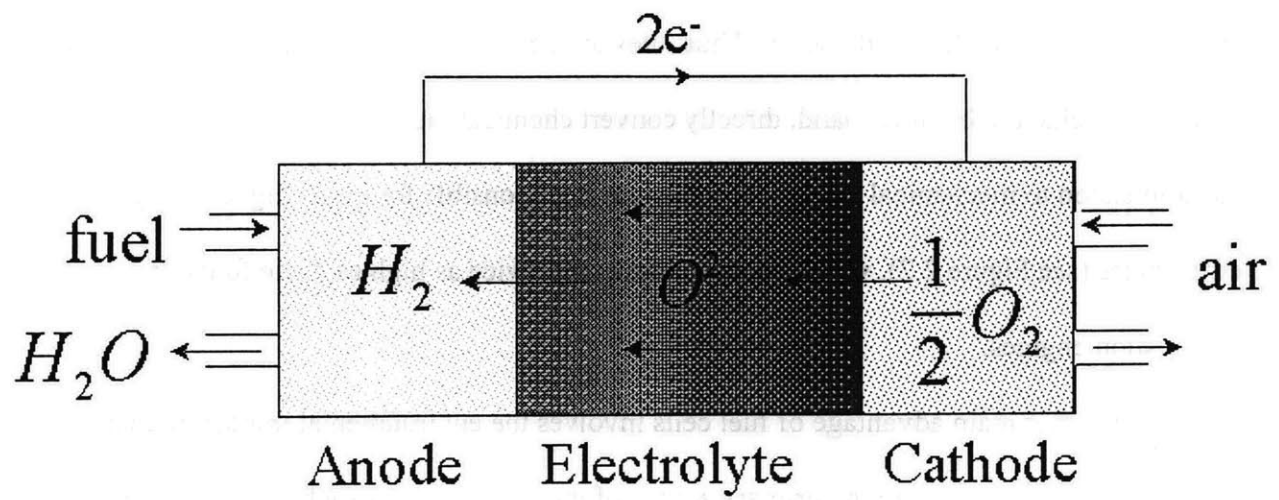
2.1.1.1. Fuel cell advantages

Combustion engines function by transforming chemical energy first into mechanical energy and then into electrical energy. Thus, they are constrained by the thermodynamic Carnot cycle. Fuel cells, on the other hand, directly convert chemical into electrical energy, bypassing the conversion to mechanical energy. This feature is responsible for much higher energy efficiencies (see Figure 2.2), which are, in some cases, twice as high as those found in combustion engines.

The other main advantage of fuel cells involves the environmental impact of energy generation. Power plants are the primary source of greenhouse gases such as CO_2 and NO_x. These gases, among others, have been identified as the primary cause for global warming, a critical issue that was the subject of an international conference at the end of 1997 in Kyoto, Japan. While regulation in individual countries may become somewhat effective in regulating and decreasing the volumes of gases that are released, other technological solutions are gaining attention. Fuel cells are such a solution, because the emissions of most of these pollutants are either significantly lower than those of conventional power plants or even undetectable (see Figure 2.3).

Fuel cells can be used with a variety of fuels, all of which may provide a convenient source of hydrogen. High temperature fuel cells are especially attractive for this reason, since they can tolerate lower purity levels in fuels and can reform hydrocarbons (e.g. natural gas) *in situ*. For fuel cells that operate at lower temperatures, liquid fuels such as ammonia or methanol are also feasible.

Yet another attractive feature of fuel cells is their modularity. Since, in principle, any number of cells can be put together to form so-called 'stacks', which can then be put together into
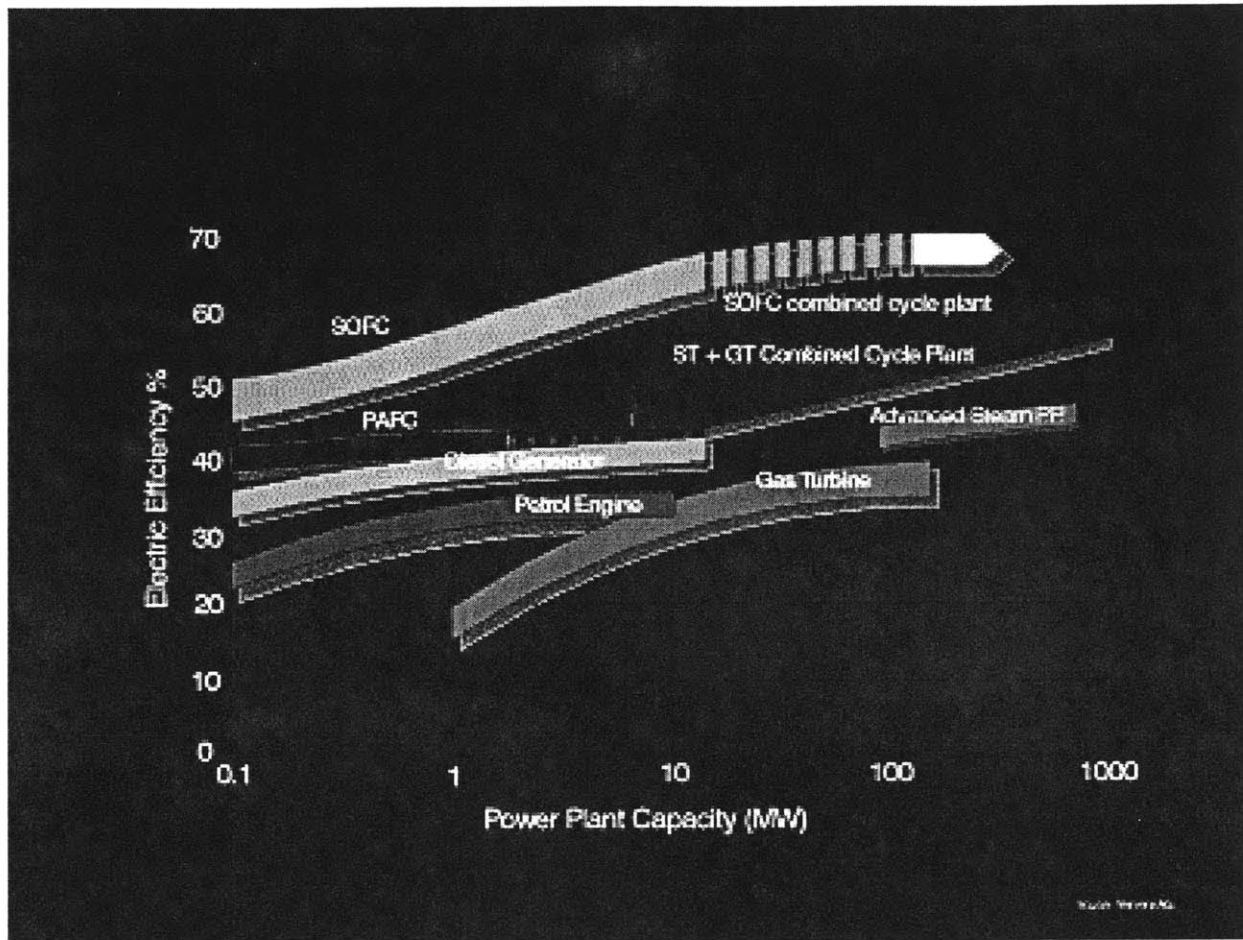
Figure 2.2. Net electric efficiency comparison of Power Generating Systems
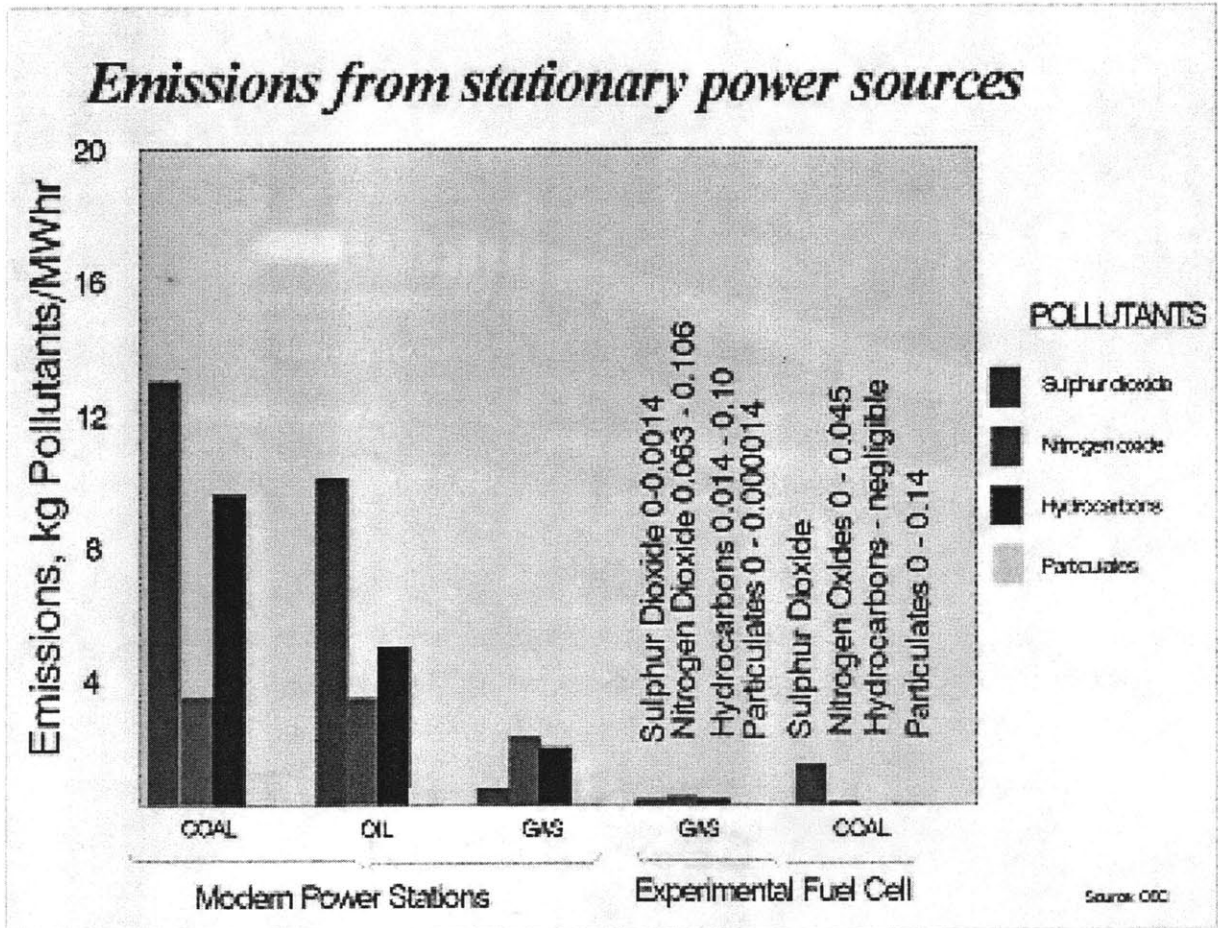
Figure 2.3. Pollutant output from power generating technologies

larger assemblies, power outputs ranging from enough to run a car (*ca.* 100-200 kilowatts)[1] or

small electronic devices to megawatt capacity for power plants can be obtained. Furthermore,

operation of fuel cell assemblies is extremely quiet, a necessity in applications for urban areas.

2.1.1.2. Types of fuel cells

The various types of fuel cells are typically named after the electrolyte used. They can

also be more generally divided according to the temperature of operation. Low-temperature fuel

cells are comprised of the phosphoric acid, alkaline and polymer membrane types, whereas the

molten carbonate and solid oxide operate at high temperatures. Table 2.1 lists the various types

and some of their characteristics.

The Phosphoric Acid Fuel Cell is perhaps the most developed type of fuel cell. IFC

(South Windsor, Connecticut) has developed a commercial unit in connection with Fuji (Japan).

Test units have been purchased by a variety of companies both in the United States and Europe.

However, due to problems with limited lifetimes caused by corrosion of the electrodes, other

types of fuel cells have received increased attention in recent years.

Working prototypes of Alkaline Fuel Cells have also been developed by Elenco and

Siemens, among others, and were used in the Apollo missions of the 1960s.[2] The electrolyte of

choice in this case is aqueous KOH. These fuel cells have encountered some problems. First,

CO_2 from the air can be absorbed and combined with KOH to produce the insoluble K_2CO_3,

which is detrimental to cell performance. In addition, the electrodes are very sensitive to CO

poisoning in the fuel. Because of these considerations, other options such as the polymer

membrane fuel cell are being considered.

Automotive companies have greatly increased their interest in fuel cell technology with the goal of producing an all-fuel cell car by the beginning of the next century.[3] While many problems remain, not only in terms of efficient technology but also of cost, there is little question as to whether there will be fuel cell cars in the future. Such cars would be powered by Proton Exchange Membranes (PEMs) which can operate at low temperatures. Prototypes have already been manufactured by most major car companies, particularly by Daimler-Benz (Germany) in conjunction with Ballard Power Systems (Vancouver, Canada). Some of these prototypes use hydrogen as the fuel, which has to be stored in tanks. To get around this weight problem, researchers are starting to look at methanol as the fuel of choice for PEMs.

The electrolyte in PEMs is a perfluorosulfonic acid polymer capable of conducting protons. These fuel cells operate at low temperatures and have excellent power density (about 2-3 times better than Li batteries), allowing for their incorporation into cars.

The clear advantage of low-temperature fuel cells is the less stringent constraints on component materials imposed by the temperature of operation. At the same time, this temperature of operation also requires suitable catalysts, which in all of the above three cases consist of expensive noble metals such as platinum. The problem of catalyst poisoning is also a common one among all these types of fuel cells.

In contrast, high temperature fuel cells (>600 °C), such as Molten Carbonate Fuel Cells (MCFCs) and Solid Oxide Fuel Cells (SOFCs), are targeted for stationary applications. MCFCs operate at lower temperatures than SOFCs, but also require noble metal catalysts and do not tolerate high levels of impurities such as CO. The MCFC has the added problem that, at its operating temperature, the kinetics of oxygen reduction at the cathode are not fast enough. Both

Table 2.1. Types and characteristics of fuel cells

	Electrolyte	Cathode	Anode	Interconnect	Operating temperature
Polymer Membrane	Perfluorosulfonic acid	PTFE*-bonded Pt on C	PTFE*-bonded Pt on C	Graphite	80 °C
Alkaline	KOH solution	Pt-Au	Pt-Pd	Ni	100 °C
Phosphoric Acid	H_3PO_4	PTFE*-bonded Pt on C	PTFE*-bonded Pt on C	Glassy carbon	200 °C
Molten Carbonate	Molten Li_2CO_3-K_2CO_3	Li-doped NiO	Ni	Stainless steel with Ni	650 °C
Solid Oxide	8% mol Y_2O_3-ZrO_2 (YSZ)	$La_{0.6}Sr_{0.4}MnO_3$	Ni/YSZ	Sr-doped $LaCrO_3$	1000 °C

*PTFE= Polytetrafluoroethylene

types of fuel cells may operate at high enough temperatures that internal natural gas reforming is a significant possibility.

2.1.1.3. Solid Oxide Fuel Cells

SOFCs currently operate at 900-1000 °C. At such high temperatures, the kinetic limitation is reduced to the point where the use of ceramic oxides instead of noble metal catalysts is viable and internal hydrocarbon reforming becomes a very attractive choice.[4] Furthermore, energy efficiencies in SOFCs are higher than in other fuel cell systems and have been projected to be as high as 70% in some cases.[5]

The electrolyte typically used is ZrO_2 doped with 8% mol Y_2O_3 (yttria-stabilized zirconia or YSZ). The presence of that amount of yttria is critical to the success of this material for two reasons. First, it stabilizes the more conductive parent cubic fluorite structure at room temperature; secondly, it introduces oxygen vacancies in the structure, which account for the high ionic conductivity of this material. It should be noted that higher concentrations of oxygen vacancies result in higher activation energies, and hence 8% YSZ is the desired composition. However, this electrolyte requires high operating temperatures to achieve the necessary oxygen fluxes. For this reason researchers have been studying other alternative electrolytic systems. Such materials must have a number of characteristics, which include: a) high ionic conductivity with negligible electronic conductivity (to avoid shorting the cell); b) stability with respect to oxidizing and reducing conditions; c) good chemical stability with respect to the electrode materials with which the electrolyte is in contact; d) good matching of thermal expansion coefficients with the other cell components. As it turns out, these two last requirements are not completely met by YSZ.[6]

Requirements for the cathode material include good ionic and electronic conductivity as well as effectiveness for oxygen reduction, and compatibility (both thermal and chemical) with other cell components, particularly the electrolyte. Since the cathode material is continuously exposed to high oxygen pressures, $p(O_2)$, ceramic oxides constitute the obvious choice. Specifically, perovskite materials of the type $La_{1-x}Sr_xMO_{3-\delta}$ (M= Mn, Fe, Co) are the materials of choice. Although the M= Mn material has the lowest ionic conductivity of the compounds listed above, it shows the best compatibility with the electrolyte in terms of stability and is therefore the compound chosen as the cathode in current SOFCs. However, its relatively low ionic conductivity also has repercussions in cell performance.

The oxygen reduction reaction at the cathode is given by

$$\tfrac{1}{2}O_2(g) + V_o^{\cdot\cdot} + 2e^- \rightarrow O_o^x \tag{2.5}$$

where the Kroger-Vink notation for defects is used. As shown in Figure 2.4, oxygen is reduced at the triple-phase boundary, which refers to the point of contact of the cathode, electrolyte and molecular oxygen gas. A mixed ionic and electronic conductor (MIEC), that is, a material with a significant level of ionic conductivity, would allow a much wider reaction area for oxygen reduction, since the oxide ion may be transported within the MIEC (see Figure 2.4). Thus, polarization losses at the electrode/electrolyte interface are expected to be reduced significantly due to the increase in the charge transfer area.

The anode is exposed to very low $p(O_2)$. Therefore, it must be stable under these conditions and also possess high levels of ionic and electronic conductivity, aside from the usual compatibility requirements with the other components. Furthermore, if internal reforming is

pursued, the anode material should also be catalytically active towards the steam reforming

reaction

$$CH_4 + H_2O \rightarrow CO + 3H_2 \qquad\qquad (2.6)$$

H_2 oxidizes more rapidly than CO or methane, so that more steam is produced. The exothermic

water-gas-shift reaction then takes place to produce more hydrogen

$$CO + H_2O \rightarrow CO_2 + H_2 \qquad\qquad (2.7)$$
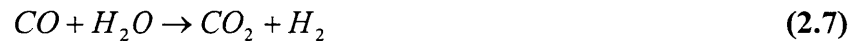
Ni metal is typically used for this purpose. To provide the necessary ionic conduction, a Ni/YSZ

cermet (ceramic metal) is most commonly used as the anode material. However, at the elevated

operating temperatures of a solid oxide fuel cell, Ni particles tend to sinter. This reduces the

specific surface area of the anode and decreases its porosity, thereby hurting cell performance.[8]

An interconnect material, to connect the cathode of one cell to the anode of the next, is

also needed. This component also serves as current collector, has to be stable under very

oxidizing and reducing conditions at the temperature of operation, and cannot be an oxygen ion

conductor. Currently, $La_{1-x}Sr_xCrO_3$, another perovskite, is the material used.

From the above discussion, it is clear that materials constraints are quite high, given the

kind of atmospheric conditions to which cell components are subject. The various known

problems in current state-of-the-art SOFCs are summarized in the schematic shown in Figure 2.5.

The underlying problem still remains the elevated temperature of operation due to the electrolyte.

Consequently, new avenues in research are being pursued to obtain new electrolyte materials that

show appropriate electrical behavior at reduced temperatures (*ca.* 700-800 °C). Some of these

materials are covered in the following section, but here I should point out that the drive towards

lower operating temperature would have a significant impact on the constraints imposed on the

electrolyte and electrode materials. For instance, regarding the cathode material, lowering the

Figure 2.4. Schematics of the SOFC cathode reaction in two cases (taken from Tuller[7]):

a) triple-phase boundary   b) MIEC cathode

$$\text{Overall reaction}:$$

$$\frac{1}{2}O_2(g) + V_o^{\cdot\cdot} + 2e^- \rightarrow O_o^x$$
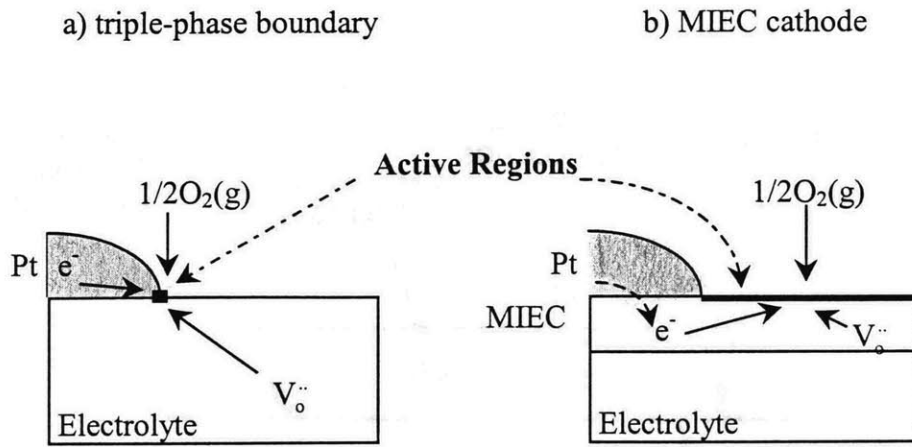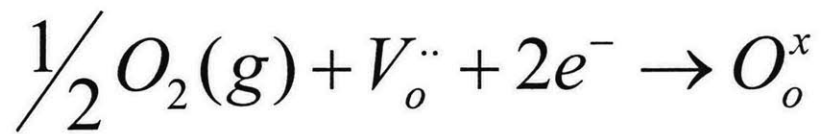
Figure 2.5. Problems arising in current Solid Oxide Fuel Cells

Decreases of length of the triple phase boundaries due to sintering

Formation of insulating compounds

Decreases of porosity

Diffusion of cathode elements into electrodes

Cathode

Electrolyte

Anode

Cracking & Flaking

Sintering of nickel particles
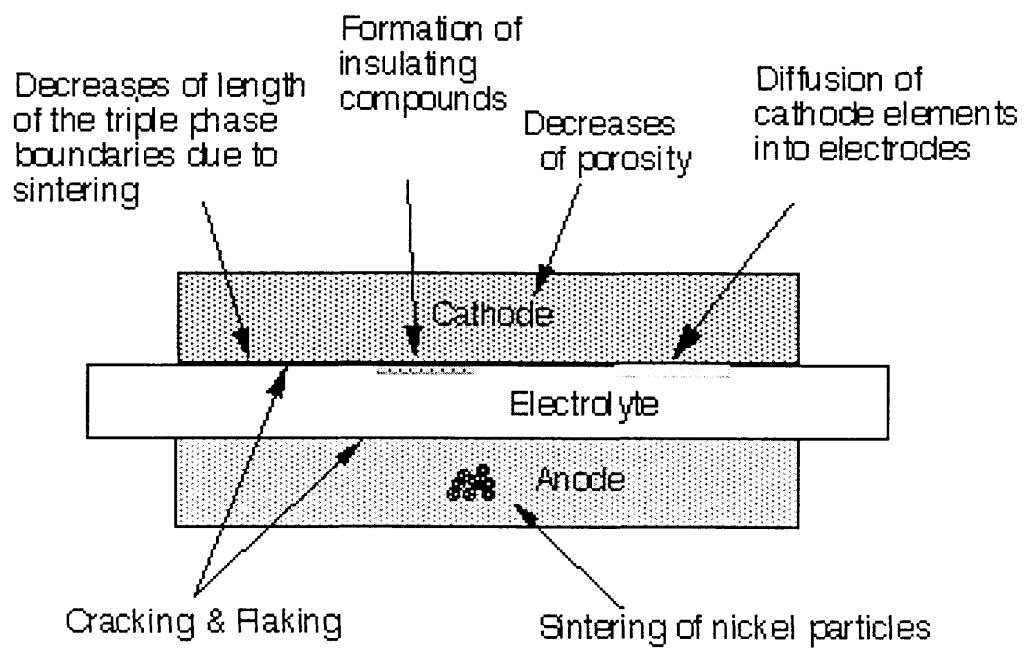
operating temperature to about 700 °C prohibits the use of lanthanum manganite, and other types of perovskites may thus be needed (e.g. $La_{1-x}Sr_xFe_{1-y}Co_yO_{3-\delta}$). Lower operating temperatures would have a positive effect on all other materials that make up the balance of plant.[9] For example, cheaper metallic current collectors might be feasible as interconnect components.

2.1.2. Oxygen sensors

Gas sensors based on Solid Oxide Electrolytes (SOEs) can be used to monitor the concentration of a number of gases of interest in industrial applications, including oxygen and carbon monoxide. In particular, YSZ is today widely used as the mandatory oxygen sensor in automobiles.

An oxygen sensor detects the voltage differential that develops when an SOE is exposed to two different partial pressures of oxygen (see Figure 2.6). The effect is due to the difference in chemical potential of oxygen on both sides. The Nernst equation predicts what the voltage drop across the electrolyte should be:

$$E = \frac{RT}{4F} \ln\left[\frac{P_{O_2}^{'}}{P_{O_2}^{''}} \right] \tag{2.8}$$

where $P_{O_2}^{'}$ and $P_{O_2}^{''}$ refer to the oxygen partial pressures on both sides of the electrolytic membrane. Typically, one of these is air, which is kept constant as a reference. By measuring the voltage, one can easily compute the partial pressure of oxygen on the other side.

Similarly, the same principle that governs oxygen sensors can be applied to transport or "pump" oxygen across an SOE membrane. As stated above, the Nernst equation governs the voltage developed across an ionic-conducting membrane exposed to different partial pressures of oxygen. If a voltage is applied across the membrane, oxygen will be pumped across accordingly.

Figure 2.6. Schematic of an oxygen sensor

$$P'_{O_2}$$

Electrolyte ─ [O^{2-}]

$$P''_{O_2}$$
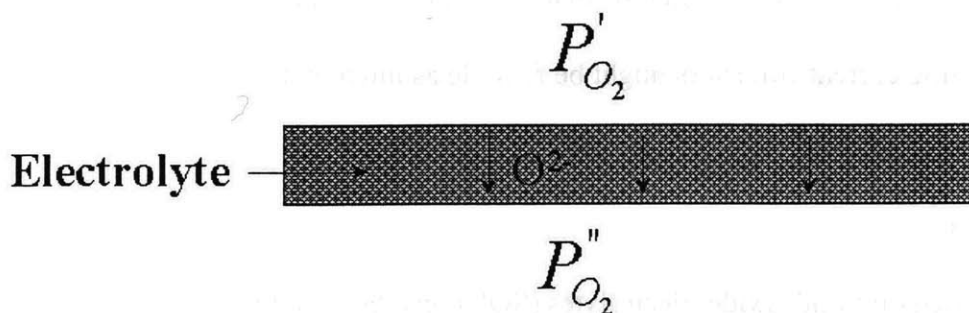
$$E = \frac{RT}{4F} \ln\left(\frac{P'_{O_2}}{P''_{O_2}}\right) \quad \text{where}$$

P'_{O_2} = reference partial pressure, typically air

P''_{O_2} = pressure of O_2 to be measured

We should point out that these techniques can be further used in partial oxidation catalysis reactions, particularly the partial oxidation of light hydrocarbons such as natural gas. It is currently very desirable to control the supply of oxygen to the reactants in order to ensure only partial oxidation while avoiding total oxidation. These and other applications, as well as possible materials, have previously been reviewed in the literature.[10]

2.2. Existing oxide ion and mixed ionic and electronic conductors

This section will give an overview of the relevant research carried out on oxide ion and mixed conductors. It is by no means an exhaustive review. Such reviews are already available in the literature.[11-14] I will concentrate mainly on fluorite-related and perovskite-related systems, since these have a direct impact on the research presented in this thesis.

2.2.1. Fluorite oxides

Until a few years ago, most of the research on oxide ion conductors had concentrated on fluorite-structured oxides of general formula MO_2.[13, 15] The fluorite structure, named after the mineral with the formula CaF_2, is made up of a cubic close-packed array of cations with anions occupying all the tetrahedral holes, so that the fluoride ions are in 4-fold coordination, and the cations are in 8-fold coordination. One can also think of the structure as the cations sitting in the center of a cube, with fluoride ions occupying the corners. A number of tetravalent cation oxides form this structure, notably ZrO_2 at high temperatures and CeO_2.

In the case of ZrO_2, the cubic fluorite phase exists only at high temperatures (>2300 °C), while at lower temperatures it has a monoclinic (below 1000 °C) or tetragonal structure (1000-

2300 °C). However, the cubic structure can be stabilized at lower temperatures by the addition of

dopants, which must have a cationic radius similar to that of Zr^{4+} and a lower valence. Perhaps

the two most important such dopants from a technological point of view are Ca^{2+} and Y^{3+}. It is

thus possible to stabilize the cubic structure and also create oxygen vacancies, which are

necessary to maintain charge neutrality. One might expect that higher ionic conductivity would

result from increased dopant content. However, this is not the case. For example, in the case of

Y^{3+}, the maximum conductivity is observed at compositions around ZrO_2-8%Y_2O_3; when higher

concentrations of Y_2O_3 are added, there is a decrease in ionic conductivity and an increase in

activation energy. This effect is due to what is known as "vacancy clustering," whereby vacancies

associate in clusters, producing a decrease in the effective number of mobile oxygen vacancies.[13]

Magnitudes of ionic conductivities in stabilized zirconias are on the order of 0.1 S/cm at

1000 °C, and ionic transference numbers are close to unity. These characteristics are responsible

for YSZ being the electrolyte of choice in high-temperature applications. It should be pointed out

that other rare-earth metals also stabilize the cubic fluorite structure of zirconia. These include

La^{3+}, Gd^{3+} and Sm^{3+}, among others.[13]

CeO_2 also has the fluorite structure. Interest in this material stems from the fact that it

exhibits deviations from stoichiometry, and so has intrinsic oxygen vacancies.[16] Furthermore, the

ability of Ce^{4+} to reduce to Ce^{3+} may introduce electronic conductivity at low partial pressures of

oxygen. It is therefore critical to determine the relative magnitudes of ionic and electronic

conductivities, in order to establish the feasibility for applications purposes. If one looks at how

anionic vacancies effect this property,

$$\frac{1}{2}O_2(g) + V_o^{\cdot\cdot} + 2e^- \leftrightarrow O_o^x \tag{2.9}$$

we determine that a higher concentration of vacancies will shift the equilibrium to the right.

Thus, introduction of aliovalent dopants suppresses the appearance of electronic conductivity, while still allowing for high levels of ionic conductivity. As an example, $(CeO_2)_{0.8}(Gd_2O_3)_{0.2}$ has an ionic conductivity of about 0.1 S/cm at 800 °C.[17] This material is being seriously considered as a possible replacement for YSZ as the electrolyte of choice in intermediate temperature SOFCs.[18]

Another fluorite system of interest is that of δ-Bi_2O_3. As can be seen from its formula, it does not correspond to an MO_2-type oxide. In fact, at low temperature it has a monoclinic structure; however, when heated to about 750 °C, it undergoes a phase transition to a defect fluorite-type structure, where ¼ of the oxygen sites are vacant. As expected, the transition is accompanied by a jump in its oxide ion conductivity from 10^{-3} S/cm to very high values (>1 S/cm).[19] Another reason for its high ionic mobility is believed to be the polarizability of the Bi^{3+} cation. Consequently, many efforts have been devoted to stabilize its cubic structure at low temperatures by the addition of several dopants. Many such studies have been carried out,[20-22] and I will not provide a description of all of them here. Suffice it to say that, indeed, a variety of dopants of appropriate ionic radius (e.g. Sr^{2+}, Ca^{2+}, Y^{3+}, Ln^{3+}) can stabilize the fluorite structure of Bi_2O_3 at low temperatures. Such doped materials display transference numbers higher than 0.9 as well as high conductivities (0.1 S/cm at 700-800 °C). However, the magnitude of the ionic conductivity is, in all cases, lower than in the parent phase. This has been attributed to an association between oxide ion vacancies and doped cations.[23] A problem common to these Bi-based systems is that they readily reduce at lower pressures of oxygen, thereby introducing electronic conductivity. Therefore, despite their high ionic conductivity, this feature makes them unsuitable for use as electrolytes in SOFCs.

Another related system is that of the pyrochlore materials. Their structure is that of an oxygen-deficient fluorite, with vacancies ordered in a certain crystallographic site. The general formula is $M_2^{3+}M'_2^{4+}O_7$ (for reference, $M_2^{4+}O_8$ represents the parent fluorite), where M is a large cation such as Gd^{3+}, Y^{3+}, La^{3+}, and M' is a smaller cation such as Zr^{4+}, Ti^{4+} or another first-row transition metal. From the formula, it is clear that 1/8 of the oxygen sites are vacant. It is this feature that makes them of interest in regards to oxygen ion conductivity. In particular, Tuller and coworkers have examined a number of compositions of the type $Gd_{2-x}Ca_xM_{2-y}M'_yO_7$, M= Ti, Zr; M'= Mo, Mn, and determined that, for example, substituting Ti with Zr increases the structural disorder in the oxygen sublattice which results in an increase in the ionic conductivity.[24-28] Introduction of a number of dopants into the structure can, by controlling the concentration of the various charged defects, provide a handle on the electrical properties of the resulting materials, so that both pure ionic and mixed ionic and electronic conductors can be obtained. Ultimately, the goal is to produce an all-pyrochlore fuel cell such that all cell components belong to this same structure type. By introducing an appropriate dopant cation, the electrical properties would be tuned from predominantly electronic with good levels of ionic conduction (electrodes) to purely ionic (electrolyte), utilizing a pyrochlore template.

2.2.2. Perovskite-type oxides

Aside from the fluorite ionic conductors, possibly the most important group of materials of interest in the last few years has been that with the perovskite-type structure.

This structure, of general formula ABO_3 and named after the mineral $CaTiO_3$, is represented in Figure 2.7. It may be described as consisting of corner-sharing BO_6 octahedra with the A cation sitting in the space left between eight such octahedra. A number of large,

12-coordinate cations such as Na^+, K^+, Ca^{2+}, Sr^{2+}, Pb^{2+}, La^{3+}, Bi^{3+}, etc., may fit in the A site, whereas smaller cations well suited to octahedral coordination such as Fe^{3+}, Cr^{3+}, Ti^{4+}, Zr^{4+} Nb^{5+}, Ta^{5+}, Mo^{6+}, W^{6+}, etc., may occupy the B site. The geometrical limits for the cationic radii are quantified by the so-called Goldschmidt Tolerance Factor, given by

$$t = (r_A + r_O)/\sqrt{2}(r_B + r_O) \tag{2.10}$$

where r_A, r_B and r_O represent the ionic radii of the A, B and O^{2-} ions. Normally, the perovskite structure is stable for $1.0 > t > 0.75$. In principle, any combination of cations of appropriate size, whose valences add up to +6, can form the perovskite structure. In fact, even ReO_6 exists without an A cation. One of the main advantages of this structure is the wide variety of cations that may fit in the A and B sites, thus conferring it great flexibility. In view of this fact, it is not surprising that the electrical properties of perovskite materials can range from metallic conductors (e.g. $LaNiO_3$)[29] to ionic conductors (doped-$LaAlO_3$).[30] This feature may be used to advantage by introducing dopant cations into a parent phase composition to achieve various properties.

Of further interest for our purposes is the fact that this structure can also accommodate oxygen vacancies with relative ease.[12] In some cases, when the oxide ions are removed from a specific site, these oxygen vacancies order throughout the lattice, and a new structure may form. Otherwise, a simple oxygen-deficient perovskite is formed, of which many different types are known. A large number of these materials resulted from the flood of research on high-T_c cuprate superconductors. These have been previously reviewed in a systematic manner.[31]

Takahashi (1971) was the first to investigate the feasibility of doping a stoichiometric perovskite to make it oxygen-deficient and study its oxygen ion conductivity.[30] He chose the $La_{1-x}M_xAlO_3$ (M=Ca, Ba) system, among others, and observed an increase of over two orders of magnitude in the conductivity of the doped samples compared to the undoped parent phases.
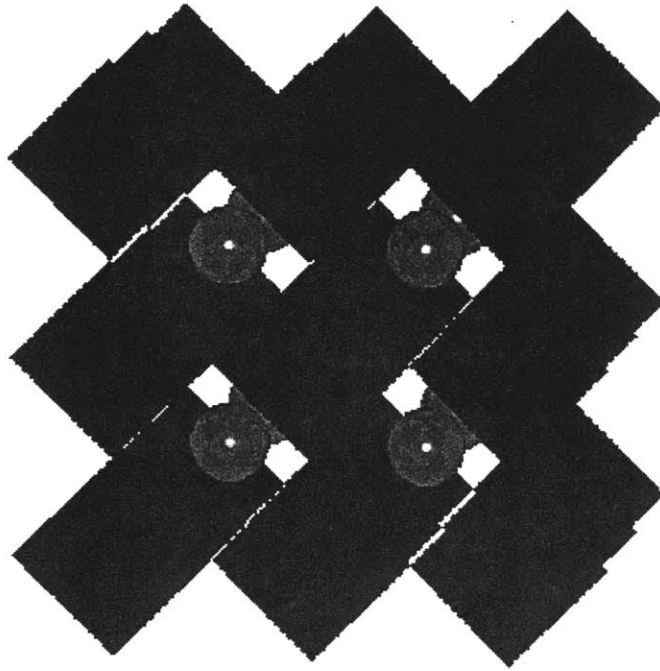
Figure 2.7. Perovskite structure. BO_6 octahedra are in dark, while the A cations are in light gray

This approach has now been extended into new systems. Both $NdAlO_3$ and $LaGaO_3$ have been doped and examined for their oxide ion conductivity.[32-34] Initial work with doped $NdAlO_3$ showed the highest oxide ion conductivity for the composition $Nd_{0.9}Ca_{0.1}Al_{0.5}Ga_{0.5}O_{3-\delta}$ (4.0×10^{-2} S/cm at 950 °C). Doping with Ga both increased the ionic conductivity and extended the electrolytic regime to higher partial pressures of oxygen. In the case of $LaGaO_3$, the highest oxide ion conductivity was found for the composition $La_{0.9}Sr_{0.1}Ga_{0.8}Mg_{0.2}O_{3-\delta}$, (0.3 S/cm at 950 °C) which also showed $p(O_2)$-independent conductivity from 1 to 10^{-20} atm. The width of the electrolytic regime makes this material attractive as a solid electrolyte for SOFCs.[35]

The oxygen vacancies can be ordered or disordered in these perovskite-related phases, and the degree to which they do so has a direct impact on their ionic conductivity. For example, the conductivity of the brownmillerite phase $Ba_2In_2O_5$ was studied by Goodenough et al.[36] This material shows a jump in conductivity of more than an order of magnitude near 900 °C. Such a jump was later found to be associated with an order-disorder transition in the oxygen vacancies that starts at that temperature and ends at 1200 °C, at which point the structure becomes a cubic perovskite.[37] Figure 2.8 summarizes the above ionic conductivity data; it shows representative compounds from the above discussion of various structural groups.

As was mentioned before, perovskites allow a wide range of cations in their structure, thus enabling the tuning of desired electrical properties. Previously, we have covered perovskite ionic conductors. A large number of transition metal perovskites of the type $MM'O_{3-\delta}$, (M=La, Sr; M'= first row transition metal), most of which are electronic conductors, are also of importance. Many of these compounds find applications in catalysis,[38-41] and sensors[42] but perhaps their most important application and the subject of many studies is as cathodes in

47
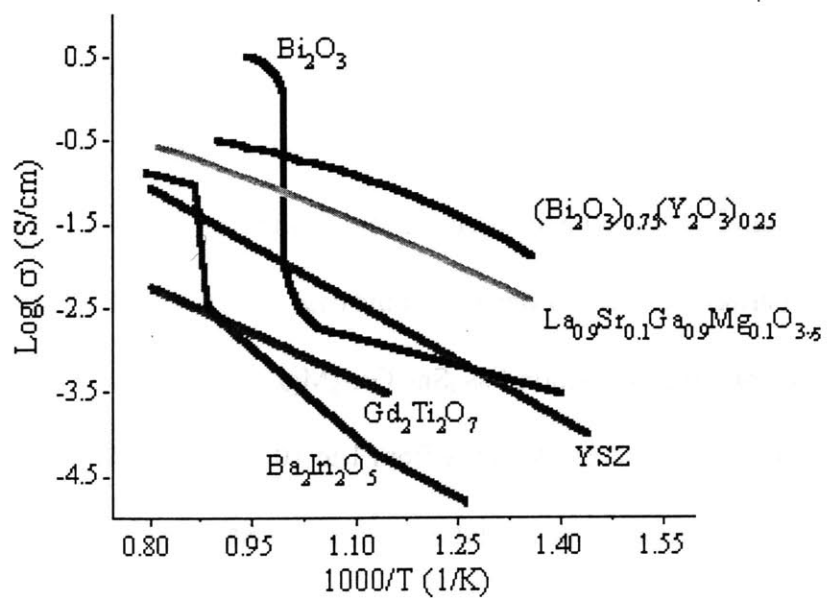
Figure 2.8. Ionic conductivity of YSZ, Bi$_2$O$_3$, (Bi$_2$O$_3$)$_{0.75}$(Y$_2$O$_3$)$_{0.25}$, Gd$_2$Ti$_2$O$_7$, Ba$_2$In$_2$O$_5$ and La$_{0.9}$Sr$_{0.1}$Ga$_{0.8}$Mg$_{0.2}$O$_{3-\delta}$.

SOFCs.[43, 44] In this respect, the family of materials that is of special interest here has the general

formula $La_{1-x}Sr_xMO_3$, M=Co, Fe, Mn.[9, 45, 46]

The properties of $La_{1-x}Sr_xMO_{3-\delta}$ (M=Co, Fe, Mn) as mixed ionic and electronic

conductors are greatly influenced by nonstoichiometry. Increasing the value of x must be

accompanied by charge compensation through one of two mechanisms: an increase in the oxygen

vacancy content or oxidation of the transition metal. Usually a combination of these two factors

is achieved. The interactions of these materials with the surrounding atmosphere define their

defect chemistry and electrical properties.

In the case of Mn, the material is stoichiometric in air, and remains that way until

$p(O_2)=10^{-10}$ atm. This implies that there is charge compensation through partial oxidation of Mn,

so that there is an equilibrium of Mn^{3+} and Mn^{4+} present in the material. The lack of oxygen

vacancies has an effect on the surface exchange of oxygen, which is predictably low. Bulk ionic

conductivities are generally small and show little dependence on the concentration of Sr.[9]

Although the ionic conductivity in this material is not very high, the manganite is the cathode of

choice due to its relative stability with respect to the YSZ electrolyte when compared to the

cobaltite and ferrite perovskites.

The acceptor doped cobaltites, $La_{1-x}Sr_xCoO_{3-\delta}$, do show improved electrical properties

with respect to the manganites. First, the diffusivity of oxygen is approximately 5 times higher.

Secondly, an increase in Sr concentration is accompanied by an increase in the ionic

conductivity. Perhaps as important is the fact that with increased Sr concentration there is charge

compensation through partial oxidation of the Co cation, so that average oxidation states range

between 3.0 and 3.4, and through creation of oxygen vacancies.[47] Despite the improved electrical

properties shown by the cobaltites, there is also a larger mismatch between its temperature

expansion coefficient and that of YSZ than displayed by the manganite analog. Furthermore, the cobaltite perovskites react more readily with YSZ to form an insulating second phase at temperatures of around 1000 °C.

The ferrites show electrical properties comparable to those of the cobaltite, although slightly lower in magnitude. The dependence of the electrical properties on nonstoichiometry has been studied by Misuzaki and coworkers.[48]

All the above acceptor-doped perovskites show p-type electronic conductivity at high $p(O_2)$'s. The magnitude of the conductivity is directly related to the degree of electron localization in the transition metal. In these cases, the trend observed is Co<Fe<Mn in the order of increasing localization of electrons.

Due to the flexibility of the structure, more than one transition metal may be accommodated in the B-site. Teraoka and coworkers have investigated the oxygen permeability of the family of perovskites with general formula $La_{1-x}Sr_xFe_{1-y}Co_yO_{3-\delta}$.[49-51] It was observed that increasing the Sr and Co contents also increased the oxygen permeability, the highest value being that of $SrFe_{0.2}Co_{0.8}O_{3-\delta}$. Mixed-conducting perovskite-related compounds have been widely studied and literature reviews are available.[10, 43, 45]

A recently discovered new material deserves special mention. Ma *et al.* reported very high oxygen ion fluxes in a perovskite-related material, of nominal composition $SrFeCo_{0.5}O_x$.[52, 53] At 800 °C in air, total and ionic conductivities are 17 and 7 S/cm, respectively. Manthiram and coworkers later reported the structure of this compound, which is made up of an intergrowth of a perovskite block and a $(Fe, Co)_2O_{2.5}$-type layer structure.[54] The unusually high oxygen ion conductivity was explained in terms of conduction in the $(Fe, Co)_2O_{2.5}$ layer via an

50

interstitial mechanism. Thus, the conduction would be strictly 2-dimensional. This material is currently being targeted for use in the direct conversion of methane to syngas ($CO + H_2$).

2.2.3. Aurivillius phases

The so-called Aurivillius phases constitute another important group of materials. They were first reported by Bengt Aurivillius in 1949.[55-57] Their general formula is $Bi_2A_{n-1}B_nO_{3n+3}$ and their structure can be described as an intergrowth of $\{Bi_2O_2\}^{2+}$ and perovskite $\{A_{n-1}B_nO_{3n+1}\}^{2-}$ slabs (n=1-5). The A and B cations have similar size constraints as those found in pure perovskites. The structure of an n=2 member, $Bi_2SrTa_2O_9$, is shown in Figure 2.9. Aurivillius phases have well documented ferroelectric properties,[58] and they also show interesting catalytic properties.[59, 60] Their oxygen ion conductivity was first reported by Takahashi and coworkers,[20, 61] who reported values as high as 0.1 S/cm at 950 °C in single crystals of Bi_2WO_6 (n=1). More recently, a flurry of research has concentrated on the BIMEVOX family of materials, $Bi_2V_{1-x}M_xO_{5.5-\delta}$, (M=Cu, Ti, Ni, Zn, Co, Nb, etc).[62-73] This research started in 1986 when Bush[74] reported the synthesis and structure of $Bi_2VO_{5.5}$, the parent phase (n=1). These materials have intrinsic oxygen vacancies in the perovskitic region, and display excellent levels of oxide ion conductivity (10^{-3} S/cm at 250 °C for $Bi_2V_{0.9}Cu_{0.1}O_{5.35}$), and low activation energies (0.5 eV for the same material). As was the case with Bi_2O_3, addition of dopants stabilizes a more conductive and disordered high-temperature structure to lower temperatures. Furthermore, the materials also show a tendency to reduce at $p(O_2)<10^{-6}$ atm, which makes them unsuitable for SOFC applications.
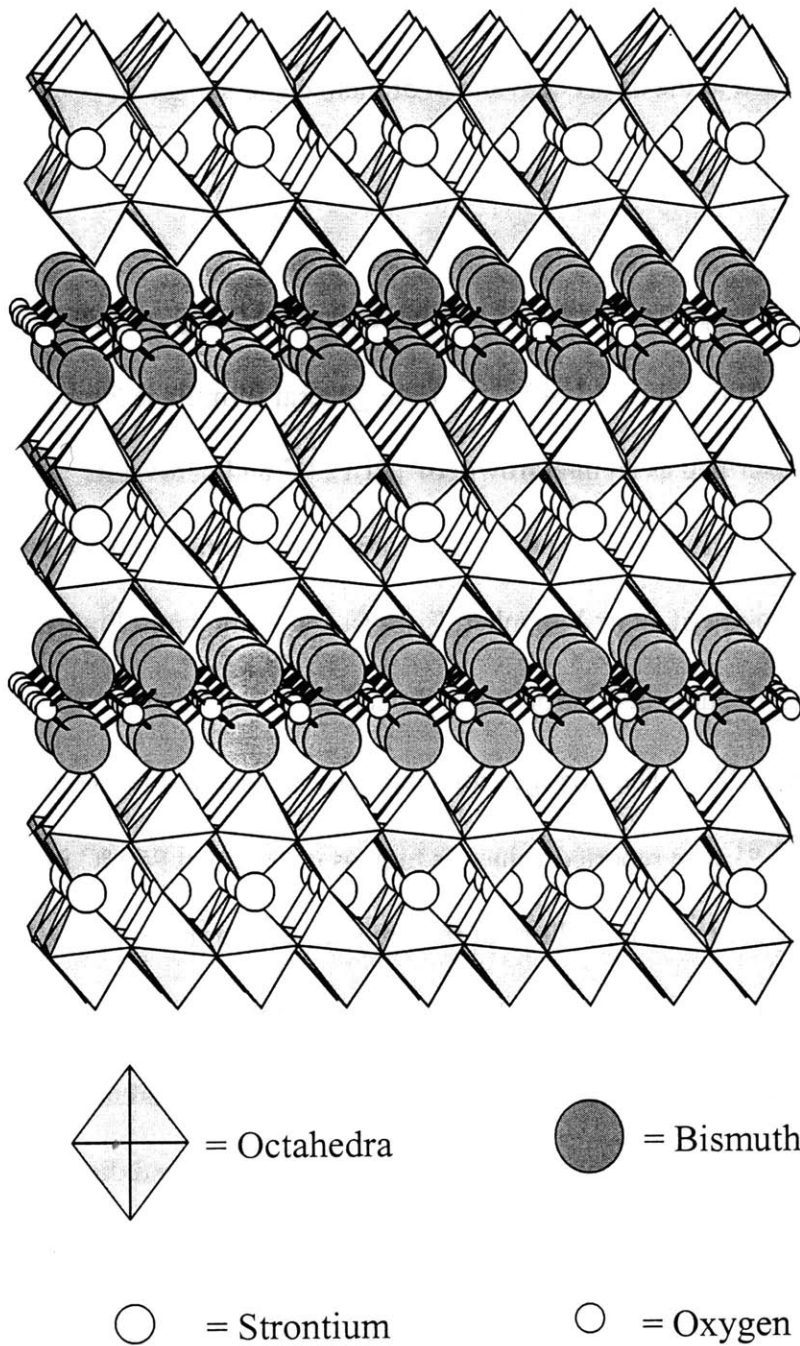
Figure 2.9. Structure of Bi$_2$SrTa$_2$O$_9$. Two octahedral "perovskite layers" separated by puckered bismuth oxide sheets. The octahedra consist of tantalum coordinated by six oxygens

Studies of modified Aurivillius phases with n= 2-4 have been carried out. For example, Jacobson and coworkers performed A and B cation substitution on a n=2 phase, $Bi_2CaNb_2O_9$, and determined that significant improvement in oxide ion conductivity could be obtained for B-site doping.[75] Specifically, $Bi_2CaNb_{2-x}Ti_xO_{9-y/2}$ displays a conductivity of 5×10^{-4} S/cm at 900 °C, about 2 orders of magnitude higher than in the parent phase, and an activation energy of 1.0 eV. Their studies also found that doping in the A-site did show some improvement, although not as much as that seen with B-site doping.

More exhaustive studies have been carried out in the zur Loye group in recent years.[76-79] Julie Thomas studied the effects of doping on some n=4 Aurivillius phases of general formula $Bi_4BaTi_3MO_{14.5}$ (M=Sc, In and Ga). She observed conductivity values at 900 °C on the order of 1×10^{-2} S/cm. Kurt Kendall examined the ionic conductivity of a family of doped n=3 materials, $Bi_2Sr_2M'_2M''O_{11.5}$ (M'=Nb, Ta; M''=Al, Ga), and observed pure ionic conductivity down to about 10^{-5} atm of oxygen with a value of about 1×10^{-2} S/cm at 800 °C.

Two features are of interest in these doped materials. First, all of them display an order-disorder transition similar to what was observed for $Ba_2In_2O_5$ at high temperatures (700-800 °C).[36] This behavior suggests that at lower temperatures, oxygen vacancies are ordered, and at higher temperatures these vacancies become partially disordered, resulting in an increase in ionic conductivity and a decrease in activation energy.

Secondly, and perhaps more importantly from an applications point of view, doped Aurivillius phases, similar to what was seen in Bi_2O_3-based systems, generally show reduction at $p(O_2)<10^{-5}$ atm. The reducibility of Bi^{3+} poses a problem in terms of the use of these materials as electrolyte materials in SOFCs.

2.3. Ruddlesden-Popper Phases

In this section, I cover background material on the Ruddlesden-Popper phases, followed by the motivation behind our studies based on a family of compounds belonging to these types of materials.

2.3.1. Background

The so-called Ruddlesden-Popper phases were first reported by Ruddlesden and Popper in 1957.[80, 81] They synthesized $Sr_3Ti_2O_7$ and recognized that its structure was tetragonal, made up of intergrowths of perovskite layers (2 in this particular case) and a rock salt-type layer. The structure is shown in Figure 2.10. Later, it was established that the general structural motif belongs to a wider class of compounds. It corresponds to a general structure where n perovskite layers (n ABO_3) are sandwiched between a rock salt-type layer (AO) to give a family of materials with the general formula $A_{n+1}B_nO_{3n+1}$, with the n=∞ member corresponding to the pure perovskite structure.

The technological importance of these materials had been very limited until 1986, when the search for the cuprate superconductors grew rapidly following the discovery of superconductivity in $La_{2-x}Ba_xCuO_4$.[82, 83] Other 2-layer Ruddlesden-Popper phases have also been studied in connection with superconductivity. For example, the structure of $La_2CaCu_2O_6$ can be derived from that of $Sr_3Ti_2O_7$ by replacing titanium with copper, strontium with lanthanum and calcium and removing oxygens between the planes of copper atoms.[84] This compound superconducts at 60 K. [85] Demonstrating the structural flexibility of these materials, Poeppelmeier and coworkers
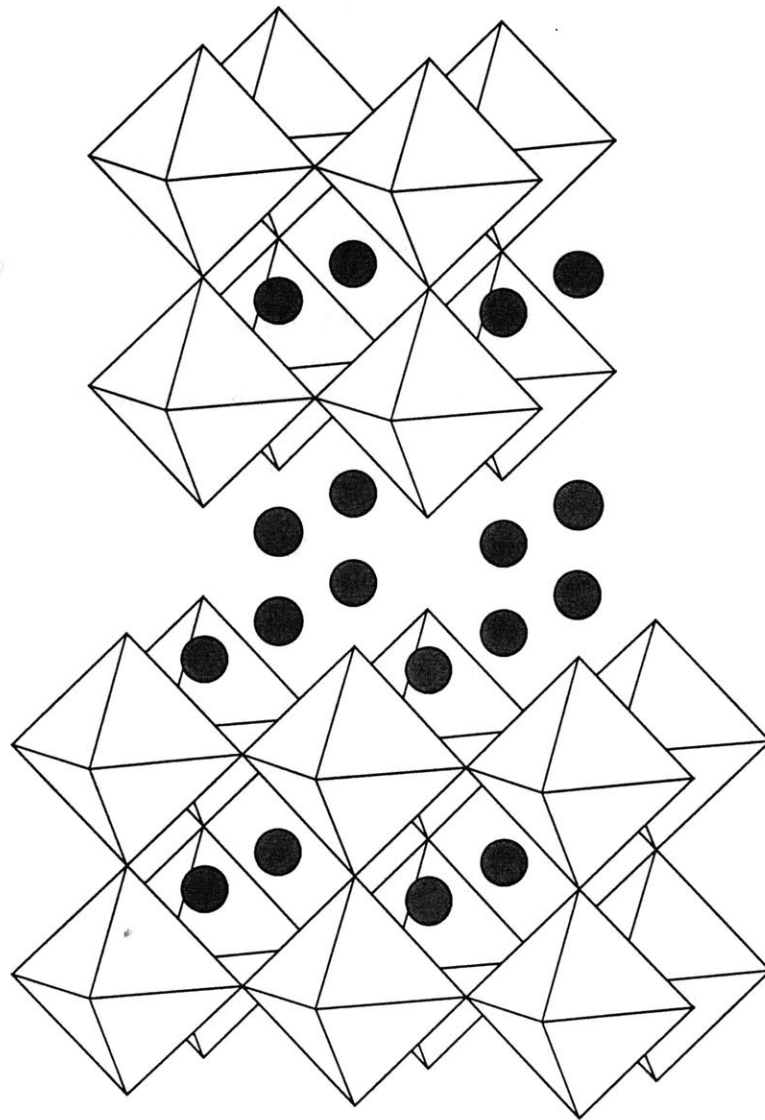
Figure 2.10. Structure of Sr$_3$Ti$_2$O$_7$. Dark circles represent Sr atoms, while TiO$_6$ octahedra are in light color

recently reported a new compound of general formula $LaSr_2CuTiO_{6.5}$, a combination of both previous examples.[86]

Other examples of technological importance include the discovery of giant magnetoresistance effects in another n=2 material, $La_{1+x}Sr_{2-x}Mn_2O_7$.[87, 88] These effects can be applied, for example, in reading heads for hard disk drives.

Only a few studies of the electrical properties of Ruddlesden-Popper phases exist. Turrillas *et al.* studied the conductivity of $Sr_3Ti_{1.9}M_{0.1}O_{7-\delta}$, (M=Al, Mg) in air.[89] They observed low levels of conductivity (10^{-5} S/cm at 500 °C for M=Al) and activation energies around 1 eV. Interested in possible reaction products at the interface of YSZ and $La_{1-x}Sr_xMnO_3$ in SOFCs, Poulsen and van der Puil studied the conductivity of the family of materials $Sr_{n+1}Zr_nO_{3n+1}$, n= ∞, 1, 2, 3, measuring values around 10^{-4} S/cm at 1000 °C in air, and activation energies of around 0.5-0.6 eV.[90]

2.3.2. Research motivation

The first section in this chapter described past efforts by different groups to come up with new ionic and mixed ionic and electronic conductors. Of particular interest in our research group (Prof. zur Loye's group) was the study of ionic conductivity in doped Aurivillius phases (n=3-4) carried out by Dr. Kurt R. Kendall and Dr. Julie K. Thomas.[76-78] At the heart of the project was the idea that intergrowth structures may be used and their components tailored to favorably effect the desired electrical properties.

Even though the approach did provide a new system with good levels of ionic conductivity, several problems became evident. The first, of a more practical nature, refers to the lack of success in synthesizing new compositions.[91] In fact, only 4 ionic conductors were

synthesized and characterized. This was due, to a large extent, to the number of different cationic reactants (oxides and carbonates) that were mixed together and reacted together, usually leading to the presence of secondary phases. The second, and perhaps more critical problem, refers to the ultimate usefulness of these compounds for industrial applications, specifically SOFCs. The main problem encountered in Bi-based systems (both Aurivillius phases and Bi_2O_3-based solid solutions) is the reducibility of the Bi^{3+} cation. At the same time, it was believed that the polarizability of this cation is a major reason for the high ionic conductivities observed in these types of materials.

On the other hand, pure perovskites are known to be good ionic conductors when appropriately doped, as indicated earlier. With the precedent of these two systems in mind, it appeared possible to follow a similar approach to that used in the Aurivillius phases, and obtain good layered perovskite-based ionic conductors lacking the $\{Bi_2O_2\}^{2+}$ layer. For this purpose, a layered perovskite material such as the Ruddlesden-Popper phase $Sr_3Ti_2O_7$ seemed a prime candidate. It is possible to dope this parent phase with lower-valent cations of the appropriate size into the B-site of the perovskite region.

Other analogs of $Sr_3Ti_2O_7$ are also known. For example, the iron analog of the titanate was originally synthesized by Gallagher and coworkers via decomposition of the corresponding oxalates.[92-94] They determined the reaction steps by thermogravimetric techniques and Mossbauer spectroscopy, which unequivocally confirmed the presence of Fe(IV). Later, Dann and Weller reported the synthesis of $Sr_3M_2O_{7-x}$ (M=Fe, Co), and identified these materials as two members of the Ruddlesden-Popper family.[95, 96] The oxidation state of the transition metal and the oxygen nonstoichiometry was shown to be dependent on the synthesis conditions. Regarding the Fe-containing phase, they observed that, as the oxygen stoichiometry decreased from 7 to 6,

the oxygen was removed selectively from the site linking the two transition metal octahedra in the perovskite layers. This selective oxygen removal results in a novel square-pyramidal coordination of the trivalent ion when the stoichiometry reaches 6, while the tetragonal structure is retained. In the case of the Co-containing phase, the oxygen stoichiometry could be as high as 6.06 and as low as 5.78, which implies predominantly Co(III). These reports did not include any information regarding their electrical properties. We should also note that a paper by Mizutani *et al.* in 1970 (in Japanese) reported the synthesis and XRD data of the Mn-containing phase.[97]

With this background in mind, an approach that now became feasible involved the synthesis and study of the electrical properties of the members of the $Sr_3Ti_2O_7$-$Sr_3M_2O_{7-\delta}$ (M=Ga, Al, In, Co, Fe, Mn) solid solution. This sort of idea has been successfully tested by Tuller and coworkers in their studies of the pyrochlore system based on $Gd_2Ti_2O_7$, as mentioned previously.[24, 27, 28, 98, 99] Our final goal is the synthesis of a family of electrical conductors where, by changing the identity of the doped cation, we can control the relative magnitudes of the ionic and electronic conductivity in the system. If successful, it would allow an all $Sr_3Ti_2O_7$-based graded SOFC.

We also wanted to answer other fundamental questions. We were interested to see if we would have problems with the synthesis of new doped phases because of the presence of secondary phases, similarly to what was reported for the n=2 Aurivillius phases. We were also curious to see what levels of oxygen nonstoichiometry we could achieve in such solid solutions, or to put it differently, the levels of solubility of the proposed dopant cations into the structure. Also, as the concentration of transition metal cation is increased, either the oxidation state of the transition metal increases (i.e. from III to IV), maintaining low levels of oxygen nonstoichiometry, or the generation of oxygen vacancies predominates. In the latter case, the

concentration of oxygen vacancies that can be achieved by this method is very high (about 1 in 7 or 17% assuming an oxidation state of +3). This concentration of oxygen vacancies is considerably higher than could be achieved by doping with fixed-valent dopants such as Al and Ga, in view of the fact that $Sr_3M_2O_6$ (M=Al, Ga) is known but has a different structure. The potential for higher levels of oxygen ion conductivity is clear, to complement the electronic conductivity that presumably is present in these systems. In the former case, the possibility exists that a new family of transition metal oxides with high oxidation states will be found. Since Co(IV)-containing materials are not very common, this possibility is of intrinsic interest.

At first, we mainly concentrated on obtaining purely ionic conductors, and therefore we substituted fixed-valent cations such as Al^{3+} and Ga^{3+}. As will be discussed later in this thesis, the conductivity of these doped materials is fairly low.[100] We then turned our attention to the transition metal-doped Ruddlesden-Popper phases. These materials show much higher values of conductivity, as well as other interesting properties.

References

1. Gottschalk, M. A., *Will fuel cells power an automotive revolution?*, Design News, 6/22/98, pp. 86-96.

2. Hamnett, A., *Phil. Trans. R. Soc. Lond. A,* **1996**, *354*, 1653-1669.

3. Naughton, K., *Detroit's impossible dream?*, Business Week, March 2, 1998, pp. 66-67.

4. Badwal, S. P. S. and Foger, K., *Ceramics International,* **1996**, *22*, 257-265.

5. Appleby, A. J., *Energy,* **1996**, *21*, 521-653.

6. Labrincha, J. A., Frade, J. R. and Marques, F. M. B., *J. Mater. Sci.,* **1993**, *28*, 3809-3915.

7. Tuller, H. L., in *High Temperature Electrochemistry: Ceramics and Metals,* F. W. Poulsen, N. Bonanos, S. Linderoth, M. Mogensen and B. Zachau-Christiansen, Eds. (Riso National Laboratory, Roskilde, Denmark, 1996), pp. 139-153.

8. Minh, N. Q., *Chemtech,* **1991**, 120-126.

9. Kilner, J. A., *Bol. Soc. Esp. Ceram. Vidrio,* **1998**, *37*, 247-255.

10. Bouwmeester, H. J. M. and Burggraaf, A. J., in *The CRC Handbook of Solid State Electrochemistry,* P. J. Gellings and H. J. M. Bouwmeester, Eds. (CRC Press, Boca Raton, 1997), pp. 481-553.

11. Kendall, K. R., Navas, C., Thomas, J. K. and zur Loye, H.-C., *Chem. Mater.,* **1996**, *8*, 642-649.

12. Kendall, K. R., Navas, C., Thomas, J. K. and zur Loye, H.-C., *Solid State Ionics,* **1995**, *82*, 215-223.

13. Etsell, T. H. and Flengas, S. N., *Chem. Rev.,* **1970**, *70*, 339-376.

14. Steele, B. C. H., *Mater. Sci. Eng. B- Solid State M.,* **1992**, *13*, 79-87.

15. Catlow, C. R. A., in *Superionic Solids and Solid Electrolytes,* A. L. Laskar and S. Chandra, Eds. (Academic Press, New York, 1989), pp. 339-379.

16. Blumenthal, R. N., Lee, P. W. and Panlener, R. J., *J. Electrochem. Soc.,* **1971**, *118*, 123-129.

17. Kudo, T. and Obayashi, H., *J. Electrochem. Soc.,* **1976**, *123*, 415-419.

18. Godickemeier, M., Ph.D. Thesis, Swiss Federal Institute of Technology, 1996

19. Kudo, T., in *The CRC Handbook of Solid State Electrochemistry,* P. J. Gellings and H. J. M. Bouwmeester, Eds. (CRC Press, Boca Raton, 1997), pp. 195-221.

20. Takahashi, T. and Iwahara, H., *J. Appl. Electrochem.,* **1973**, *3*, 65-72.

21. Takahashi, T., Iwahara, H. and Arao, T., *J. Appl. Electrochem.,* **1975**, *5*, 187-195.

22. Takahashi, T., Esaka, T. and Iwahara, H., *J. Appl. Electrochem.,* **1975**, *5*, 197-202.

23. Takahashi, T. and Iwahara, H., *Mat. Res. Bull.,* **1978**, *13*, 1447-1453.

24. Kramer, S., Spears, M. and Tuller, H. L., *Solid State Ionics,* **1994**, *72*, 59-66.

25. Kramer, S. A. and Tuller, H. L., *Solid State Ionics,* **1995**, *82*, 15-23.

26. Porat, O., Spears, M. A., Heremans, C., Kosacki, I. and Tuller, H. L., *Solid State Ionics,* **1996**, *86-88*, 285-288.

27. Porat, O., Heremans, C. and Tuller, H. L., *Solid State Ionics,* **1997**, *94*, 75-83.

28. Moon, P. K. and Tuller, H. L., *Solid State Ionics,* **1988**, *28-30*, 470-474.

29. Mohan Ram, R. A., Ganapathi, L., Ganguly, P. and Rao, C. N. R., *J. Solid State Chem.,* **1986**, *63*, 139-147.

30. Takahashi, T. and Iwahara, H., *Energy Convers.,* **1971**, 105-111.

31. Anderson, M. T., Vaughey, J. T. and Poeppelmeier, K. R., *Chem. Mater.,* **1993**, *5*, 151-165.

32. Ishihara, T., Matsuda, H. and Takita, Y., *J. Am. Chem. Soc.,* **1994**, *116*, 3801-3803.

33. Ishihara, T., Matsuda, H., Mizuhara, Y. and Takita, Y., *Solid State Ionics,* **1994**, *70/71*, 234-238.

34. Ishihara, T., Matsuda, H. and Takita, Y., *J. Electrochem. Soc.,* **1994**, *141*, 3444-3449.

35. Huang, K., Feng, M., Goodenough, J. B. and Milliken, C., *J. Electrochem. Soc.,* **1997**, *144*, 3620-3624.

36. Goodenough, J. B., Ruiz-Diaz, J. E. and Zhen, Y. S., *Solid State Ionics,* **1990**, *44*, 21-31.

37. Adler, S. B., Reimer, J. A. and Baltisberger, J., et al., *J. Am. Chem. Soc.,* **1994**, *116*, 675.

38. Baiker, A., Marti, P. E., Keusch, P., Fritsch, E. and Reller, A., *J. Catal.,* **1994**, *146*, 268-276.

39. Barton, J., *Collect. Czech. Chem. Commun.,* **1990**, *55*, 1928-1934.

40. Barton, J., *Collect. Czech. Chem. Commun.,* **1990**, *55*, 1935-1942.

41. Kojima, I., Adachi, H. and Yasumori, I., *Surface Science,* **1983**, *130*, 50-62.

42. Alcock, C. B., Doshi, R. C. and Shen, Y., *Solid State Ionics,* **1992**, *51*, 281-289.

43. Anderson, H., *Solid State Ionics,* **1992**, *52*, 33-41.

44. Minh, N. Q., *J. Amer. Ceramic. Soc.,* **1993**, *76*, 563-588.

45. Mizusaki, J., *Solid State Ionics,* **1992**, *52*, 79-91.

46. Yokokawa, H., Sakai, N., Kawada, T. and Dokiya, M., *Solid State Ionics,* **1992**, *52*, 43-56.

47. Mizusaki, J., Mima, Y., Yamauchi, S., Fueki, K. and Tagawa, H., *J. Solid State Chem.,* **1989**, *80*, 102-111.

48. Mizusaki, J., Sasamoto, T., Cannon, W. R. and Bowen, H. K., *J. Amer. Ceram. Soc.,* **1983**, *66*, 247-252.

49. Teraoka, Y., Zhang, H. M., Furukawa, S. and Yamazoe, N., *Chem. Lett.,* **1985**, 1743-1746.

50. Teraoka, Y., Nobunaga, T. and Yamazoe, N., *Chem. Lett.,* **1988**, 503-506.

51. Teraoka, Y., Nobunaga, T., Okamoto, T., Miura, N. and Yamazoe, N., *Solid State Ionics*, **1991**, *48*, 207-212.

52. Ma, B., U., B., Park, J.-H. and Segre, C. U., *J. Electrochem. Soc.*, **1996**, *143*, 1736-1744.

53. Ma, B., Park, J.-H. and Balachandran, U., *J. Electrochem. Soc.*, **1997**, *144*, 2816-2823.

54. Guggilla, S. and Manthiram, A., *J. Electrochem. Soc.*, **1997**, *144*, L120-L122.

55. Aurivillius, B., *Arkiv. Kemi*, **1949**, *1*, 463-480.

56. Aurivillius, B., *Arkiv. Kemi*, **1949**, *1*, 499-512.

57. Aurivillius, B., *Arkiv. Kemi*, **1950**, *2*, 519-527.

58. Subbarao, E. C., *J. Amer. Ceram. Soc.*, **1962**, *45*, 166-169.

59. Barrault, J., Grosset, C., Dion, M., Ganne, M. and Tournoux, M., *Catal. Lett.*, **1992**, *16*, 203-210.

60. Batist, P. A., Bouwens, J. F. H. and Schuit, G. C. A., *J. Catal.*, **1972**, *25*, 1-11.

61. Takahashi, T., Esaka, T. and Iwahara, H., *J. Appl. Electrochem.*, **1977**, *7*, 31-35.

62. Abraham, F., Debreuille-Gresse, M. F., Mairesse, G. and Nowogrocki, G., *Solid State Ionics*, **1988**, *28-30*, 529-532.

63. Abraham, F., Boivin, J. C., Mairesse, G. and Nowogrocki, G., *Solid State Ionics*, **1990**, *40/41*, 934-937.

64. Anne, M., Bacmann, M., Pernot, E., Abraham, F., Mairesse, G. and Strobel, P., *Physica B*, **1992**, *180 & 181*, 621-623.

65. Dygas, J. R., Krok, F., Bogusz, W., Kurek, P., Reiselhuber, K. and Breiter, M. W., *Solid State Ionics*, **1994**, *70/71*, 239-247.

66. Essalim, R., Tanouti, B., Bonnet, J.-P. and Reau, J. M., *Mater. Lett.*, **1992**, *13*, 382-386.

67. Goodenough, J. B., Manthiram, A., Parantham, M. and Zhen, Y. S., *Mater. Sci. Eng. B- Solid State M.*, **1992**, *12*, 357-364.

68. Iharada, T., Hammouche, A., Fouletier, J., Kleitz, M., Boivin, J. C. and Mairesse, G., *Solid State Ionics*, **1991**, *48*, 257-265.

69. Lee, C. K., Tan, M. P. and West, A. R., *J. Mater. Chem.*, **1994**, *4*, 525-528.

70. Pernot, E., Anne, M., Bacmann, M., Strobel, P., Fouletier, J., Vannier, R. N., Mairesse, G., Abraham, F. and Nowogrocki, G., *Solid State Ionics*, **1994**, *70/71*, 259-263.

71. Sharma, V., Shukla, A. K. and Gopalakrishnan, J., *J. Mater. Chem.*, **1994**, *4*, 703-705.

72. Sharma, V., Shukla, A. K. and Gopalakrishnan, J., *Solid State Ionics*, **1992**, *58*, 359-362.

73. Vannier, R. N., Mairesse, G., Nowogrocki, G., Abraham, F. and Boivin, J. C., *Solid State Ionics*, **1992**, *53-56*, 713-722.

74. Bush, A. A. and Venevtsev, Y. N., *Russ. J. Inorg. Chem.*, **1986**, *31*, 1346-1348.

75. Pham, A.-Q., Puri, M., DiCarlo, J. F. and Jacobson, A. J., *Solid State Ionics*, **1994**, *72*, 309-313.

76. Thomas, J. K., Kendall, K. R. and zur Loye, H. C., *Solid State Ionics*, **1994**, *70/71*, 225-228.

77. Kendall, K. R., Thomas, J. K. and zur Loye, H. C., *Chem. Mater.*, **1995**, *7*, 50-57.

78. Kendall, K. R., Navas, C. and zur Loye, H.-C., *Bi$_2$Sr$_2$M'$_2$M"O$_{11.5}$ [(M' = Nb, Ta) and (M" = Al, Ga)], Synthesis and Characterization of oxygen-deficient Aurivillius Phases*, G.-A. Nazri, J.-M. Tarascon and M. Armand, Eds., (MRS, Materials Research Society Symposium Proceedings: Solid State Ionics IV, Boston, MA, 1995), Vol. 369, pp. 355-360.

79. Kendall, K. R., Thomas, J. K. and zur Loye, H. C., *Solid State Ionics*, **1994**, *70/71*, 221-224.

80. Ruddlesden, S. N. and Popper, P., *Acta Cryst.*, **1957**, *10*, 538-539.

81. Ruddlesden, S. N. and Popper, P., *Acta Cryst.*, **1958**, *11*, 54-55.

82. Bednorz, J. G. and Muller, K. A., *Z. Phys. B,* **1986**, *64*, 189.

83. Hauck, J. and MIka, K., *Intl. J. Mod. Phys. B,* **1993**, *7*, 3423-3433.

84. Kinoshita, K., Izumi, F., Yamada, T. and Asano, H., *Phys. Rev.,* **1992**, *B45*, 5558-5562.

85. Cava, R. J., Batlogg, B., can Dover, R. B., Krajewski, J. J., Waszczak, J. V., Fleming, R. M., Peck, W. F., Jr., Rupp, L. W., Jr., Marsh, P., James, A. C. W. P. and Schneemeyer, L. F., *Nature,* **1990**, *345*, 602.

86. Sarjeant, G. M., Greenwood, K. B., Poeppelmeier, K. R., Zhang, H., Salvador, P. A., Mason, T. O. and Marks, L. D., *Chem. Mater.,* **1996**, *8*, 2792-2798.

87. Battle, P. D., Green, M. A., Laskey, N. S., Millburn, J. E., Murphy, L., Rosseinsky, M. J., Sullivan, S. P. and Vente, J. F., *Chem. Mater.,* **1997**, *9*, 552-559.

88. Seshadri, R., Martin, C., Hervieu, M., Raveau, B. and Rao, C. N. R., *Chem. Mater.,* **1997**, *9*, 270-277.

89. Turrillas, X., Sellars, A. P. and Steele, B. C. H., *Solid State Ionics,* **1988**, *28-30*, 465-469.

90. Poulsen, F. W. and van der Puil, N., *Solid State Ionics,* **1992**, *53-56*, 777-783.

91. Kendall, K. R., Ph.D. Thesis, Massachusetts Institute of Technology, 1996

92. Gallagher, P. K., *Inorg. Chem.,* **1965**, *4*, 965.

93. Gallagher, P. K., MacChesney, J. B. and Buchanan, D. N. E., *J. Chem. Phys.,* **1966**, *45*, 2466-2471.

94. Gallagher, P. K. and Kurkjian, C. R., *Inorg. Chem.,* **1966**, *5*, 214.

95. Dann, S. E., Weller, M. T. and Currie, D. B., *J. Solid State Chem.,* **1992**, *97*, 179-185.

96. Dann, S. E. and Weller, M. T., *J. Solid State Chem.,* **1995**, *115*, 499-507.

97. Mizutani, *J. Chem. Soc. (Japan) Ind. Ed.,* **1970**, *73*, 1097-1103.

98. Tuller, H. L., *Solid State Ionics,* **1992**, *52*, 135-146.

99. Sprague, J. J., Porat, O. and Tuller, H. L., *Sensors and Actuators,* **1996,** *B35,* 348-352.

100.   Navas, C. and zur Loye, H. C., *Solid State Ionics,* **1997,** *93,* 171-176.

Chapter 3. Theory

3.1. Mechanism of oxygen ion conductivity

Critical to the success of our research is the ability to effect the electrical properties of the materials under study. In our case, such properties are directly dependent on the motion of charge carrying species. Consequently, it is essential to control parameters such as oxygen nonstoichiometry, and key defect concentrations. This section provides an overview of the theory of ionic and mixed ionic and electronic conductivity.

3.1.1. Electrical conductivity

The partial electrical conductivity, σ, of species j is defined by equation 3.1

$$\sigma_j = \mu_j \cdot n_j \cdot Z_j \cdot e \qquad (3.1)$$

where μ is the mobility, n is the concentration of charge carriers, and Z is the charge of the carrier (e.g. -2 for O^{2-}). Then, the total conductivity in a solid is given by

$$\sigma_{tot} = \sum_j \sigma_j \qquad (3.2)$$

where, for our purposes, the charge carriers may be electrons, holes and oxide ions. In this case, equation 3.2. becomes

$$\sigma_{tot} = \sigma_i + \sigma_n + \sigma_p \qquad (3.3)$$

where σ_i represents the ionic conductivity and σ_n and σ_p represent the electron and hole conductivities, respectively. A new quantity, the ionic transference number, may be defined as

$$t_i = \frac{\sigma_i}{\sigma_{tot}} \qquad\qquad (3.4)$$

The transference number indicates the relative contributions of ionic charge carriers to the total conductivity. One can similarly define a transference number for electrons and holes. We should point out that all solid oxides exhibit some degree of both ionic and electronic conduction. When we refer to a material as an ionic conductor, it implies that the level of electronic conductivity is very low compared to that of the ionic conductivity. When talking about electronic conductors, the implication is that the magnitude of the ionic conductivity is negligible when compared to the electronic component. Mixed conductors (e.g. $La_{1-x}Sr_xMO_{3-\delta}$, M=Co, Fe, Mn) typically exhibit electronic conductivities orders of magnitude higher than the ionic, as transference number measurements show.[1] However, the level of ionic conductivity, while much lower than the electronic, is still high when compared to other ionic conductors, and may play a significant role.

We now concentrate on equation 3.1. Since $Z_j e$ is constant, it is clear that the two parameters one needs to control in order to influence the conductivity are the mobility and the concentration of charge carriers. In the case of electrons and holes, these parameters are determined by the electronic structure of the material. Since we are interested in both ionic and mixed conductors, controlling the magnitude of the electronic conductivity is important. This is not always easy to do; however, for most practical purposes, the magnitude of electronic conductivity is not the overriding factor.

The factors that are of concern regarding the electronic conductivity are the degree of orbital overlap, the degree of electron localization and the number of charge carriers. The first two could very well be grouped in the same category. The lower the orbital overlap, the less shared the electrons are between the valence orbitals, and the more localized the electrons are. In

this case, the electronic conductivity will likely take place via a hopping-type mechanism. It involves electrons jumping or "hopping" between valence orbitals of adjacent atoms. The other extreme case is that of a metal, where there is a large degree of orbital overlap and the electrons are very delocalized, so that motion is very facile.

Regarding the number of charge carriers, they are related to the number of valence electrons in d orbitals. [*Note*: We are restricting ourselves to transition metals, typically of the first-row, and hence we only make references to d orbitals.] If the valence band is nearly completely filled and the conduction band is nearly completely empty, then electrons cannot move freely and either semiconducting or insulating behavior ensues, depending on the energy gap between the valence and conduction bands. In the case of semiconductors, the charge carriers may be electrons in the conduction band or holes in the valence band, giving rise to n-type or p-type electronic conductivity, respectively. In the case of insulators, the band gap energy is large enough so that there is little promotion of electrons from the top of the valence band to the bottom of the conduction band. This situation may be altered through the addition of appropriate dopants to extrinsically introduce defects such as holes in the valence band or electrons in the conduction band.

Most titanates materials may be characterized as semiconductors with band gaps of 3-4 eV as illustrated by $SrTiO_3$ and $Gd_2Ti_2O_7$. The first material, with the perovskite structure, is directly related to $Sr_3Ti_2O_7$, since it is the n= ∞ member of the Ruddlesden-Popper family of materials. Its band gap is about 3.3-3.4 eV,[2] while that of the pyrochlore composition is 3.48 eV.[3] To our knowledge, the band gap of $Sr_3Ti_2O_7$ has not been reported in the literature, but clearly one may assume that the value of its band gap lies around the same value, given the similarities in structure and bonding with $SrTiO_3$. Therefore, $Sr_3Ti_2O_7$ may also be characterized as a large

gap semiconductor. Later in this chapter we outline a way to determine the bandgap energy within the framework of our studies.

If instead of Ti^{4+}, which has no electrons in its d orbitals, a different transition metal cation is occupying the same octahedral site, the presence of valence electrons will have a marked effect on the electronic transport properties. For example, related $n= 2$ Ruddlesden-Popper phases of general formula $Sr_{3-x}A_xFe_2O_7$ (A= Ba, La; x $\leq$ 0.4) have been reported as semiconductors with small activation energies of about 0.11 eV.[4] The electronic transport properties were described on the basis of weakly localized electrons. Similarly, other related cobaltates of general formula $Ln_2MCo_2O_7$ (Ln= Sm, Gd; M= Sr, Ba) have been reported. Their resistance at room temperature is about 5 Ω·cm and they were all characterized as semiconductors. Consequently, one should expect higher electronic conductivities in the Co and Fe-containing $n= 2$ Ruddlesden-Popper phases than in the parent titanate material.

3.1.2. Ionic conduction mechanism

We restrict ourselves to solid oxides and oxide ion conduction, although the principles outlined in the following section are valid as well for other ionic species (e.g. Li^+, Na^+...).

The mechanism by which an oxygen vacancy may move across the lattice is depicted in Figure 3.1. An oxide ion "jumps" or "hops" from an occupied site to an adjacent vacant site via a thermally activated process. As the oxide ion moves, it passes through an interstitial space within the structure, with a potential energy barrier. This "open volume" available for the oxide ion to pass through has been identified as one of the critical parameters in determining the feasibility of a material as an oxide ion conductor.[5] It obviously has a direct impact on the activation energy,

Figure 3.1. Hopping mechanism of oxide ions

⬤ = Oxide ion   ☐ = Oxygen vacancy
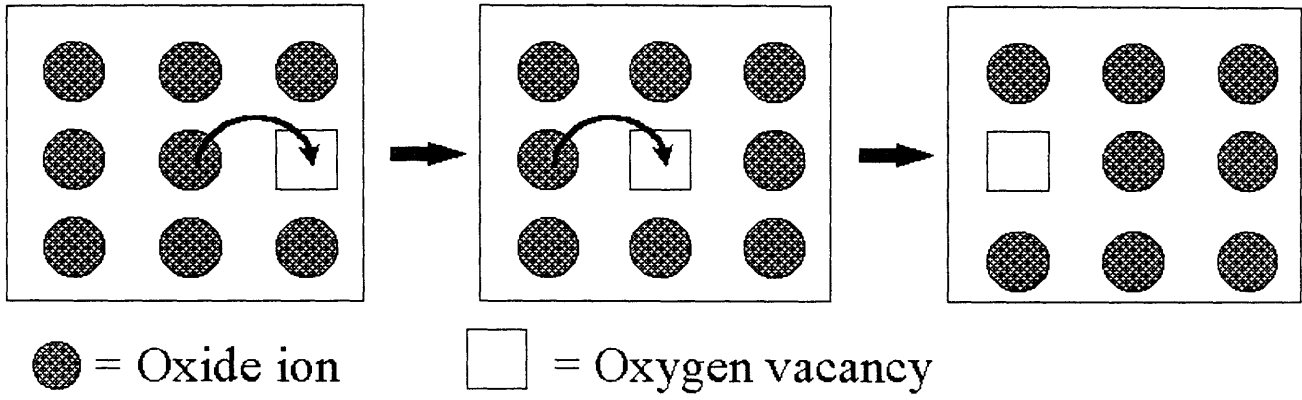
E_a, required for the hopping motion. The mobility depends directly on this parameter and may be expressed by equation 3.5

$$\mu = \mu_0 \exp\left(\frac{-E_a}{kT}\right)$$ (3.5)

where μ_o is the pre-exponential factor, E_a the activation energy and T the temperature in degrees Kelvin. The pre-exponential factor includes factors such as the attempt frequency, the jump distance, the number of unoccupied neighboring sites as well as other geometric and correlation effects. Combining equations 3.1 and 3.6 one obtains

$$\sigma = \frac{\sigma_0}{T} \exp\left(\frac{-E_a}{kT}\right)$$ (3.6)

This Arrhenius-type expression allows one to obtain E_a by plotting ln ($\sigma*T$) vs. 1/T and extracting the slope. The intercept of the line on the ordinate corresponds to the pre-exponential term, σ_0.

Geometrical arguments have been made regarding ways to improve the mobility in oxide ion conductors. Since ionic conduction is controlled by the motion of oxide ions throughout the lattice, a larger space through which the anion can move will increase its mobility. Kilner and Brook looked at this concept of "free volume", and suggested, in certain cases, using larger cations to induce the close-packed oxide anions to move apart.[6] A similar argument can be made regarding the polarizability of the cations. A more polarizable ion (e.g. Bi^{3+} vs. La^{3+}) will improve oxide ion mobility by minimizing the disturbance of the lattice potential upon the "hopping" of the oxide ion from an occupied site (lower in energy), through a "hole" in the structure (higher energy) and into a vacant site.[7] In fact, this is presumed to be one of the reasons that Bi_2O_3 is such a good oxide ion conductor.[8]

Besides improving mobility of oxide ions, the other factor that may be more easily controllable is the concentration of oxygen vacancies. At temperatures above 0 K, all oxides have oxygen vacancies due to the entropy of the system. They may be of different types. For example, Schottky defects consist of vacancies in the lattice (both anionic and cationic, in order to preserve overall electroneutrality). Frenkel defects, on the other hand, involve the generation of an oxygen vacancy and an oxygen interstitial. This process is given by equation 3.7

$$O_o^x \rightarrow O_i^{''} + V_o^{\cdot\cdot} \tag{3.7}$$

These types of oxygen vacancies are intrinsic to the system. Their presence and whether they are ordered or not may become critical in determining whether a compound is a good ionic conductor. Perhaps this is best exemplified by the pyrochlore materials, specifically $Gd_2M_2O_7$ (M= Ti, Zr). The oxygen vacancies in the titanate member are highly ordered, and the material is not a very good ionic conductor, whereas the zirconate displays a much higher degree of disorder and is a much better oxygen ion conductor.

Oxygen vacancies may further be introduced by doping into the structure. For example, for an oxide with general formula MO, doping with a cation, M', of valence +1, will create oxygen vacancies (e.g. $M_{1-x}M'_xO_{1-\delta}$) in order to maintain electroneutrality. These oxygen vacancies will then be extrinsic. YSZ is an example of a material where vacancies have been introduced extrinsically. We note that by controlling x in the example, one also controls the value of δ, and the concentration of oxygen vacancies.

As we have seen, the two parameters that determine ionic conductivity (mobility of the oxide ion and concentration of oxygen vacancies) can be varied to some degree by appropriate choice of structural types and dopant cations.

3.1.3. Chemical diffusion

In this section, we derive a relationship between the conductivity and the chemical diffusion coefficient of a charge carrier. The treatment described below follows that of Heyne[9] and Weppner.[10]

Chemical diffusion is a process in which the transport of coupled species within a solid is involved. In general, the flux density of species j (in particles per square centimeter second) in a solid is given by Fick's first law of diffusion

$$j_j = -\tilde{D}_j \frac{\partial c_j}{\partial x} \qquad (3.8)$$

where $\tilde{D}_j$ is the chemical diffusion coefficient of species j and c_j represents the concentration of species j. The chemical diffusion coefficient of the solid represents a weighed average of the chemical diffusion coefficients of all species contributing to the transport phenomena. In the case of a mixed ionic and electronic conductor, where the overall conduction process is the sum of the contributions from the oxide ions and an electronic charge carrier (e.g. holes), the chemical diffusion coefficient may also be represented by the following equation:

$$\tilde{D} = t_e \, D_i + t_i \, D_e \qquad (3.9)$$

where $\tilde{D}$ is the overall chemical diffusion coefficient, t_i and t_e represent the ionic and electronic transference numbers and D_i and D_e represent the diffusion coefficients of oxide ions and holes, respectively. Usually electronic charge carriers are much more mobile than ionic defects, so that $D_e \gg D_i$ is a valid approximation. Furthermore, if under certain conditions of temperature

74

and oxygen partial pressure the conductivity is predominantly electronic ($t_e \approx 1$), equation 3.9

reduces to:

$$\tilde{D} = D_i \tag{3.10}$$

This result implies that the measurement of the chemical diffusion coefficient in a material under

the conditions specified above can provide the diffusion coefficient of the ionic species. The

diffusion coefficient of species j is related to the mobility by the following equation:

$$\mu_j = \frac{z_j e D_j}{kT} \tag{3.11}$$

Equation 3.11 is a form of the Nernst-Einstein relation. By substituting it into equation 3.1, the

conductivity of species j can also be given by

$$\sigma_j = \frac{D_j z_j^2 e^2 c_j}{kT} \tag{3.12}$$

3.2. Defect notation

The charges of defects in solids, as well as those of the component particles, are

important with respect to the neutral lattice. Therefore, the oxide ion (O^{2-}), in an oxide lattice, is

considered to be effectively neutral. The defect notation most commonly used is that introduced

by Kroger and Vink.[11, 12] A positive excess charge is indicated by a dot (˙), while the excess

negative charge is denoted with a prime symbol ('), as superscripts. Table 3.1 summarizes the

point defect notation using a compound with general formula $M^{2+}X^{2-}$ as an example.

Table 3.1. Kroger-Vink notation for point defects in crystals of general formula MX, where M^{2+} and X^{2-} represent the cation and anion, respectively.

Type of defect	Symbol	Remarks
Vacant M site	$V_M^{''}$	
Vacant X site	$V_X^{\cdot\cdot}$	
Ion on lattice site	M_M^x, X_X^x	^{x}: uncharged
L on M site	$L_M^{'}$	L^+ dopant ion
N on M site	$N_M^{\cdot}$	N^{3+} dopant ion
Free electron	e'	
Free hole	$h^{\cdot}$	
Interstitial M ion	$M_i^{\cdot\cdot}$	$^{\cdot}$: effective positive charge
Interstitial X ion	$X_i^{''}$	$^{''}$: effective negative charge

3.3. Defect chemistry of nonstoichiometric oxides

In this section we consider the defect chemistry of an oxide where a dopant of either fixed or variable valence has been introduced. Here I summarize the treatment of this problem given by Tuller.[13]

When studying ionic and mixed ionic and electronic conductors, it is critical to identify the various possible charge carriers. In order to do so, a knowledge of basic dependence of chemical defects on parameters such as temperature and oxygen partial pressure (in the case of oxides) becomes critical. Examining and interpreting the dependence of conductivity on those parameters becomes easier by considering which defects dominate under certain conditions.

In general, a number of point defects will be present according to various conditions of T and p(O₂). Frenkel disorder in the oxygen sublattice can be represented in the form of Equation 3.13, using Kroger-Vink notation[12]

$$O_o^x \leftrightarrow O_i^{''} + V_o^{\cdot\cdot} \tag{3.13}$$

where O_o^x, $O_i^{''}$ and $V_o^{\cdot\cdot}$ represent a lattice oxide ion, an interstitial oxide ion and an oxygen vacancy, respectively. We also must consider electron-hole pair generation, described by Equation 3.14

$$0 \leftrightarrow e^{'} + h^{\cdot} \tag{3.14}$$

as well as the equilibrium with the gas phase (Equation 3.15)

$$O_o^x \leftrightarrow V_o^{\cdot\cdot} + \frac{1}{2}O_2(g) + 2e^{'} \tag{3.15}$$

We shall now consider the introduction into the structure of a dopant cation, N_M', with a valence

one less than the host cation for which it is substituting. In such a case, all the charged defects

must balance, and the electroneutrality equation reads as follows:

$$n + 2[O_i''] + [N_M'] = p + 2[V_o^{..}] \tag{3.16}$$

The mass-action relations for Equations 3.13-3.15 are, respectively,

$$[O_i''] \cdot [V_o^{..}] = K_F = K_F^0 \exp\left(-E_F/kT\right) \tag{3.17}$$

$$np = K_i = N_c N_v \exp\left(-E_g/kT\right) \tag{3.18}$$

$$[V_o^{..}] \cdot n^2 P_{O_2}^{1/2} = K_R = K_R^0 \exp\left(-E_R/kT\right) \tag{3.19}$$

We would like to obtain a set of relationships between the concentration of each particular

defect, T, p(O$_2$) and $[N_M']$. In order to obtain such relationships, it becomes easier to simplify the

above equations by using the Brouwer approach,[14] whereby one recognizes that only one defect

on each side of equation 3.16 dominates for a given set of experimental conditions. For example,

high oxygen pressures result in the formation of $h^.$ and O_i'' and equation 3.16 reduces to

$p = 2[O_i'']$. On the other hand, low oxygen pressures lead to the formation of e' and $[V_o^{..}]$, and

equation 3.16 instead reduces to $n = 2[V_o^{..}]$.

In all, four regions with their corresponding neutrality relations may be observed in the

case of a fixed-valent dopant. The region of particular interest for our purposes is given by the

relation $2[V_o^{..}] = [N_M']$, which implies that $[V_o^{..}]$ is virtually constant with respect to p(O$_2$), since it

depends strictly on $[N_M']$. The dependence of the concentration of defects of interest on oxygen

partial pressure in this regime is depicted in Figure 3.2.

Figure 3.2. Dependence of charge-carrying defects on oxygen partial pressure for an oxide doped with a fixed-valent cation
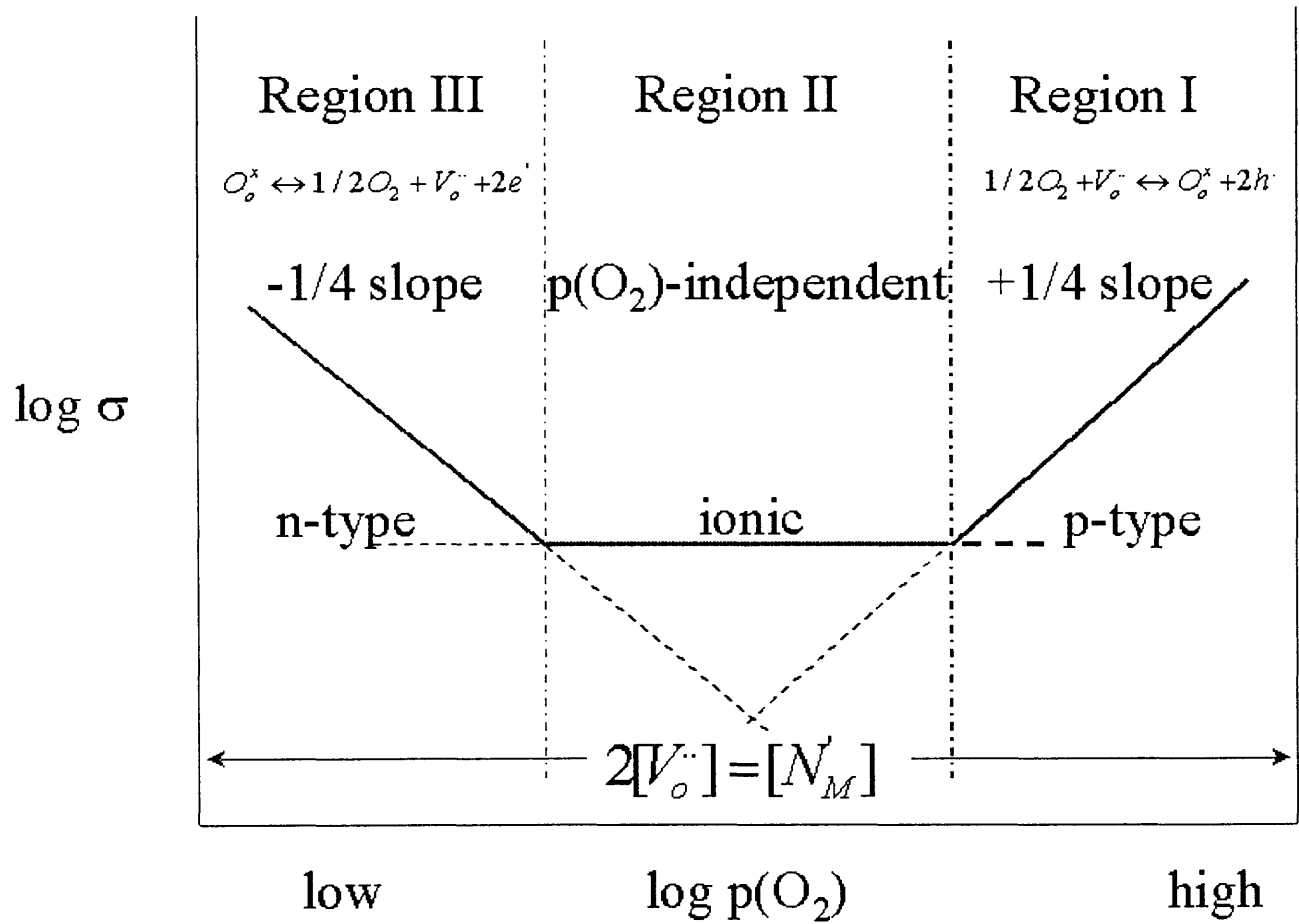
Within the regime defined by $2[V_O^{\cdot\cdot}] = [N_M']$, three distinct subregions may be observed.

At high oxygen pressures, insertion of oxygen into the lattice (oxygen vacancies) produces holes

via the following equilibrium

$$\tfrac{1}{2}O_2(g) + V_O^{\cdot\cdot} \leftrightarrow O_o^x + 2h^{\cdot} \tag{3.20}$$

where one may write

$$K_{ox} = \frac{[h^{\cdot}]^2[O_o^x]}{[V_O^{\cdot\cdot}]p(O_2)^{\frac{1}{2}}} \tag{3.21}$$

and rearranging, one may easily derive that

$$[h^{\cdot}] \propto p(O_2)^{\frac{1}{4}} \tag{3.22}$$

which shows the dependence of holes on oxygen partial pressure follows a slope of +1/4 (on a

log scale). Similarly, at low oxygen partial pressures, oxygen leaves the lattice via the following

equilibrium

$$O_o^x \rightarrow \tfrac{1}{2}O_2(g) + 2e^- + V_o^{\cdot\cdot} \tag{3.23}$$

producing electrons. Therefore,

$$K_R = \frac{[V_o^{\cdot\cdot}][e']^2 p(O_2)^{\frac{1}{2}}}{[O_o^x]} \tag{3.24}$$

Equation 3.24 may be also rearranged to show that

$$[e'] \propto p(O_2)^{-\frac{1}{4}} \tag{3.25}$$

As can be seen in Figure 3.2, the oxygen vacancies in the entire regime show no dependence on

oxygen partial pressure, as they are fixed by the concentration of dopant cations. Thus, in this

manner, one can determine the charge carriers responsible for the conductivity observed by

measuring and determining the dependence of the conductivity of a material as a function of

oxygen partial pressure, and identifying the region to which it corresponds. The total conductivity will then be given by

$$\sigma_{tot} = A \cdot p(O_2)^{\frac{1}{4}} + B + C \cdot p(O_2)^{-\frac{1}{4}} \qquad (3.26)$$

where one can easily extract the ionic conductivity from $\sigma_i = B$. Furthermore, the enthalpies of oxidation and reduction may be also extracted from the dependence of the parameters A and C on temperature, respectively. For example, using equation 3.26 the electronic conductivity is given by

$$\sigma_e = C \cdot p(O_2)^{-1/4} \qquad (3.27)$$

The temperature dependence of the electronic conductivity is given by:

$$\sigma_e = C_o \cdot p(O_2)^{-\frac{1}{4}} \exp\left(-E_c / kT\right) \qquad (3.28)$$

Therefore, a plot of ln C vs. 1/T yields E_c. Using equations 3.19, 3.27 and 3.28, E_c may be related to E_R by

$$\frac{d(\ln K_R)}{d(1/kT)} = \frac{2d(\ln n)}{d(1/kT)} = \frac{2d(\ln \sigma_e)}{d(1/kT)} = -2E_C = -E_R \qquad (3.29)$$

A similar approach shows that the enthalpy of oxidation can be extracted from a plot of ln A vs. 1/T.

The thermal bandgap (E_g) can also be calculated from E_A and E_C by using equation 3.18:

$$\frac{d(\ln K_i)}{d(1/kT)} = \frac{d(\ln n)}{d(1/kT)} + \frac{d(\ln p)}{d(1/kT)} \cong \frac{d(\ln \sigma_e)}{d(1/kT)} + \frac{d(\ln \sigma_h)}{d(1/kT)} = -E_g \qquad (3.30)$$

Taking now equations 3.28 and 3.31

$$\sigma_h = A_o \cdot p(O_2)^{\frac{1}{4}} \exp\left(-E_A / kT\right) \qquad (3.31)$$

and substituting into equation 3.30, one obtains:

$$E_g = E_C + E_A \qquad (3.32)$$

Thus, the thermal bandgap is the sum of the activation energies for the fitting parameters A and C.

The above picture becomes somewhat more complicated if we include the presence of a variable-valence dopant, N_M, which may possess a charge equal to (N_M^x) or one less than (N_M') the host. The corresponding ionization reaction is

$$N_M^x + e' \leftrightarrow N_M' \qquad (3.33)$$

and can also be described by its mass-action relation:

$$\frac{[N_M']}{[N_M^x]n} = K_N(T) = K_N^0 \exp\left(-\frac{E_N}{kT}\right) \qquad (3.34)$$

with the further constraint that the total concentration of the dopant remains constant

$$[N_M^x] + [N_M'] = [N_M]_{tot} = N_t \qquad (3.35)$$

Again, we may use the Brouwer approach to produce a similar set of regimes, as was derived above. In the case of a variable-valence dopant, five such regimes can theoretically be observed (Figure 3.3). We note that now $V_o^{\cdot\cdot}$ shows no p(O$_2$) dependence in only one region (region IV). At the same time, both p and n also show no p(O$_2$) dependence in a different regime (region II). In addition, both regions II and IV are preceded by a region where p-type conductivity shows a slope of +1/6 (regions I and III). Whereas in the case of a fixed-valent dopant it was fairly simple to ascertain the presence of an ionic conductivity region, the task is now more complex. We now have two possibilities that may produce the same kind of dependence with respect to oxygen partial pressure and have completely different origins. A region of decreasing conductivity with decreasing p(O$_2$) which follows a slope of +1/6 on a log scale, followed by a region of

Figure 3.3. Dependence of charge-carrying defects on oxygen partial pressure for an oxide doped with a variable-valent cation
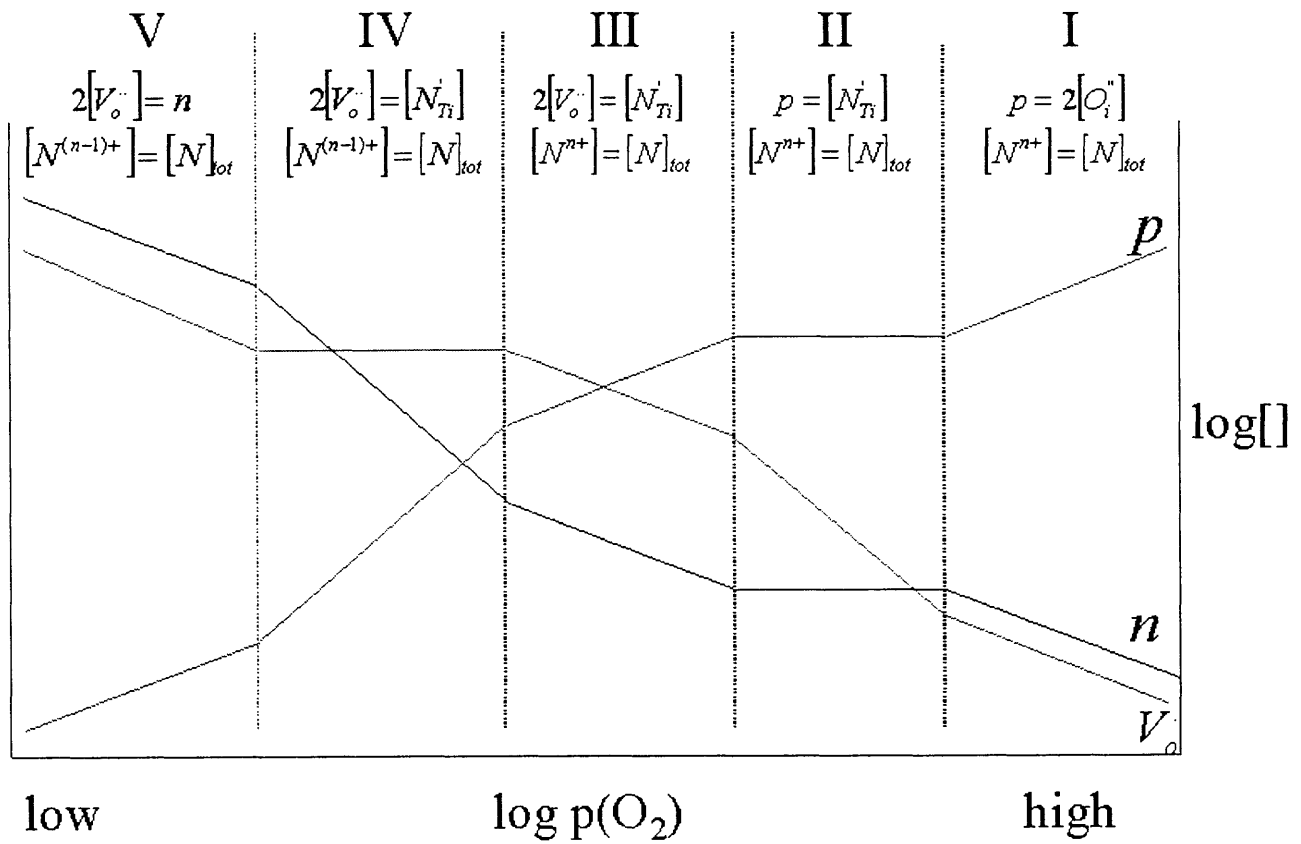
conductivity independent of p(O₂), may be due to regions I and II or to regions III and IV. Consequently, other independent measurements would be needed in other to confirm or deny the presence of an ionic regime in case a p(O₂)-independent region is present. As noted above, both cases are preceded by a region of p-type conductivity of slope +1/6. However, the origin of this p-type region is different for both cases. As can be seen in Figure 3.3, in the transition between regions I and II, there is no change in the oxidation state of the variable-valent dopant, whereas the transition between regions III and IV is accompanied by a one-electron reduction of the dopant.

If region III is observed, where p-type conduction dominates the region, the conductivity may be fit to an equation of the form:

$$\sigma_{tot} = A \cdot p(O_2)^{1/6} \tag{3.36}$$

The dependence of the parameter A on temperature can be used to obtain further information, such as E_N. The p-type regime may be modeled as

$$\sigma_p = A_o \cdot p(O_2)^{1/6} \exp\left(-E_A/{kT}\right) \tag{3.37}$$

Combining equations 3.18, 3.21, 3.34, using $2[V_O^{\cdot\cdot}] = [N_M']$, and assuming that at high p(O₂),

$[N_M^x] = [N_M]_{tot}$, it can be shown that

$$p = \frac{(K_{ox} \cdot K_N \cdot K_i)^{1/3} \cdot [N_M]_t^{1/3} \cdot p(O_2)^{1/6}}{2^{1/3}} \tag{3.38}$$

which can be in turn used to obtain:

$$3E_A = E_{ox} + E_N + E_g \tag{3.39}$$

A knowledge or estimation of E_g and E_{ox} allows to calculate E_N.

The above model and set of equations are valid for dilute solutions, and may only give an approximate model of the defect structure when the dopant content and defect concentrations become large. In this case, the effect of defect band formation should be taken into account in addition to other forms of defect-defect interactions.

Table 3.2. Slope of the dependence of various defects on $p(O_2)$ in the case of variable valence dopants.

Region	n	p	$[V_o^{\cdot\cdot}]$	$[O_i'']$	N_M'
I	-1/6	1/6	-1/6	1/6	-1/6
II	0	0	-½	½	0
III	-1/6	1/6	-1/6	1/6	1/6
IV	-1/4	¼	0	0	0
V	-1/6	1/6	1/6	1/6	0

References

1. Kharton, V. V., Naumovich, E. N., Vecher, A. A. and Nikolaev, A. V., *J. Solid State Chem.,* **1995**, *120*, 128-136.

2. Capizzi, M. and Frova, A., *Phys. Rev. Lett.,* **1972**, *25*, 1298-1301.

3. Spears, M. A. and Tuller, H. L., *Application of defect modeling to materials design,* (Materials Research Society, Boston, 1995), Vol. 369, pp. 271-288.

4. Adler, P., *J. Solid State Chem.,* **1997**, *130*, 129-139.

5. Kilner, J. A. and Brook, R. J., *Solid State Ionics,* **1982**, *6*, 237-252.

6. Kilner, J. A., *The role of dopant size in determining oxygen ion conductivity in the fluorite structure oxides,* R. Metselaar, H. J. M. Heijligers and J. Schoonman, Eds., (Elsevier Scientific Publishing Company, Studies in Inorganic Chemistry, Veldhoven, The Netherlands, 1982), Vol. 3, pp. 189-192.

7. Funke, K., *Z. Phys. Chem.,* **1995**, *188*, 243-257.

8. Takahashi, T. and Iwahara, H., *Mat. Res. Bull.,* **1978**, *13*, 1447-1453.

9. Heyne, L. and den Engelsen, D., *J. Electrochem. Soc.,* **1977**, *124*, 727-735.

10. Weppner, W. and Huggins, R. A., *J. Electrochem. Soc.,* **1977**, *124*, 1569-1578.

11. Kroger, F. A. and Vink, H. J., *Solid State Physics,* **1956**, *3*, 307.

12. Kroger, F. A. *The Chemistry of Imperfect Crystals*; North-Holland Publishing: Amsterdam, 1964.

13. Tuller, H. L., in *Nonstoichiometric Oxides,* O. T. Sorensen, ed. (Academic Press, Inc., New York, 1981), pp. 271-332.

14. Brouwer, G., *Phillips Res. Rep.,* **1954**, *9*, 366.

Chapter 4. Experimental Approach

The first half of my thesis studies was carried out in the zur Loye laboratories, while the second half took place in the Tuller laboratories. Although the basic methods used were the same in both places, the equipment in some cases was different. I tried to minimize whatever differences might have been present due to equipment by using the same kinds of techniques in both labs, and whenever this was not possible, reproducing the appropriate synthetic conditions as well as possible.

4.1. Synthetic techniques

Compounds with the general formula $Sr_{3-x}La_xM_{2-y}M'_yO_{7-\delta}$, M=Ti, Zr; M'=Ga, Al, In, Co, Fe, Mn were synthesized. The synthesis of the parent phases has been reported in the literature and was therefore followed.[1-5] All materials were synthesized by solid state reaction of the corresponding oxides or carbonates. Purity of all starting materials was 99% or better. Table 4.1 shows the starting materials for the elements of interest.

Stoichiometric amounts of starting materials were ground by hand in an agate mortar under acetone for about 15-30 min. Acetone was allowed to evaporate and the homogeneous powder was pressed into a pellet, typically ¾" in diameter. When synthesizing the Fe-doped samples, the loose powder was placed in an alumina crucible. The same could not be done for the Co-containing samples, because they react to form the blue compound $CoAl_2O_4$. Pressing the powders into pellets was helpful to speed the reaction time. The pelletized mixture was placed on a sheet of Pt resting on an alumina tray. It was then introduced inside a tube or box furnace and heated at a rate of 5 °C/min up to 900 °C where it remained for 24 hours. This step has the effect

of converting the carbonates into oxides and partially reacting the starting materials. After

cooling, the resulting pellet/powder was ground to a fine powder and pressed again into a pellet

and placed in a high temperature tube or box furnace, where it was heated at 10 °C/min for

several days. Synthesis conditions are summarized in Table 4.2. Heating steps were continued

until a single phase material was obtained, as determined by X-ray diffraction measurements.

Table 4.1. Elements used in this research and their corresponding starting materials.

Element	Starting material
Sr	$SrCO_3$
La	La_2O_3
Ti	TiO_2
Ga	Ga_2O_3
Al	Al_2O_3
In	In_2O_3
Co	Co_3O_4
Fe	Fe_2O_3
Mn	Mn_2O_3
Zr	ZrO_2

Table 4.2. List of compounds synthesized with the synthesis conditions.

Compound	Synthesis (*)
$Sr_3Ti_2O_7$	1400 °C/ 5 days
$Sr_3Ti_{1.8}Al_{0.2}O_{6.9}$	1400 °C/ 3 days
$Sr_3Ti_{1.75}Al_{0.25}O_{6.875}$	1400 °C/ 5 days
$Sr_{2.9}La_{0.1}Ti_{1.8}Al_{0.2}O_{6.95}$	1400 °C/ 4 days
$Sr_3Ti_{1.8}Ga_{0.2}O_{6.9}$	1400 °C/ 3 days
$Sr_3Ti_{1.75}Ga_{0.25}O_{6.875}$	1400 °C/ 6 days [a]
$Sr_3Ti_{1.9}In_{0.1}O_{6.95}$	1400 °C/ 5 days [a]
$Sr_3Zr_2O_7$	1550 °C/ 1 day [a]
$Sr_3Zr_{1.9}Al_{0.1}O_{6.95}$	1550 °C/ 1 day [a]
$Sr_3Zr_{1.9}Ga_{0.1}O_{6.95}$	1550 °C/ 1 day [a]
$Sr_3Ti_{1.8}Co_{0.2}O_7$	1400 °C/ 3 days
$Sr_3Ti_{1.6}Co_{0.4}O_7$	1400 °C/ 3 days + 1350 °C/ 1 day
$Sr_3Ti_{1.4}Co_{0.6}O_7$	1250 °C/ 4 days
$Sr_3Ti_{1.2}Co_{0.8}O_7$	1250 °C/ 3 days
Sr_3TiCoO_7	1250 °C/ 7 days
$Sr_3Ti_{1.5}Fe_{0.5}O_7$	1300 °C/ 3 days +1350 °C/ 3 days
Sr_3TiFeO_7	1250 °C/ 3 days[b]
$Sr_3Ti_{0.5}Fe_{1.5}O_7$	1250 °C/ 3 days
$Sr_3Fe_2O_7$	1150 °C/ 2 days[b]
$Sr_3Ti_{1.5}Mn_{0.5}O_7$	1400 °C/ 3 days +1450 °C/ 2 days
Sr_3TiMnO_7	1400 °C/ 3 days +1450 °C/ 2 days
$Sr_3Ti_{0.5}Mn_{1.5}O_7$	1400 °C/ 3 days +1500 °C/ 2 days
$Sr_3Mn_2O_7$	1595 °C/ 12 hrs

* All compounds were first reacted at 900 °C for 24 hours except were noted

[a] No first heating at 900 °C

[b] First heating at 1000 °C for 24 hours

4.2. Structural characterization

All samples were structurally characterized by X-ray powder diffraction (XRD). These measurements were carried out on two different diffractometers. The first was a Siemens D5000 diffractometer with Cu Kα radiation, $\lambda(K\alpha_1)$= 1.54056 Å, which operated at 40 kV and 45 mA, with a graphite monochromator. The slits used were DS 1mm, SS 1mm and RS 0.6mm. Step scans (1 hour long) were taken from 5 to 65° (2θ), with step sizes of 0.05° and 3 sec/step. Samples were prepared by grinding the material to a fine powder, suspending it in a Collodion/amyl acetate (1:3 ratio) binder, and depositing the mixture on a glass slide. The glass slide was baked in an oven (*ca.* 100 °C) for a few minutes and mounted on a plastic sample holder with clay. This method produced thin, homogeneous samples.

The second diffractometer was a Rigaku RU300 with a rotating anode, also with Cu Kα radiation and a graphite monochromator, which was typically operated at 50 kV and 300 mA. Slits used in this case were DS 1.0°, SS 1.0° and RS 0.15°. Besides using the Collodion suspension method to run scans, the ground sample was sometimes placed on a piece of double-sided tape, which was then mounted on a glass slide. We also performed X-ray diffraction scans on sintered pellets, by placing the pellet on a custom-made stainless steel holder. Continuous scans from 5 to 65° were also performed usually with 10°/min.

Measurements carried out on the Siemens diffractometer were used to calculate lattice parameters. Prior to the use of the Rigaku diffractometer, all materials reported in this thesis had been structurally characterized, so diffraction patterns were used only to determine phase purity.

Lattice parameters were determined using the computer software PPLP in the NRCVAX package.[6]

4.3. Characterization of nonstoichiometry

The oxidation states of the transition metals (Co, Fe and Mn) may be determined by

iodometric titration. This method has been used before to characterize solid state materials.[7-11]

The laboratory procedures and theory for the method of iodometric titration, in general, can be

reviewed in any analytical chemistry book. See, for example, Skoog, West and Holler.[12] For the

procedure, a starch solution was prepared, and an approximately 0.01N $Na_2S_2O_3$ solution was

prepared and standardized.

An approximately 0.2% starch solution served as an indicator and was prepared as

follows: about 2 g of starch, 0.01g of HgI_2 and 30 ml of H_2O was thoroughly mixed in a mortar,

then added to about 1 L of boiling water and placed in a polypropylene bottle.

An approximately 0.01 N $Na_2S_2O_3$ solution was prepared as follows: 100 ml of

standardized 0.100 N $Na_2S_2O_3 \cdot 5$ H_2O (Alfa/Aesar) was added to approximately 900 ml H_2O. The

solution was standardized by producing a known amount of iodine (I_2) and titrating with

thiosulfate solution. The reaction of interest is

$$IO_3^- + 5I^- + 6H^+ \rightarrow 3I_2 + 3H_2O \tag{4.1}$$
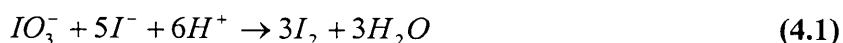
For the procedure, KIO_3 was dried in an oven for about 2 hours. About 0.015 g of KIO_3 was

weighed by difference in an Erlenmeyer flask and dissolved in 5 ml of distilled water. About

0.28 g (excess) KI was added to the solution, followed by 3 ml 6 M HCl, upon which the solution

turned brown due to the production of iodine (I_2). The iodine was then titrated using the

standardized thiosulfate solution according to the following reaction:

$$I_2 + 2S_2O_3^{2-} \rightarrow 2I^- + S_4O_6^{2-} \tag{4.2}$$

Starch was added just before the endpoint was reached, and made the solution turn blue. The endpoint was taken as the point at which the blue color disappeared. At least three consistent measurements were carried out. The concentration of the thiosulfate solution was calculated through the use of equations 4.1 and 4.2. The average concentration from the three measurements was then taken as the concentration of the thiosulfate solution. 95% confidence limits were also calculated.

One full set of data of nonstoichiometry vs. oxygen partial pressure was collected on a sample with nominal composition $Sr_3Ti_{1.2}Co_{0.8}O_{7-\delta}$. I chose this composition because it was the Co-doped material with the highest concentration of Co for which I had conductivity data as a function of oxygen partial pressure. This allowed correlations to be drawn between composition, nonstoichiometry and conductivity trends. Also, after preliminary test measurements, it was apparent that Co^{4+} was present. For this reason, we took the composition with the highest concentration of Co.

Ground samples of $Sr_3Ti_{1.2}Co_{0.8}O_{7-\delta}$ were placed in an alumina boat which was placed inside a closed-end mullite tube. The tube was introduced in a tube furnace which could be rolled back and forth (towards and away from the sample), so that the ceramic tube could be removed from the furnace and exposed to ambient temperature very quickly. The open end of the tube was fitted with a Cajon-type fitting so that a desired gas mixture could be flowed through it. Gases used for the quenching experiments were: air, 1% O_2/Ar, 100ppm O_2/Ar and 0.1% CO/CO_2. Samples were left at 700 °C overnight and then quenched as described above. This procedure had been previously used successfully in the Tuller group to quench samples.
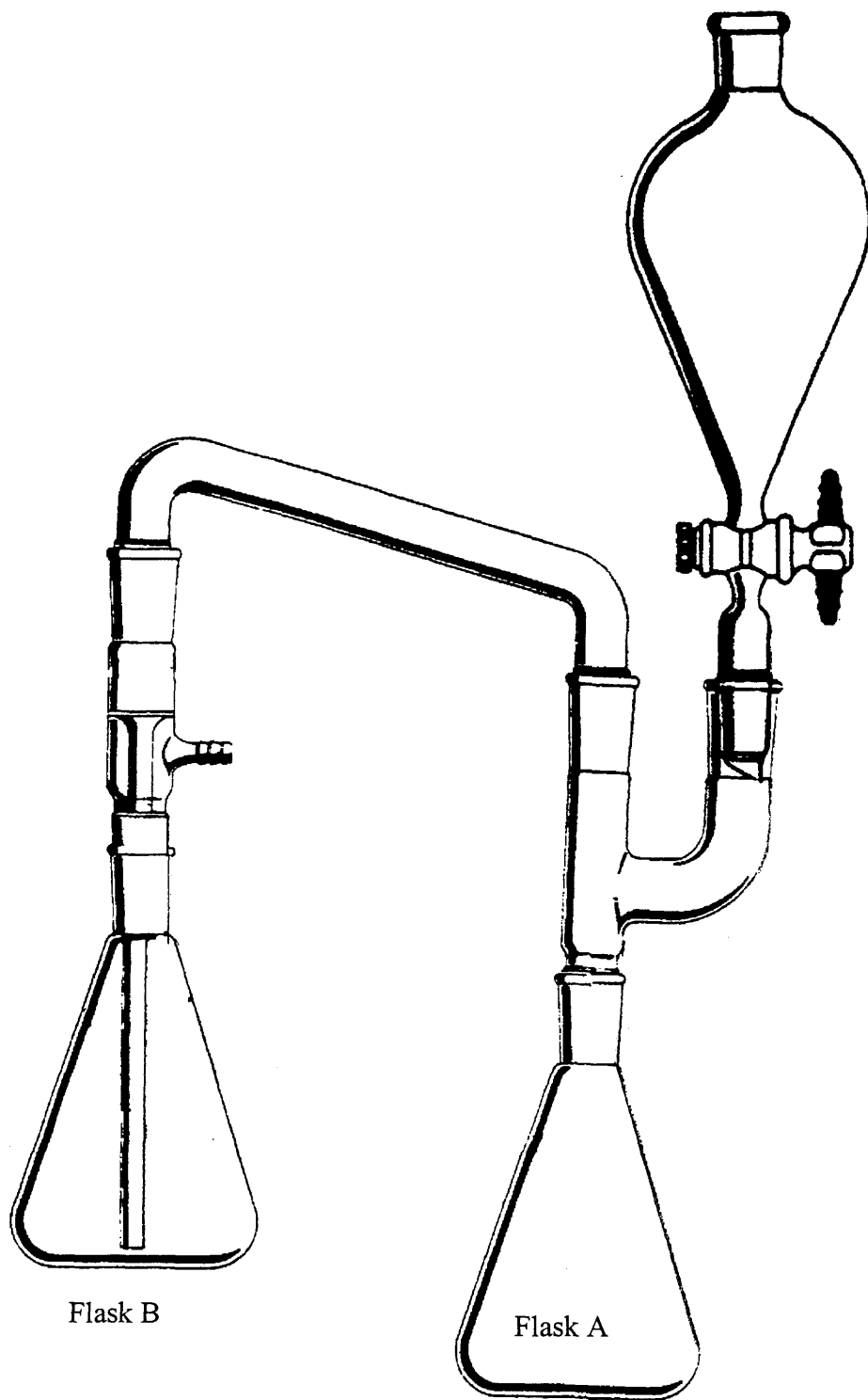
Flask B

Flask A

Figure 4.1. Experimental setup for iodometric titration

An apparatus such as the one depicted in Figure 4.1 was assembled. The quenched

sample to be studied (about 100 mg) and an excess of KI (about 1 g) were placed in flask A.

Excess KI was placed in flask B, where it was dissolved in 10 ml of distilled H_2O and 10 ml of

concentrated HCl, while $N_2(g)$ was passed through the solution. Concentrated HCl (about 20 ml)

was added to the sample to be studied (e.g. Sr_3TiCoO_y) through the separatory funnel. In order

for the reaction to occur, this mixture was stirred and gently heated while $N_2(g)$ was passed

through. When the sample was completely reacted, flask A was removed from the apparatus and

titrated with standardized $Na_2S_2O_3$ solution (about 0.01N), adding starch near the endpoint. Flask

B was also titrated using the same procedure.

The relevant chemical equations are:

$$Co^{2+p} + pe^- \rightarrow Co^{2+} \tag{4.3}$$

$$2Cl^- \rightarrow Cl_2 + 2e^- \tag{4.4}$$

After multiplying equation 4.3 by 2 and equation 4.4 by p and adding them, we get:

$$2Co^{2+p} + 2pCl^- \rightarrow 2Co^{2+} + pCl_2 \tag{4.5}$$
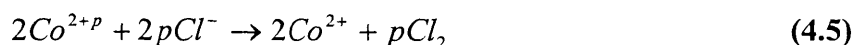
Then chlorine reacts with iodide in the following manner

$$pCl_2 + 2pI^- \rightarrow pI_2 + 2pCl^- \tag{4.6}$$

and iodine is titrated by thiosulfate

$$pI_2 + 2pS_2O_3^{2-} \rightarrow 2pI^- + pS_4O_6^{2-} \tag{4.7}$$
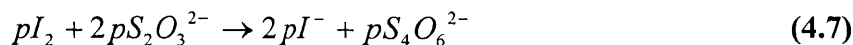
Adding equations 4.3, 4.4, 4.5, 4.6 and 4.7 we finally obtain

$$2Co^{2+p} + 2pS_2O_3^{2-} \rightarrow 2Co^{2+} + pS_4O_6^{2-} \tag{4.8}$$
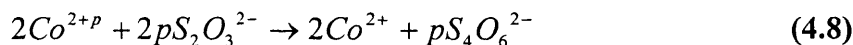
So, for every mole of Co^{2+p}, p moles of $S_2O_3^{2-}$ will be used. Hence:

$$\#moles\ Co = \frac{\#moles\ S_2O_3^{2-}\ used}{p} \qquad (4.9)$$

On the other hand, the exact molecular weight of the material under study is unknown,

and depends directly on the oxidation state of the cation (in our case Co) or, equivalently, on the

oxygen stoichiometry. In our case, if we assume that all Co is +2, then the molecular weight of

the comopund is 465.6566 g/mol. For Co^{2+p}, the molecular weight is then

$$M.W. = 465.6566 + \left(\frac{p}{2}\right) \times 15.9994\ \ g/mol \qquad (4.10)$$

and the number of moles of Co (in $Sr_3Ti_{2-x}Co_xO_y$) used in the titration experiment is

$$\#moles\ Co = \frac{x \times (\#g)}{M.W.} \qquad (4.11)$$

The right hand sides of equations (4.9) and (4.11) can now be equated and solved for p, obtaining

$$p = \frac{(M.W.) \times (\#moles S_2O_3^{2-})}{x*(\#g) - (7.9997*(\#moles S_2O_3^{2-}))} \qquad (4.12)$$

In order to determine the validity of the method, it was successfully standardized by using

$KMnO_4$ as the starting material. After 3 consistent titrations, an average oxidation state of Mn of

7.03 was obtained. One should bear in mind that the accuracy of these experiments depends on

the amount of sample used. Since in the case of $KMnO_4$ we used quantities on the order of

15 mg, and in the case of the Ruddlesden-Popper phases we used more (about 100 mg), the

accuracy of the measurements on our materials was expected to be considerably improved.

4.4 Electrical conductivity characterization

The electrical conductivity was measured using AC impedance spectroscopy. A brief overview of this technique is provided in the following section, followed by a description of the experimental setup.

4.4.1. AC impedance spectroscopy

Conductivity is typically determined by measuring the resistance of a sample under a potential gradient. However, the response changes depending on whether the resistance is ionic or electronic in nature due to the internal changes that take place in a material. Figure 4.2 illustrates the behavior over time of an electronic, ionic and mixed conductor under a potential gradient. In the case of an electronic conductor, the current or resistance stays constant over time, since it is simply given by Ohm's Law. In an ionic conductor, the ionic mobile species internally rearrange to counter the external potential applied. Therefore, under such a potential, O^{2-} and $V_o^{..}$ will move towards the positive and negative electrodes, respectively. The consequence of this motion is an internal polarization that the material experiences from the motion of opposite charges to opposite electrodes. Due to this polarization, the current (motion of charged particles) will drop off with time, assuming that the electrodes are blocking the ionic current. In the case of a mixed conductor, the current will theoretically decrease down to a value given by the magnitude of the electronic conduction. In principle, it should be possible to determine the magnitude of the electronic conduction in a mixed ionic/electronic conductor using this method. In practice, this approach is problematic due to the internal segregation of ions, among other factors.[13]

Consequently, 2-probe DC measurements of the type described are not used to measure ionic conductivity in solids. Instead, AC impedance spectroscopy is the method of choice for this purpose. A detailed description of impedance spectroscopy is provided by Macdonald,[14] and a brief explanation is provided below.

Impedance is the alternating current analogue to resistance for direct current. Thus, in a DC measurement, the resistance is given by

$$R = \frac{V}{I} \tag{4.13}$$

The impedance is calculated in a similar manner. The technique is based on applying a small signal, $v(t)$, to a sample. The signal follows a sinusoidal relation

$$v(t) = V_m \sin(\omega t) \tag{4.14}$$

where V_m is the voltage amplitude, and ω is the frequency in Hertz. The resulting steady-state current of the system is measured as a function of the signal over a range of frequencies

$$i(t) = I_m \sin(\omega t + \phi) \tag{4.15}$$

where ϕ represents the phase shift. The impedance is then defined as:

$$Z(\omega) = \frac{v(t)}{i(t)} \tag{4.16}$$

and may be rewritten in terms of its real and imaginary parts

$$Z = Z' + iZ'' \tag{4.17}$$

By plotting the imaginary vs. the real components in the complex plane as a function of frequency, important information regarding the resistance and capacitance of the sample and the origin of the various contributions to that resistance may be gathered. To understand how this

Figure 4.2. Variation of current with respect to time in the cases of an electronic, ionic and mixed ionic/electronic conductor, respectively
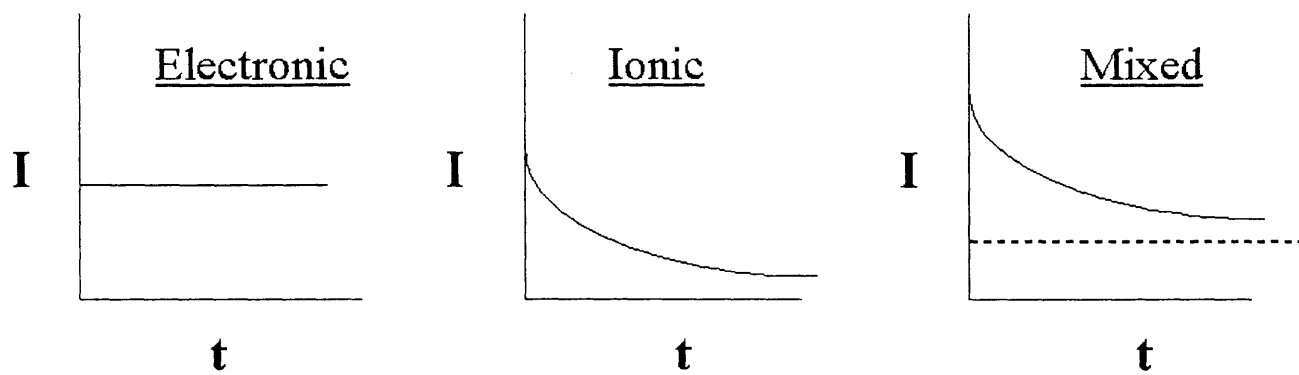
may be done, it is useful to realize how the different components in a material will contribute to the resistance in an AC experiment.

Both a resistance and a capacitance are associated with the conduction process. Therefore, the bulk of the material may be represented by an RC-circuit. In a polycrystalline material, however, charges must move between the internal grains of the material often overcoming space charge barriers. This conduction process at the grain boundaries can also be represented by its own RC-circuit. Furthermore, the charge transfer occurring at the electrodes can also be regarded in a similar manner. These parallel RC-circuit components are usually looked at as a series circuit (see Figure 4.3), with each component giving rise to its own impedance. The product of R and C is termed the time constant, and for simplicity we will assume that the time constants of all components are distinct. Then the impedance of each RC-circuit component is given by

$$ Z = \frac{1}{\frac{1}{R} + j(2\pi f C)} \tag{4.18} $$

where R is the resistance in ohms, $j = \sqrt{-1}$, f is the frequency in Hz and C is the capacitance in Farads. Multiplying equation 4.18 by the complex conjugate of its denominator, the real and imaginary parts can be separated as follows:

$$ Z' = \frac{\frac{1}{R}}{\left(\frac{1}{R}\right)^2 + (2\pi f C)^2} \tag{4.19} $$

$$ Z'' = \frac{2\pi f C}{\left(\frac{1}{R}\right)^2 + (2\pi f C)^2} \tag{4.20} $$

From here one arrives at an equation for a circle with a center at $\left(\frac{R}{2}, 0\right)$ and radius $\frac{R}{2}$:

$$(Z'')^2 + (Z' - \frac{R}{2})^2 = \frac{R^2}{4} \qquad\qquad (4.21)$$

If the time constants associated with each process are indeed different enough, three contacting arcs are formed in a plot of Z" vs. Z'. In actual experiments, this is rarely the case. Figure 4.4. illustrates this point. The figure shows how the arcs corresponding to the bulk and grain boundary combine to form a single depressed arc. Experimentally it becomes hard to tell whether the arc corresponds to bulk or grain boundary conduction, and therefore it is common to report the total conductivity of the material as the sum of both contributions. In the course of this research thesis, this was a common situation, and so the conductivity values reported in later chapters are derived from the sum of contributions from the bulk and grain boundary resistivities.

We should note that, although in our studies we have not been able to differentiate between bulk and grain boundary conductivities, it may be of interest in certain instances to pursue further the separation of these individual contributions. While bulk conductivities are an intrinsic property of any given material, the grain boundary represents a parameter which may be modified by appropriate control on the microstructure of the material.

It is clear from the above discussion that AC impedance spectroscopy is a powerful technique which offers an advantage over DC measurements in that it may characterize bulk and interfacial conductivities and identify the origin of the contributions to the total conductivity.

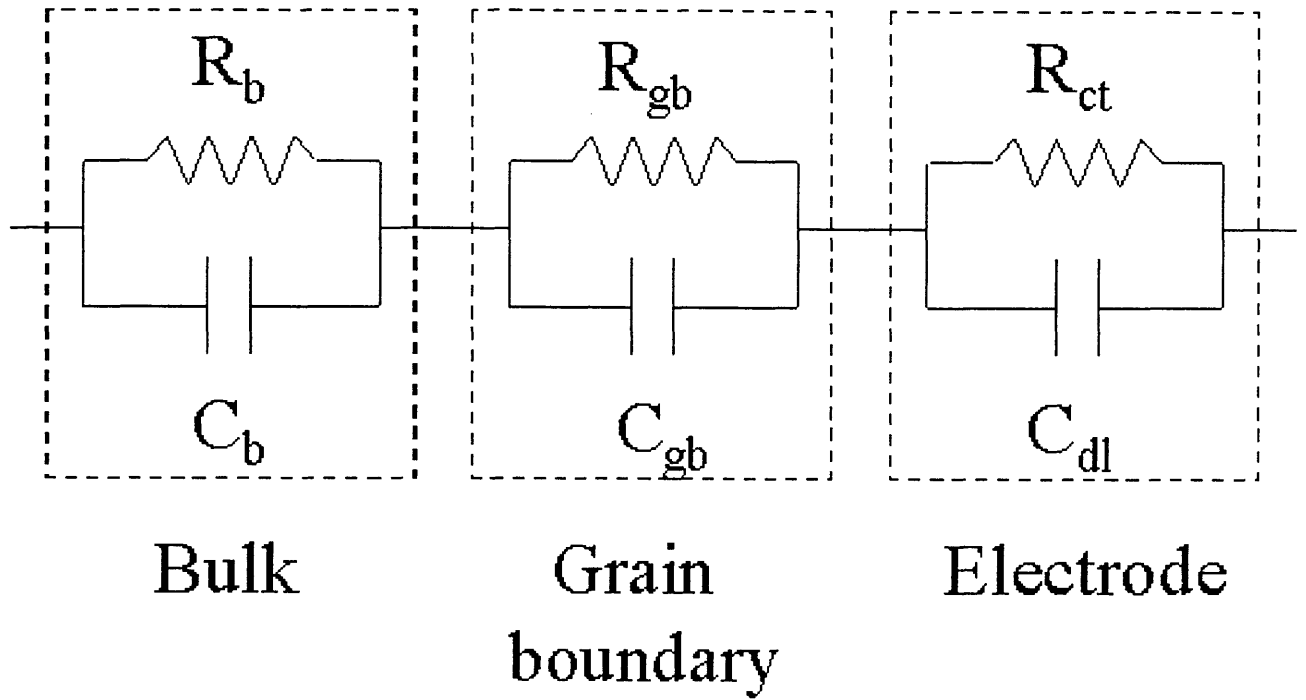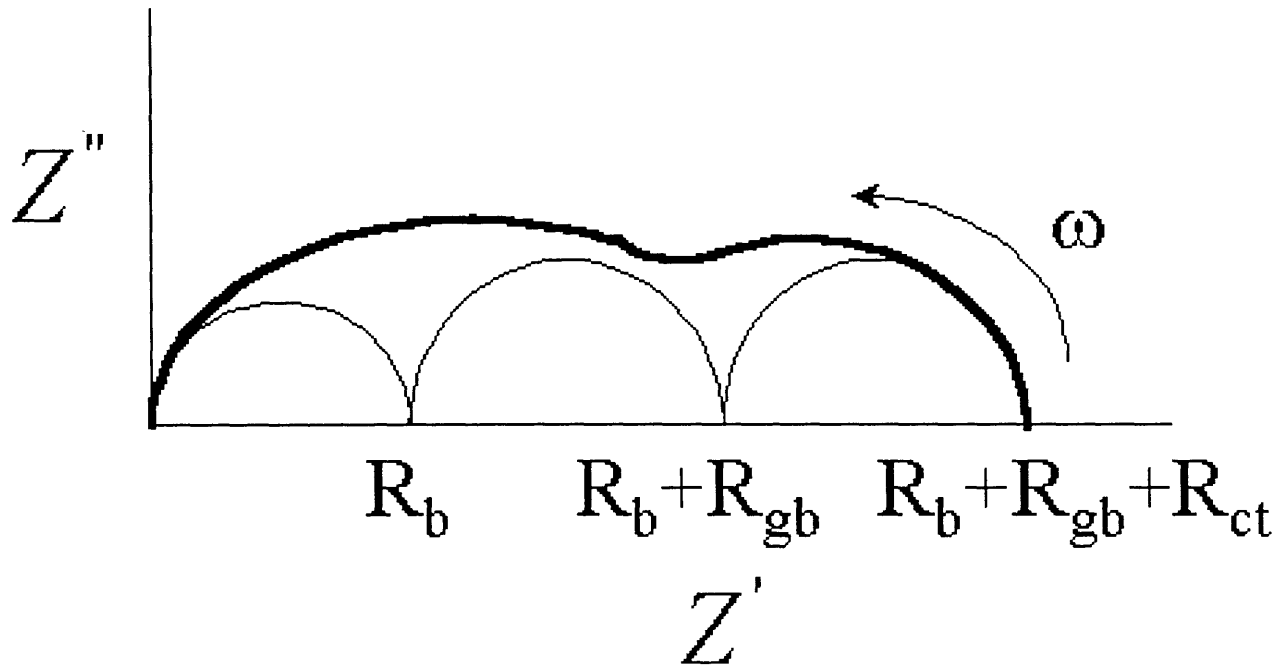**Figure 4.3. RC circuits for bulk, grain boundary and electrode processes in an ionic conductor**

Bulk   Grain   Electrode
              boundary

Figure 4.4. Impedance plot for the circuit in the previous figure

4.4.2. Conductivity measurements

The electrical conductivity was measured using AC impedance spectroscopy on sintered pellets. The powders were pressed into ½" pellets and heated at a temperature 50 °C higher than the previous heating cycle for sintering. Pellet densities ranged from 70-80% (Al and Ga doping) to about 90% of theoretical densities. Measurements of conductivity as a function of temperature in air were carried out for most fixed-valent doped samples, as well as for $Sr_3Ti_{1.8}Co_{0.2}O_{7-\delta}$. Measurements of conductivity as a function of oxygen partial pressure were performed for all transition metal-doped samples at temperatures ranging between 600 and 1000 °C, as well as for a number of Al and Ga-doped compositions. Except were noted, these measurements were taken at 700 °C. For some Co-doped samples, the temperature dependence of the conductivity was measured under Ar and other CO/CO_2 mixtures in order to obtain values for the activation energy under those atmospheric conditions. After $p(O_2)$-dependence measurements were carried out, one of the faces of the pellet was polished with sand paper, while the other was kept intact, and XRD powder patterns of both sides were collected to check for possible decomposition of the samples.

The setup used for conductivity measurements is shown in Figure 4.5. The outside tube is made of nickel and is grounded to eliminate noise. Inside the nickel tube was a ¾" mullite single-bore tube with Cajon Ultra-torr connectors at each end. Inside this tube were two ½" double-bore mullite tubes. A three-way Ultra-torr fitting was placed at the end of the double-bore mullite tube to enable a controlled atmosphere. Platinum wire leads were inserted through one of the holes, and on one side a thermocouple was also inserted. The end of the thermocouple was positioned approximately 2-3 mm from the sample. Pt foil was used as the electrodes and was attached to the platinum leads. The thermocouple and platinum leads were run through a piece of rubber cord stock with the aid of a hypodermic needle to ensure good sealing. The sample was placed

between the two double-bore tubes. Good contact was ensured by pressing the two tubes against each other with the aid of springs.

In the Tuller group, the basic setup remained very similar with a few changes. There was no outside nickel tube present, and the outer ¾" mullite tube was made of quartz. The atmosphere was controlled in a similar manner although, instead of rubber cord stock tubing, the sealing was obtained with the aid of a high-temperature silicon rubber adhesive sealant, Red RTV 106, made by GE Silicones®. This sealing method also proved effective.

Most of the measurements reported herein were carried out while in the zur Loye laboratories. In the Tuller laboratories, measurements of conductivity as a function of oxygen partial pressure for $Sr_3Ti_{1.98}Ga_{0.02}O_{6.99}$, $Sr_3Ti_{1.95}Ga_{0.05}O_{6.95}$ and additional measurements for $Sr_3Ti_{1.8}Co_{0.2}O_{7-\delta}$ at several temperatures were taken.

In order to achieve an appropriate range of oxygen partial pressures, O_2/Ar and CO/CO_2 mixtures were used. The concentration of O_2 in Ar directly gives the desired partial pressure down to about 100 ppm (10^{-4} atm). The lower oxygen partial pressures in CO/CO_2 mixtures are given by the equation for the Gibbs free energy

$$\Delta G^{\circ} = 86.81T - 282400 J \tag{4.22}$$

for the reaction

$$CO + \frac{1}{2}O_2 \leftrightarrow CO_2$$
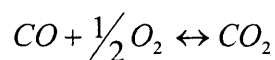
This provides a range of partial pressures of about 10^{-5}-10^{-30} atm of oxygen at temperatures between 600 and 1000 °C (the range of oxygen pressures changing with each temperature). Measurements of conductivity as a function of p(O_2) were always performed going from high to

Figure 4.5. Experimental setup for 2-probe AC impedance measurements

low p(O_2) in order to start from the more stable end of oxygen partial pressures. The oxygen

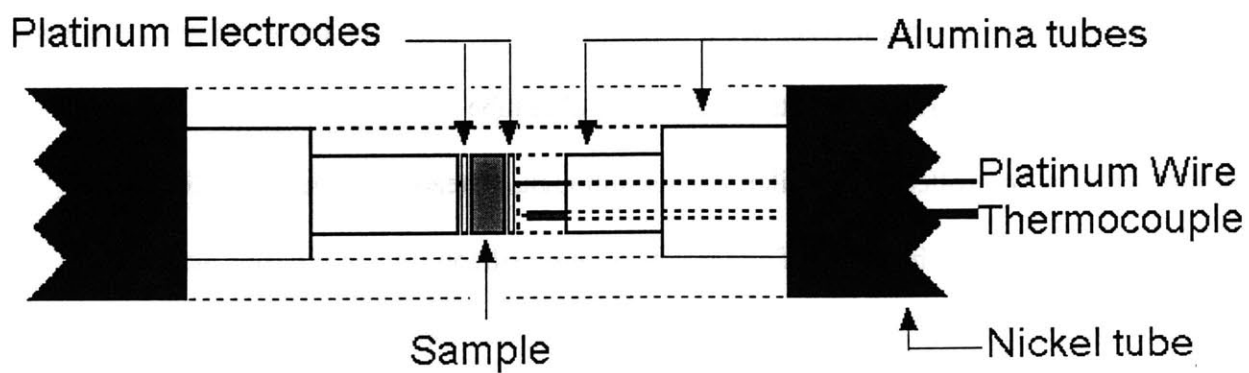partial pressure in the gas stream was measured after passing it over the sample using a

YSZ-based oxygen sensor working at 750 °C. After changing the gas mixtures, the sample was

allowed to equilibrate before moving on to the next measurement. Waiting times varied greatly

with temperature, and ranged from under an hour (1000 °C) to several hours (600 °C).

The AC impedance spectroscopy measurements were taken using a Solartron 1260

impedance/gain-phase analyzer interfaced to a PC driven by Z-Plot software (Scribner

Associates). The frequency range was typically 1 MHz to 1 Hz and measurements were taken in

log form; the amplitude of the potential was typically 10 mV. No bias was applied.

Using Z-View software (a complementary software package with Z-Plot), the impedance

plots thus obtained were analyzed. Because such plots typically displayed only parts of one or

two arcs at most, it was very difficult to assign the arcs to the appropriate conduction process (i.e.

bulk, grain boundary, etc.) The arc corresponding to the higher frequencies was fitted, and its

intercept with the real axis taken as the value of the total resistance of the sample (i.e. bulk plus

grain boundary). For a pellet-shaped sample, the conductivity was calculated via the following

relation:

$$\sigma = \frac{l}{A \cdot R} \tag{4.23}$$

where l and A represent the thickness (in cm) and cross-sectional area (in cm^2), respectively, and

R is the resistance in ohms.

4.4.3. EMF measurements

4.4.3.1 Background

Measurements of the electromotive force (EMF) are used to determine the transference number of an ionic/mixed conductor under certain conditions of temperature and oxygen partial pressure. They are carried out by using a setup similar to the oxygen sensor (see Chapter 2). One keeps a reference $p(O_2)^I$ on one side, varies $p(O_2)^{II}$ on the other side and measures the voltage across the sample. If the conductivity is purely ionic ($t_i \approx 1$), then the measured voltage should correspond to the Nernst voltage. Since electronic conductivity will partially short circuit the sensor, the ratio between the measured (V_M) and the theoretical (V_T) represents an average t_i.

$$t_i = \frac{V_M}{V_T} \tag{4.24}$$

The voltage may also be expressed in terms of the transference number via the following relation[15]

$$E = \frac{kT}{4q} \int_{II}^{I} t_i d \ln p(O_2) \tag{4.25}$$

If $p(O_2)^I$ is fixed on one side of the oxide sample to serve as reference and $p(O_2)^{II}$ is varied, t_i can be obtained by differentiating equation 4.25 with respect to the reference $p(O_2)^I$, and is given by

$$t_i(p(O_2)) = \frac{4q}{kT} \left(\frac{\partial E}{\partial \ln p(O_2)} \right)_{p(O_2)=p(O_2)^{II}} \tag{4.26}$$

Therefore, t_i may be calculated at a certain $p(O_2)^{II}$ by evaluating the slope of the E vs. ln $p(O_2)$ at constant $p(O_2)^I$.

4.4.3.2 EMF Experimental setup

The experimental setup for the EMF measurements is shown in Figure 4.6. It consists of an outer ¾" quartz tube with a ½"-long glass support in the center. This support has a 9 mm hole running through it. On one side of the support, the seal material is introduced, followed by a ½" sample pellet. They are both pressed against the glass support by a ½" alumina tube; through the tube runs the Pt lead, which is in contact with Pt gauze, which in turn is in contact with the sample itself. The other Pt electrode also consists of Pt gauze in contact with wire that runs through a ¼" alumina tube. Both alumina tubes are spring-loaded to ensure adequate sealing. Both sides of the sample have a gas inlet and outlet to allow the gas to flow in and out of the same side. One gas was kept constant (typically 10%CO/CO$_2$), while the other was changed from 10%CO/CO$_2$ to higher p(O$_2$)'s.

The sample was prepared in a similar manner to that used for the conductivity measurements. Pt paint was applied to both faces of the sintered pellet and fired at 900 °C for 2 hours. Only Co-doped samples were studied, specifically Sr$_3$Ti$_{1.8}$Co$_{0.2}$O$_{7-\delta}$ and Sr$_3$Ti$_{1.6}$Co$_{0.4}$O$_{7-\delta}$. The first sample presented a problem in that it was only 73% dense and, consequently, a sample of the latter composition was used. This sample was very close to 100% dense.

The sealing material presented a number of problems. We first attempted to use Pyrex rings of appropriate size to seal the sample. While, at first, we thought that this setup did not provide a good enough seal, it was later determined that the Pyrex ring reacted with the sample. XRD patterns of the pellet face reveal partial decomposition of the sample and new minor compounds formed at the surface which contained Si from the Pyrex. We then tried the use of metals, which proved more successful. Gold foil was shown not to react with the sample; using a

Figure 4.6. Experimental setup for EMF measurements
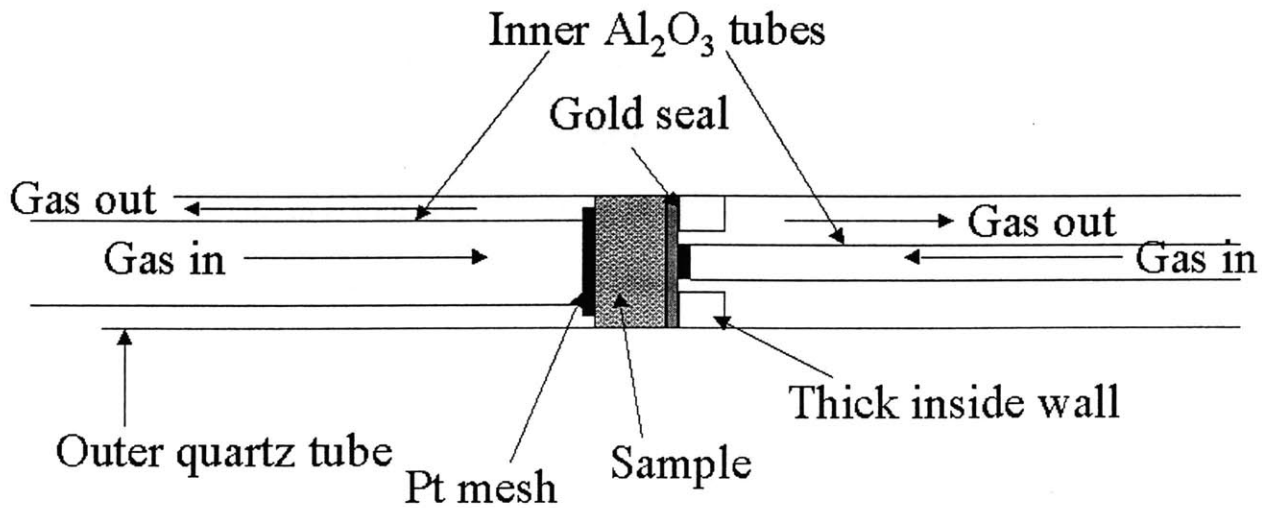
large enough piece of gold foil and heating the setup to about 700 °C or above afforded an

appropriate seal. Above this temperature, gold softens and may be used to prevent gas leakage

across the sample.

4.4.4 Chemical diffusion coefficient

4.4.4.1. Background

As was pointed out in Chapter 3, the ionic conductivity is directly related to the chemical

diffusion coefficient. After carefully choosing the appropriate conditions of temperature and

oxygen partial pressure, the overall chemical diffusion coefficient of the material may be directly

related to the diffusion of oxide ions. There are many different methods to independently

determine the chemical diffusion coefficient reported in the literature.[16]

The method of electrical conductivity relaxation has been successfully employed to

determine the chemical diffusion coefficient in Cu_2O[17], NiO[18], $YBa_2Cu_3O_{6+x}$.[19] and $LaCrO_3$,[20]

among others. An abrupt change of chemical potential is imposed on a sample under constant

temperature, usually changing the atmospheric conditions, $p(O_2)$, and the change with time of

physical properties such as resistance is monitored until the sample reaches equilibrium again.

The method was first proposed by Dünwald and Wagner in 1934.[21] It has been typically used by

assuming that the sample surface instantaneously attains equilibrium with the atmosphere, so that

the relaxation process which is being monitored is controlled exclusively by bulk diffusion.

Some studies have suggested that the importance of this surface effect should not be

overlooked,[20] although in practice, both effects can generally be clearly separated.

The relationship between the electrical conductivity and the chemical diffusion

coefficient may be given by equation 4.27:

$$\frac{\sigma - \sigma_\infty}{\sigma_0 - \sigma_\infty} = \frac{8}{\pi^2} \cdot e^{-\frac{\pi^2 \tilde{D} t}{a^2}} \tag{4.27}$$

where t is the time, $\tilde{D}$ is the chemical diffusion coefficient, a is the thickness of the sample and σ_∞ and σ_0 represent the conductivities at equilibrium and at time t = 0, respectively. Therefore, a plot of $\ln[(\sigma - \sigma_\infty)/(\sigma_0 - \sigma_\infty)]$ as a function of time yields the chemical diffusion coefficient, $\tilde{D}$.

4.4.4.2 Experimental setup for measurements of the chemical diffusion coefficient

The experimental setup used to obtain conductivity data at various temperatures and oxygen pressures depicted in Figure 4.5 was also employed to measure the chemical diffusion coefficient. A dense sample (near 100%) of composition $Sr_3Ti_{1.6}Co_{0.4}O_7$ was equilibrated (typically in air) at temperatures of 700, 750 and 800 °C, and then the gas atmosphere was changed to either 0.1% O_2/Ar or 100 ppm O_2/Ar. The change of resistance was monitored as a function of time, and equilibration times were about 2 hours (which varied slightly with temperature).

References

1. Ruddlesden, S. N. and Popper, P., *Acta Cryst.,* **1958**, *11,* 54-55.

2. Minichelli, D. and Longo, V., *J. Mater. Sci. Lett.,* **1978**, *13,* 2069-2070.

3. Mizutani, *J. Chem. Soc. (Japan) Ind. Ed.,* **1970**, *73,* 1097-1103.

4. Dann, S. E., Weller, M. T. and Currie, D. B., *J. Solid State Chem.,* **1992**, *97,* 179-185.

5. Dann, S. E. and Weller, M. T., *J. Solid State Chem.,* **1995**, *115,* 499-507.

6. Gabe, E. J., Page, Y. L., Charland, J. P., Lee, F. L. and White, P. S., *J. Appl. Cryst.,* **1989**, *22,* 384-387.

7. Ward, R. and Struthers, J. D., **1937**, *59,* 1849-1854.

8. Petrov, K., Markov, L., Ioncheva, R. and Rachev, P., *J. Mater. Sci.,* **1988**, *23,* 181-184.

9. Gushee, B. E., Katz, L. and Ward, R., **1957**, *79,* 5601-5603.

10. Guggilla, S. and Manthiram, A., *J. Electrochem. Soc.,* **1997**, *144,* L120-L122.

11. Sunstrom, J. E. I., Ramanujachary, K. V., Greenblatt, M. and Croft, M., *J. Solid State Chem.,* **1998**, *139,* 388-397.

12. Skoog, D. A., West, D. M. and Holler, F. J., in *Fundamentals of Analytical Chemistry,* D. A. Skoog, D. M. West and F. J. Holler, Eds. (Saunders College Publishing, 1992), pp. 863-864.

13. Giuntini, J. C., Zanchetta, J. V. and Salam, F., *Mater. Sci. Eng. B-Solid State Mat.,* **1995**, *33,* 75.

14. Macdonald, J. R. *Impedance Spectroscopy*; John Wiley & Sons: New York, 1987.

15. Tuller, H. L., in *Nonstoichiometric Oxides,* O. T. Sorensen, ed. (Academic Press, Inc., New York, 1981), pp. 271-332.

16. Riess, I., in *The CRC Handbook of Solid State Electrochemistry,* P. J. Gellings and H. J. M. Bouwmeester, Eds. (CRC Press, Boca Raton, 1997), pp. 223-268.

17. Maluenda, J., Farhi, R. and Petot-Ervas, G., *J. Phys. Chem. Solids,* **1981**, *42*, 697-699.

18. Farhi, R. and Petot-Ervas, G., *J. Phys. Chem. Solids,* **1978**, *39*, 1169-1173.

19. LaGraff, J. R. and Payne, D. A., *Phys. Rev. B,* **1993**, *47*, 3380-3390.

20. Yasuda, I. and Hikita, T., *J. Electrochem. Soc.,* **1994**, *141*, 1268-1273.

21. Dunwald, H. and Wagner, C., *Z. Phys. Chem.,* **1934**, *B24*, 53-58.

Chapter 5. Results

5.1. Synthesis

The synthesis of most of the doped Ruddlesden-Popper phases based on $Sr_3Ti_2O_7$ could be carried out at temperatures around 1400 °C. Only the more heavily doped Co-containing and Fe-containing materials needed a lower synthesis temperature. In general, this is due to a decrease of the melting point with increasing concentration of transition metals, as was observed a number of times experimentally. The Mn-doped material is an exception to this rule; $Sr_3Mn_2O_7$ was synthesized at high temperatures (1600 °C), and the solid solutions $Sr_3Ti_{2-x}Mn_xO_7$ also required high synthetic temperatures. Similarly, the few $Sr_3Zr_2O_7$-related materials required synthesis temperatures around 1550 °C. In general, we were guided by the synthesis temperatures and techniques reported in the literature.[1-4]

It should be noted that the fixed valent-doped titanates and zirconates were all brown in color. All samples turned darker after the sintering process. In contrast, the transition metal-doped phases were black, except perhaps for the lowest Co concentration used, for which the material was a very dark brown, almost black.

An observation of interest is the increased softness that the Co-doped materials exhibited. This had a detrimental effect on our ability to carry out conductivity measurements. Consequently, the synthesis of $Sr_3TiCoO_{7-\delta}$ is reported, whereas its electrical conductivity is not, because the compound showed an annoying propensity to crumble. Once this problem became apparent, we decided not to attempt synthesis of compounds containing higher concentrations of

cobalt, because of our inability to fully characterize the electrical properties of the sample.

Hence, x=1 is the highest doping level in the $Sr_3Ti_{2-x}Co_xO_{7-\delta}$ family.

Regarding the new materials formed by doping with fixed-valent cations, we were able to

substitute for about 1/8 of the cationic sites. For example, the synthesis of $Sr_3Ti_{1.5}M_{0.5}O_{6.75}$

(M=Al, Ga) was attempted, but secondary phases $(Sr_3M_2O_6)$ appeared in the XRD pattern. In the

case of doping with In, it was even harder to introduce higher concentrations into the structure,

presumably due to the large difference in cationic radii of Ti^{4+} and In^{3+}. Consequently, the

composition with the highest concentration was $Sr_3Ti_{1.9}In_{0.1}O_{6.95}$. In general, In-doped materials

were not further pursued due to the low levels of conductivities observed in the fixed

valent-doped materials.

5.2. Powder X-ray diffraction

XRD patterns showed that all samples reported herein were single phase. Some examples

of XRD patterns for $Sr_3Ti_{1.98}Ga_{0.02}O_{6.99}$, $Sr_3Ti_{1.6}Co_{0.4}O_{7-\delta}$ and $Sr_3TiFeO_{7-\delta}$ are shown in Figure

5.1, 5.2. and 5.3, respectively. On these powder patterns, the lines for the parent phase, $Sr_3Ti_2O_7$,

are typically shown as well for easy comparison with the parent phase. The peaks for the various

samples are always shifted towards a higher 2-theta value, corresponding to a decrease in

d-spacing and indicating a decrease in the cell parameter.

The powder patterns of appropriate quality were indexed using the PPLP package in the

NRCVAX software. Use of this program produced atomic cell parameters with, in general, low

errors. These are shown in Table 5.1 in parenthesis after the actual data. All phases were indexed

to a tetragonal cell, based on that corresponding to the parent structure, $Sr_3Ti_2O_7$.[5] Examples of

the assignment of Miller indices are provided in Tables 5.2, 5.3 and 5.4 which show the data for

$Sr_3Ti_{1.8}Al_{0.2}O_{6.9}$, $Sr_3TiCoO_{7-\delta}$ and $Sr_3TiFeO_{7-\delta}$, respectively.

In general, the indices assigned to the different 2-theta positions were based on those of

the parent phase. However, examining the tables one may conclude that some ambiguities arose

on some of these assignments. For example, if we compare the line at around $2\theta = 49°$, we

assigned the same set of Miller indices (e.g. h k l=1 1 8) for both $Sr_3Ti_{1.8}Al_{0.2}O_{6.9}$ and

$Sr_3TiFeO_{7-\delta}$, whereas one may observe a different set (e.g. h k l= 2 0 3) for $Sr_3TiCoO_{7-\delta}$. This is

due to the fact that both sets of indices correspond to very close values of 2-theta degrees, and the

assignment was given in order to provide a better refinement in the end. This was possible

because the PPLP software package provides a "goodness-of-fit" parameter that allowed us to

compare both options. In order to achieve the best set of results, we always attempted to

minimize this "goodness-of-fit" parameter.

Looking at the cell parameters, some trends become apparent. First, doping results in the

expected decrease in the cell parameters with respect to the parent phase, given that the ionic

radii of the dopants are, in general, smaller than those of Ti^{4+}(0.605 Å) and Zr^{4+} (0.72 Å). For

comparison, the ionic radii of the relevant cations are provided in Table 5.5. For example, for

Al^{3+} it is only 0.535 Å. The trend, however, is discontinued for Ga^{3+} (0.620 Å). In the case of the

In-doped sample, the cell parameters do increase as expected (e.g. $r(In^{3+})$= 0.80 Å). Substitution

of Ti^{4+} by transition metal cations also results in a decrease of the cell parameter. This

observation confirms the expectations, since cationic radii generally decrease as one goes across

the first-row transition metals for a given oxidation state. Second, an increase in dopant

concentration is accompanied by a decrease in cell parameters. For the most part, this occurs in

accordance with Vegard's Law, which states that the cell parameters should vary linearly with

119

solute concentration. The variations of cell parameters as a function of solute concentration for the various dopant cations are shown in Figures 5.4, 5.5, 5.6 and 5.7. These graphs show that the cell parameters do decrease with increasing dopant concentration, although not necessarily always in a linear fashion. Specifically, the cell parameters for $Sr_3Ti_{1.75}Ga_{0.25}O_{6.875}$ increase with respect to those for $Sr_3Ti_{1.8}Ga_{0.2}O_{6.9}$, a feature for which we have no explanation since XRD shows both materials to be single phase. Also, the c parameter in $Sr_3Mn_2O_7$ increases with respect to that of $Sr_3Ti_{0.5}Mn_{1.5}O_7$. While these discontinuities in the trends may be due to errors in the fitting of the peaks, the overall trend remains, in general, valid.

Since in the $Sr_3Ti_{2-x}Co_xO_{7-\delta}$ solid solution we were unable to synthesize compounds with x > 1, we fitted the data linearly in order to extrapolate the cell parameters for the Co end member, obtaining a= 3.823 Å and c= 20.02 Å.

In the Ruddlesden-Popper phases, the a parameter corresponds to the O-M-O distances which compose the MO_4 coordination sphere in the ab plane, and therefore is a direct indicator of interatomic bond distances. Consequently, dividing by 2 yields the average M-O bond distance. This is useful in determining possible trends in changing bond covalency and/or ionic radius as the concentration of dopant is being increased. Furthermore, information such as possible structural distortions may be gathered from these data. For instance, in the above case of the all-Co compound, the Co-O distance may be calculated as 1.9115 Å. For $Sr_3M_2O_7$ (M=Fe, Mn) the M-O distances are: 1.9275 Å (Fe-O) and 1.902 Å (Mn-O). These distances decrease in all cases from the parent phase, where the Ti-O distance is 1.9535 Å.
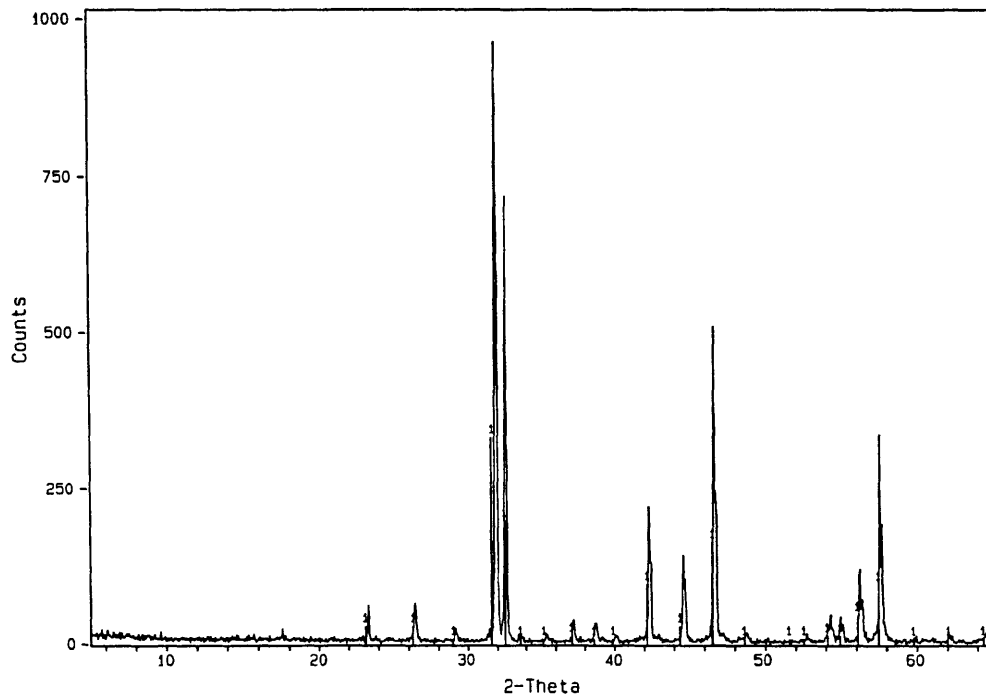
1> 11-0663: Sr3Ti2O7 - Strontium Titanium Oxide

cmse @ MIT - Mon Mar 16 1998 @9:34am

Figure 5.1. X-ray diffraction powder pattern for $Sr_3Ti_{1.8}Ga_{0.02}O_{6.99}$

C:\STUDENTS\CARLOS\XRAY\CNI192C.RAW CNI192C SR3TI1.6CO0.4 3HEAT (CT: 3.0s, SS:0.050dg, WL:
11-0663 Q Sr3Ti2O7 Strontium Titanium Oxide (WL: 1.5406Ao)
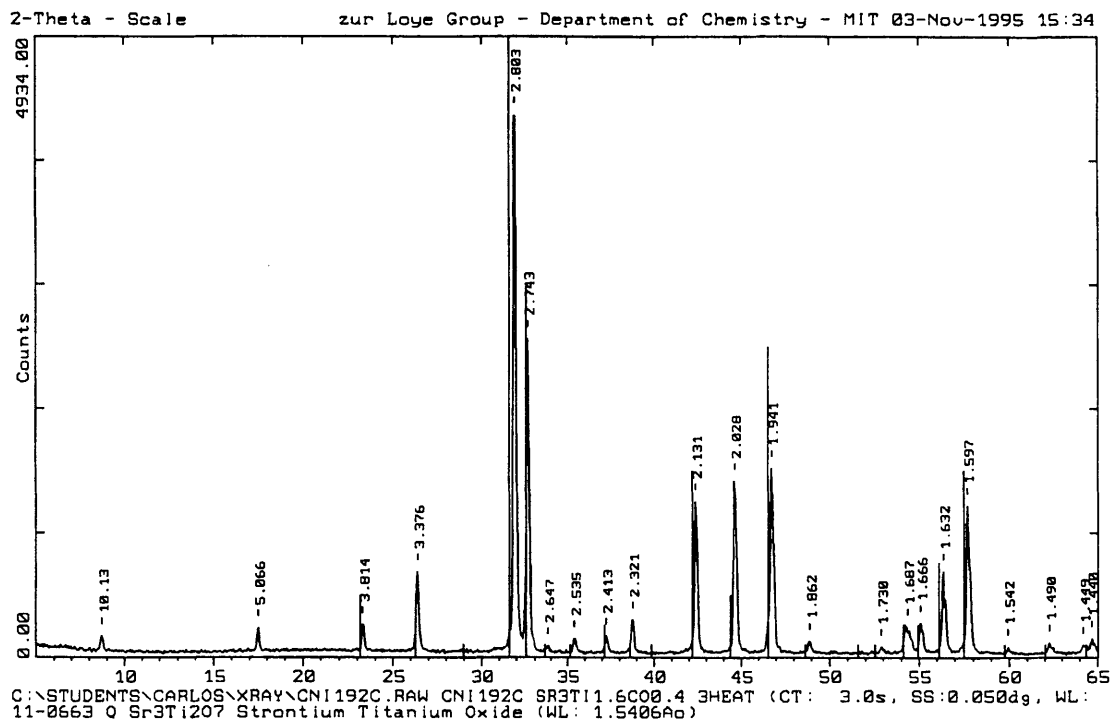
Figure 5.2. X-ray diffraction powder pattern for $Sr_3Ti_{1.6}Co_{0.4}O_{7-\delta}$

C:\STUDENTS\CARLOS\XRAY\CNII84C.RAW CNII84C SR3TIFEOY 3HEAT (CT: 3.0s, SS:0.050dg, WL: 1.54
26-0981 I Sr3Fe2O6.16 -Strontium Iron Oxide (WL: 1.5406Ao)
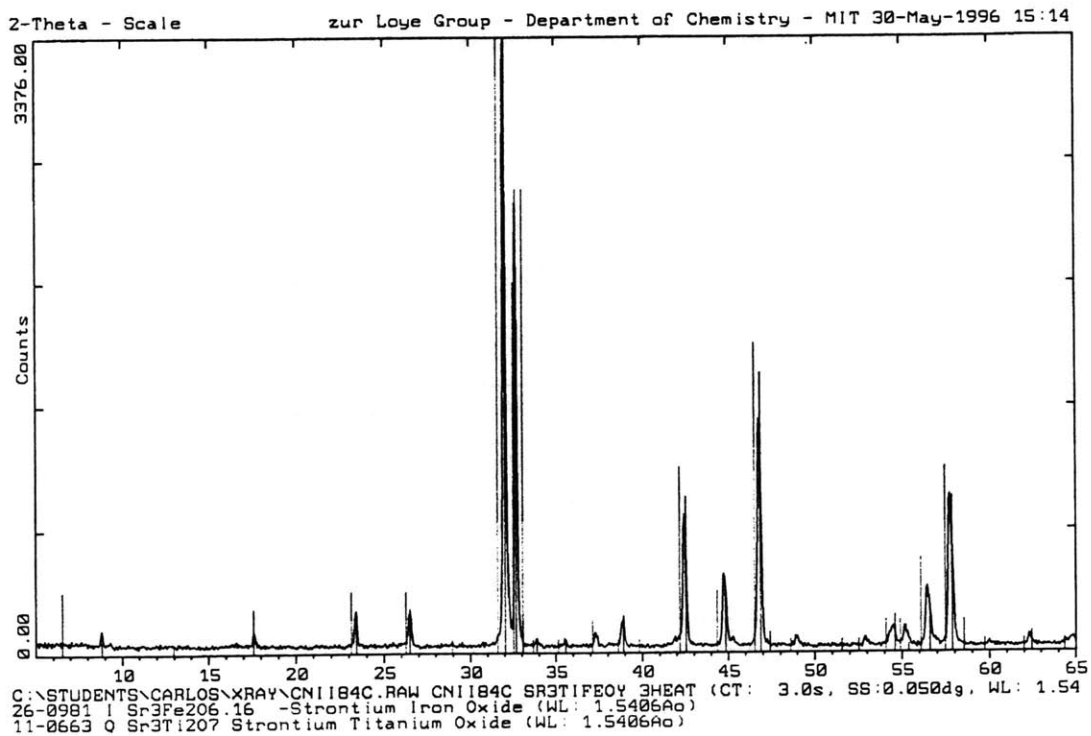11-0663 Q Sr3Ti2O7 Strontium Titanium Oxide (WL: 1.5406Ao)

Figure 5.3. X-ray diffraction powder pattern for Sr$_3$TiFeO$_{7-\delta}$

Table 5.1 List of cell parameters of synthesized Ruddlesden-Popper phases.

Compound	Cell parameters	
	a (Å)	c(Å)
$Sr_3Ti_2O_7$	3.907(1)	20.37(1)
$Sr_3Ti_{1.98}Ga_{0.02}O_{6.99}$	3.901(2)	20.36(1)
$Sr_3Ti_{1.95}Ga_{0.05}O_{6.975}$	3.897(2)	20.34(1)
$Sr_3Ti_{1.9}Ga_{0.1}O_{6.95}$	3.894(3)	20.31(2)
$Sr_3Ti_{1.8}Ga_{0.2}O_{6.9}$	3.889(2)	20.30(1)
$Sr_3Ti_{1.75}Ga_{0.25}O_{6.875}$	3.894(1)	20.33(1)
$Sr_3Ti_{1.8}Al_{0.2}O_{6.9}$	3.882(2)	20.30(1)
$Sr_3Ti_{1.75}Al_{0.25}O_{6.875}$	3.889(2)	20.34(1)
$Sr_{2.9}La_{0.1}Ti_{1.8}Al_{0.2}O_{6.95}$	3.883(1)	20.31(1)
$Sr_3Ti_{1.9}In_{0.1}O_{6.95}$	3.909(1)	20.35(1)
$Sr_3Zr_2O_7$	4.104(1)	20.93(1)
$Sr_3Zr_{1.9}Ga_{0.1}O_{6.95}$	4.104(1)	20.91(1)
$Sr_3Zr_{1.9}Al_{0.1}O_{6.95}$	4.101(1)	20.90(1)
$Sr_3Ti_{1.8}Co_{0.2}O_7$	3.888(1)	20.30(1)
$Sr_3Ti_{1.6}Co_{0.4}O_7$	3.882(1)	20.29(1)
$Sr_3Ti_{1.4}Co_{0.6}O_7$	3.878(1)	20.25(1)
$Sr_3Ti_{1.2}Co_{0.8}O_7$	3.869(1)	20.22(1)
Sr_3TiCoO_7	3.862(1)	20.19(1)
$Sr_3Ti_{1.5}Fe_{0.5}O_7$	3.891(2)	20.27(1)
Sr_3TiFeO_7	3.884(1)	20.26(1)
$Sr_3Ti_{0.5}Fe_{1.5}O_7$	3.870(1)	20.17(1)
$Sr_3Fe_2O_7$	3.855(1)	20.12(1)

$Sr_3Ti_{1.5}Mn_{0.5}O_7$	3.865(2)	20.21(1)
Sr_3TiMnO_7	3.837(2)	20.14(1)
$Sr_3Ti_{0.5}Mn_{1.5}O_7$	3.813(2)	20.09(1)
$Sr_3Mn_2O_7$	3.804(2)	20.10(2)

Table 5.2. XRD powder data (d-spacings and miller indices) for $Sr_3Ti_{1.8}Al_{0.2}O_{6.9}$

2theta (deg)	d(Å)	h	k	l
8.78	10.06	0	0	2
17.50	5.06	0	0	4
23.33	3.810	1	0	1
26.36	3.379	0	0	6
31.88	2.805	1	0	5
32.57	2.747	1	1	0
33.80	2.650	1	1	2
35.35	2.537	0	0	8
37.21	2.414	1	1	4
38.72	2.324	1	0	7
42.33	2.134	1	1	6
44.63	2.029	0	0	10
46.68	1.944	2	0	0
48.80	1.865	1	1	8
52.79	1.733	2	1	1
54.33	1.687	2	0	6
55.00	1.668	1	0	11
56.24	1.634	1	1	10
57.57	1.600	2	1	5

Table 5.3. XRD powder data (d-spacings and miller indices) for $Sr_3TiCoO_{7-\delta}$

2theta (deg)	d(Å)	h	k	l
8.79	10.05	0	0	2
17.59	5.04	0	0	4
23.47	3.788	1	0	1
26.49	3.362	0	0	6
32.08	2.787	1	0	5
32.78	2.730	1	1	0
34.00	2.634	1	1	2
37.42	2.401	1	1	4
38.95	2.310	1	0	7
42.61	2.120	1	1	6
44.87	2.018	0	0	10
47.02	1.931	2	0	0
49.08	1.855	2	0	3
55.36	1.658	1	0	11
56.63	1.624	1	1	10
57.99	1.4837	2	1	5

Table 5.4. XRD powder data (d-spacings and miller indices) for $Sr_3TiFeO_{7-\delta}$

2theta (deg)	d(Å)	h	k	l
8.70	10.15	0	0	2
17.55	5.05	0	0	4
23.31	3.814	1	0	1
26.40	3.374	0	0	6
31.92	2.802	1	0	5
32.61	2.743	1	1	0
33.78	2.651	1	1	2
35.48	2.528	0	0	8
37.23	2.413	1	1	4
38.78	2.320	1	0	7
42.41	2.129	1	1	6
44.72	2.025	0	0	10
46.74	1.942	2	0	0
48.87	1.862	1	1	8
52.89	1.730	2	1	1
54.43	1.684	2	0	6
55.16	1.664	1	0	11
56.40	1.630	1	1	10
57.69	1.597	2	1	5

| 60.01 | 1.5404 | 2 | 0 | 8 |
| 62.28 | 1.4895 | 2 | 1 | 7 |

Table 5.5. Ionic radii for relevant cations. Taken from Shannon.[6]

Cation	Ionic radius (Å)
Ti^{4+}	0.605
Zr^{4+}	0.72
Al^{3+}	0.535
Ga^{3+}	0.620
In^{3+}	0.800
Co^{4+}	0.53
Co^{3+}	0.545 (LS)
	061 (HS)[a]
Fe^{4+}	0.585
Mn^{4+}	0.530

[a] LS: low spin; HS: high spin.

Figure 5.4. Variation of cell parameters with Ga concentration in $Sr_3Ti_{2-x}Ga_xO_{7-\delta}$

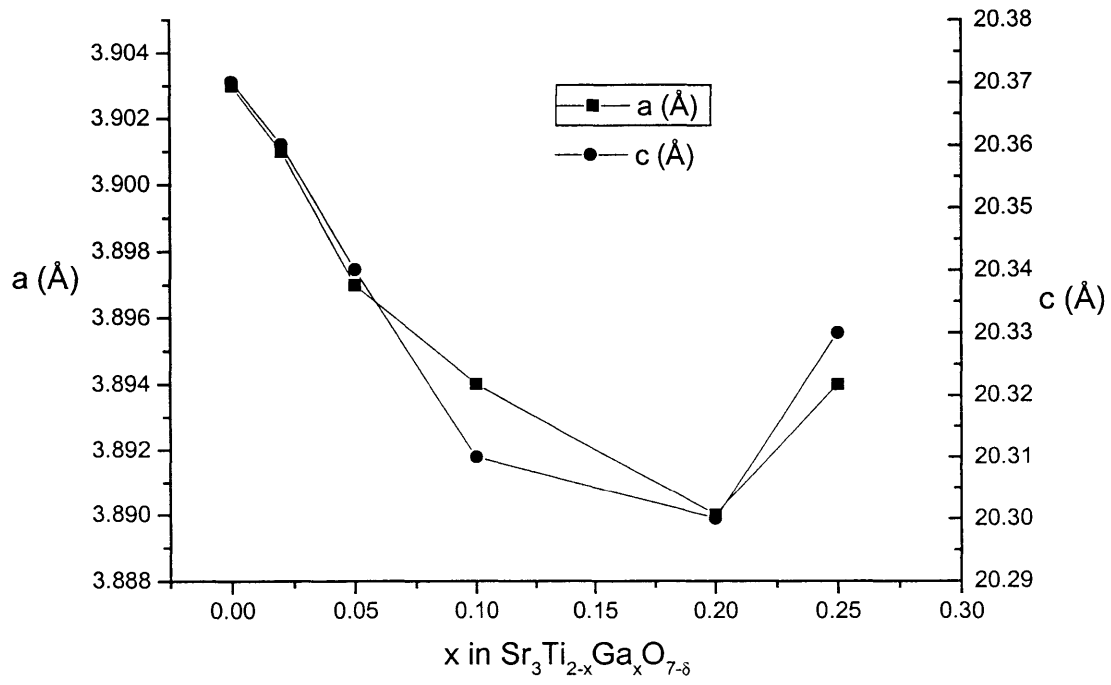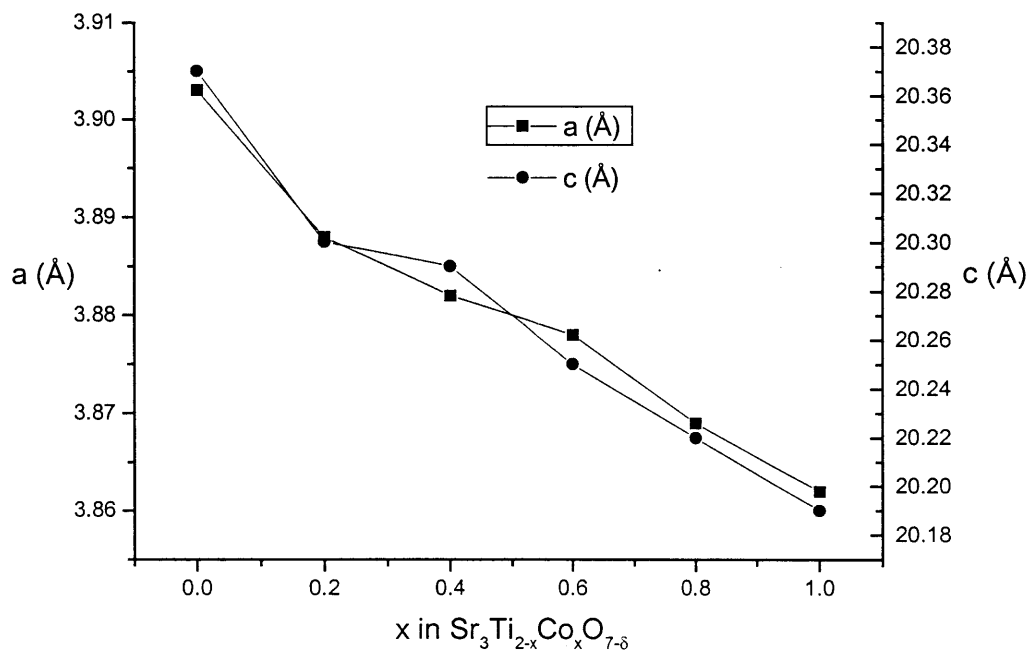**Figure 5.5. Variation of cell parameters with Co concentration in $Sr_3Ti_{2-x}Co_xO_{7-\delta}$**

Figure 5.6. Variation of cell parameters with Fe concentration in $Sr_3Ti_{2-x}Fe_xO_{7-\delta}$

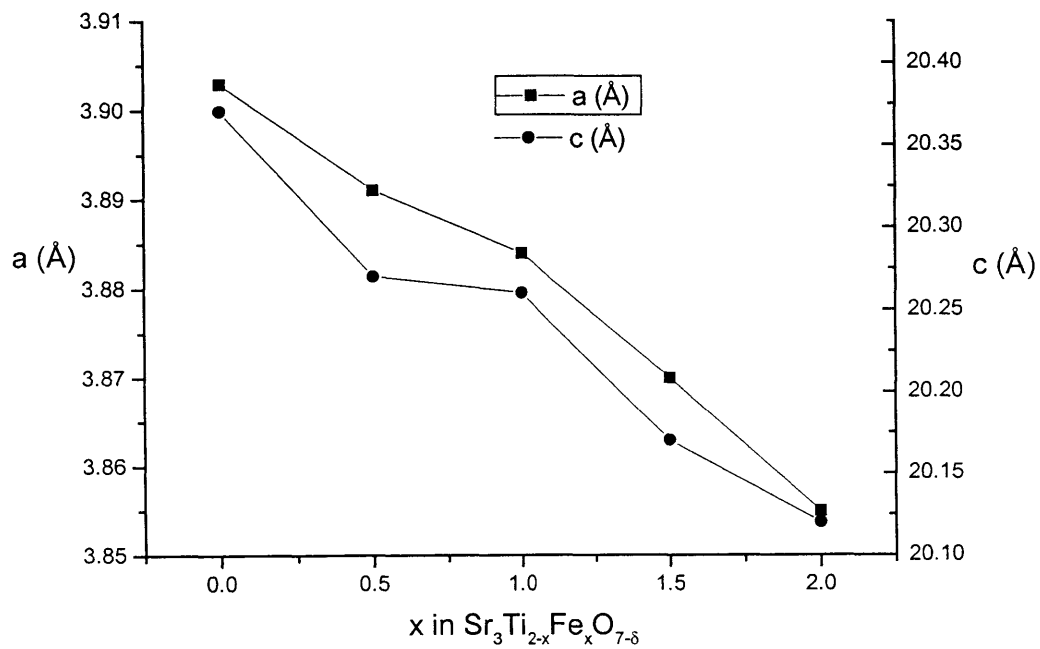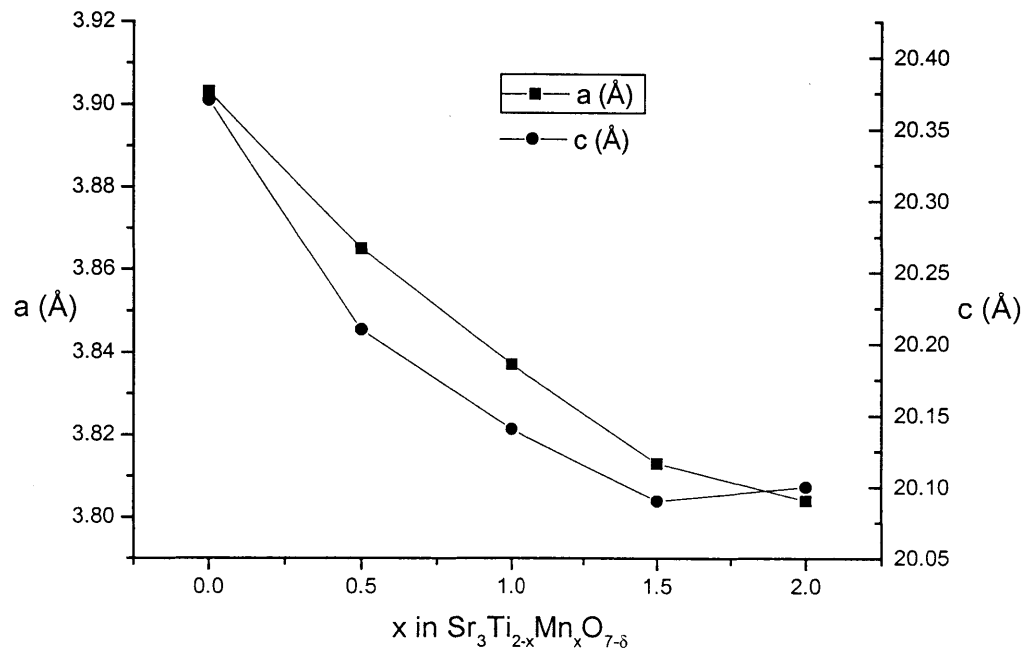**Figure 5.7. Variation of cell parameters with Mn concentration in $Sr_3Ti_{2-x}Mn_xO_{7-\delta}$**

5.3. Electrical conductivity

The electrical conductivity of the synthesized compounds was studied by 2-probe AC impedance spectroscopy. Because these materials were new and their electrical properties unknown, we first studied their conductivity in air as a function of temperature to get an idea of the magnitude of the conductivity. However, this measurement alone did not provide information regarding the charge carriers responsible for the conduction observed and, therefore, measurements of conductivity as a function of $p(O_2)$ at various temperatures were carried out.

A plot of conductivity as a function of temperature for two sample compositions is shown in Figure 5.8. The main feature of interest in this graph is the difference in slope between the heating and cooling cycles. The lower slope in the cooling cycle implies a decrease in the activation energy with respect to the heating cycle. Such a hysteresis has been observed in other systems, most notably the Aurivillius phases,[7,8] but also in other perovskite-type materials.[9] The plots of log (σ) vs. 1/T for all compositions studied exhibit this hysteresis. The plots of log (σ) vs. 1/T for all doped titanates are shown in Figure 5.9; the data for doped zirconate compositions are shown in Figure 5.10 (for the sake of clarity, only cooling cycles are shown).

A number of features about Figure 5.9 should be noted. First, the magnitude of the total conductivity for the fixed valent-doped phases is, in general, not very high (about 10^{-3} S/cm at 950 °C in the most conductive material, $Sr_3Ti_{1.75}Ga_{0.25}O_{6.875}$). Secondly, the conductivity of all doped materials is higher than that of the parent phase. Nonetheless, the increase in overall conductivity is quite low, the exception being the Co-doped phase, which exhibits a conductivity of 2.4×10^{-3} S/cm at 950 °C. For all fixed valent–doped phases, the largest increase observed is only of about an order of magnitude. Another feature of interest is that the slope of all fixed valent-doped phases is similar, whereas that of the Co-doped material is lower. This difference

135

may be translated into activation energies, which were in the range 0.95-1.1 eV and 0.8-0.87 eV for the heating and cooling cycles, respectively, for the fixed valent-doped phases. In contrast, the activation energies for $Sr_3Ti_{1.8}Co_{0.2}O_{7-\delta}$ are about 0.52 and 0.38 eV for the heating and cooling cycles, respectively. Table 5.6 provides a list of all the activation energies obtained, not only in air but also under other atmospheres.

The conductivity of the doped zirconates is lower than that of the doped titanates by approximately an order of magnitude (see Figure 5.10). As was the case in the family of titanates, addition of dopants results in an increase of the total conductivity by about an order of magnitude. Also, the slopes are similar in all cases. The highest conductivity, observed for the doped compositions, is about 3×10^{-4} S/cm at 950 °C. The activation energies are typically somewhat higher than that of the titanate samples by about 0.1 eV. Furthermore, the doped materials display activation energies about 0.1 eV lower than that of the parent material.

As pointed out above, the total conductivity of these materials in air is low. These values represent the sum of all contributions from the various possible charge carriers; that is, both ionic and electronic. Hence, it is of interest to more fully characterize the type of conductivity measured. In order to do so, and following the treatment explained in Chapter 3, we carried out measurements of conductivity as a function of oxygen partial pressure.

The conductivity of a number of Al and Ga-doped compositions as a function of oxygen partial pressure is shown in Figures 5.11-5.16. Figure 5.11 shows the behavior of a few different Al and Ga-doped compositions at 700 °C. It is worth noting a few features of this graph. First, there are 3 different regions that can be observed, corresponding to 3 different slopes. At high $p(O_2)$ ($>10^{-5}$ atm), the conductivity decreases with decreasing $p(O_2)$. This region displays a slope of approximately 0.25, indicating p-type conductivity. At intermediate $p(O_2)$'s, the conductivity is

nearly constant, suggesting the presence of an electrolytic domain. At very low $p(O_2)$, a slight

increase in conductivity is seen, indicative of n-type electronic conductivity. Secondly, the

magnitude of the conductivities in the $p(O_2)$-independent regime for all samples does not exceed

10^{-5} S/cm, a low value. Furthermore, the conductivities in the electrolytic regime for the

Ga-doped compositions are higher than those found in the Al-doped samples for the same dopant

content, although no trend is observed for the conductivity as a function of gallium concentration

in this region (see Figure 5.18). For the sample with composition $Sr_3Ti_{1.75}Al_{0.25}O_{6.875}$, the last

three data points at very low $p(O_2)$ represent a drop in conductivity of more than two orders of

magnitude. XRD powder patterns on this pellet sample revealed partial decomposition at the

surface.

Figures 5.12-5.14 show plots of log σ vs. log $p(O_2)$ at several temperatures for samples

doped with several concentrations of Ga. The overall trend is also similar for all compositions,

displaying the three distinct regimes. We should also note that the electrolytic regime shrinks

with increasing temperature. The highest conductivity observed in the $p(O_2)$-independent regime

is 2×10^{-4} S/cm at 1000 °C for the sample with composition $Sr_3Ti_{1.98}Ga_{0.02}O_{6.99}$. The plots are

shown with the corresponding fits to equation 3.26. Figure 5.17 shows an example of a fit of the

data to equation 3.26 together with the individual contributions from hole, electron and ionic

conductivities (straight lines). The dependence of the ionic conductivity on dopant content is

shown in Figure 5.18. With the data at several different temperatures, one can generate

Arrhenius-type plots and extract the activation energies. A complete table of activation energies

corresponding to ionic conductivities is provided in Table 5.6. We should note that for the

Ga-doped compositions, the activation energy varies between 1.23 and 1.59 eV, with the highest

activation energy (1.59 eV) corresponding to $Sr_3Ti_{1.95}Ga_{0.05}O_{6.975}$, and the lowest (1.23 eV)

corresponding to $Sr_3Ti_{1.98}Ga_{0.02}O_{6.99}$. Similar dopant concentrations for Al and Ga result in a higher activation energy for the former case (1.59 eV vs. 1.47 eV).

Figures 5.15 and 5.16 show the dependence of the conductivity as a function of oxygen partial pressure for some Al-doped materials, with the corresponding fits to equation 3.26. As for the Ga-doped compositions, the three distinct regions are again present, with the width of the $p(O_2)$-independent regime shrinking with increasing temperature. The highest ionic conductivity was 1 x 10^{-5} S/cm at 800 °C for the composition $Sr_3Ti_{1.8}Al_{0.2}O_{6.9}$. The activation energies for ionic conduction are listed in Table 5.6., and are, in all cases, higher than those found for the Ga-doped materials with similar dopant content.

The fits to the data using equation 3.26 allow us to extract the individual contributions of hole, electron and ionic conductivities. For low Ga content (x=0.02 and 0.05) a good fit is obtained; however, with higher dopant concentrations, the electrolytic domain widens, providing fewer data points at very low $p(O_2)$. Consequently, while it was possible to fit the data, the accuracy of the fit of the electronic component of the conductivity may not be as good at high dopant levels.

The three parameters A, B and C, extracted from these fits, were used to obtain the oxidation and reduction enthalpies, E_{ox} and E_r, and the ionic conductivity from equations 3.28, 3.30 and 3.31. As outlined in Chapter 3, the thermal bandgap may also be readily obtained from E_{ox} and E_r. Table 5.7 summarizes the data obtained in this manner. The oxidation enthalpy appears to increase with increasing dopant content, as can be seen with M= Ga (see Figure 5.22). On the other hand, the reduction enthalpy and thermal bandgap do not show any clear trends with dopant concentration. Thermal bandgap energies were in the 3.2-3.9 eV range.

Doping with transition metal cations has a different impact on the conductivity. The dependence of the conductivity of $Sr_3Ti_{1.8}Co_{0.2}O_{7-\delta}$ on oxygen partial pressure at temperatures between 600-1000 °C is shown in Figure 5.19. The conductivity decreases with decreasing $p(O_2)$ between 1 and 10^{-5} atm, followed by a regime which exhibits little or no dependence of conductivity on $p(O_2)$. In the first region, the line follows a slope of approximately 1/6. The total conductivity increases with increasing temperature, and the $p(O_2)$-independent regime shows a total conductivity at 1000 °C of 6 x 10^{-3} S/cm. The data points were fit to equation 3.36, and the fits are shown in the figure as well.

Fitting the data of Figure 5.19 allows a rough determination of the energy required to ionize Co^{4+} to Co^{3+}, E_{Co}, by using equation 3.39 (the presence of Co^{4+} is discussed later in this chapter). We estimate the oxidation enthalpy and the thermal bandgap energy from the data obtained from the fixed valent-doped materials (Table 5.7) and calculate $E_{Co} = 3.61$ eV.

If we compare the conductivity of fixed vs. variable valent-doped Ruddlesden-Popper phases at the same temperature and for the same doping level in the electrolytic regime, the conductivities are higher, by about two orders of magnitude, in the transition metal-doped materials. For example, at 800 °C, the conductivities are 2 x 10^{-3} S/cm and 2 x 10^{-5} S/cm for the Co and Ga-doped, respectively. The activation energies are also significantly different. The calculated ionic activation energy for the Co-doped material is 0.64 eV, in contrast to about 1.47 eV for the fixed-valent dopants, or a difference of about 0.8 eV between the two cases. In the high $p(O_2)$ region, the activation energies also show a significant difference. They are approximately 0.9 and 0.4 eV for the Ga and Co-doped materials, respectively.

The dependence of electrical conductivity on oxygen partial pressure at 700 °C for various Co levels is shown in Figure 5.20. In this case, the same two regions are observed and, in

139

addition, the conductivity drops off sharply at low $p(O_2)$'s for all compositions except x=0.2. The regime at high $p(O_2)$ with decreasing conductivity displays a slope of approximately 1/6 in all cases. The magnitude of the conductivity also increases with increasing dopant concentration. The highest level of apparent ionic conductivity measured in the $p(O_2)$-independent regime is 2×10^{-2} S/cm for $Sr_3Ti_{1.2}Co_{0.8}O_{7-\delta}$. Since the conductivity generally decreased at low $p(O_2)$'s, similar to $Sr_3Ti_{1.75}Al_{0.25}O_{6.875}$, XRD powder patterns of the pellet faces were obtained and revealed partial decomposition. The magnitudes of the conductivities in the $p(O_2)$-independent regime of the Co-doped phases are significantly higher than those observed for the Al and Ga-doped samples. The dependence of the magnitude of the conductivity on Co content at 700 °C is shown in Figure 5.21. A significant increase in the conductivity in the plateau regime is observed, with a maximum value of 2×10^{-2} S/cm.

Figure 5.23 shows the dependence of the electrical conductivity on oxygen partial pressure for a few Fe-doped samples at 700 °C. The general profile observed is similar to that of the Co-doped Ruddlesden-Popper phases. There exists a region at high $p(O_2)$ of decreasing conductivity with decreasing oxygen partial pressure, followed by a region of conductivity nearly independent of $p(O_2)$. This region decreases in width with increasing concentration of iron. The regime is then followed by a sharp drop in conductivity of about 2 orders in magnitude, and then by an increase in conductivity at low $p(O_2)$'s. Again, XRD analysis revealed that partial decomposition of the samples had occurred. In contrast to the Co-doped phases, the conductivity does not increase with increasing iron doping levels. The conductivity in the $p(O_2)$-independent regime is about 1×10^{-2} S/cm. We should note that the presence of this region is barely perceptible in the $Sr_3Ti_{0.5}Fe_{1.5}O_{7-\delta}$ sample, although it indeed looks as if, at about 10^{-5} atm, the conductivity is starting to level out.

The dependence of electrical conductivity on oxygen partial pressure for two Mn-doped compositions at 700 °C is depicted in Figure 5.24. It is obvious from the figure that the profile is vastly different from that seen in all other cases. At $p(O_2) > 10^{-5}$ atm, the conductivity increases slightly, the increase being larger for the sample with a higher Mn concentration. At intermediate $p(O_2)$'s, the conductivity goes through a maximum, then drops to a minimum value at about 10^{-18} atm. At even more reducing atmospheres, the conductivity shows a small increase. As in the Co-doped samples, the conductivity increases with increasing dopant concentration. The maximum conductivity observed is about 3×10^{-2} S/cm for the $Sr_3TiMnO_{7-\delta}$ composition.

Figure 5.8. Conductivity as a function of temperature in air for Ruddlesden-Popper phases showing both heating and cooling cycles

Figure 5.9. Conductivity as a function of temperature for some doped titanate

Ruddlesden-Popper phases

Legend:
- ■ $Sr_3Ti_2O_7$
- ● $Sr_3Ti_{1.8}Al_{0.2}O_{6.9}$
- ▲ $Sr_3Ti_{1.75}Al_{0.25}O_{6.875}$
- ▼ $Sr_3Ti_{1.8}Co_{0.2}O_{7-\delta}$
- ◆ $Sr_3Ti_{1.8}Ga_{0.2}O_{6.9}$
- + $Sr_3Ti_{1.75}Ga_{0.25}O_{6.875}$
- × $Sr_{2.9}La_{0.1}Ti_{1.8}Al_{0.2}O_{6.95}$
- ✳ $Sr_3Ti_{1.9}In_{0.1}O_{6.95}$

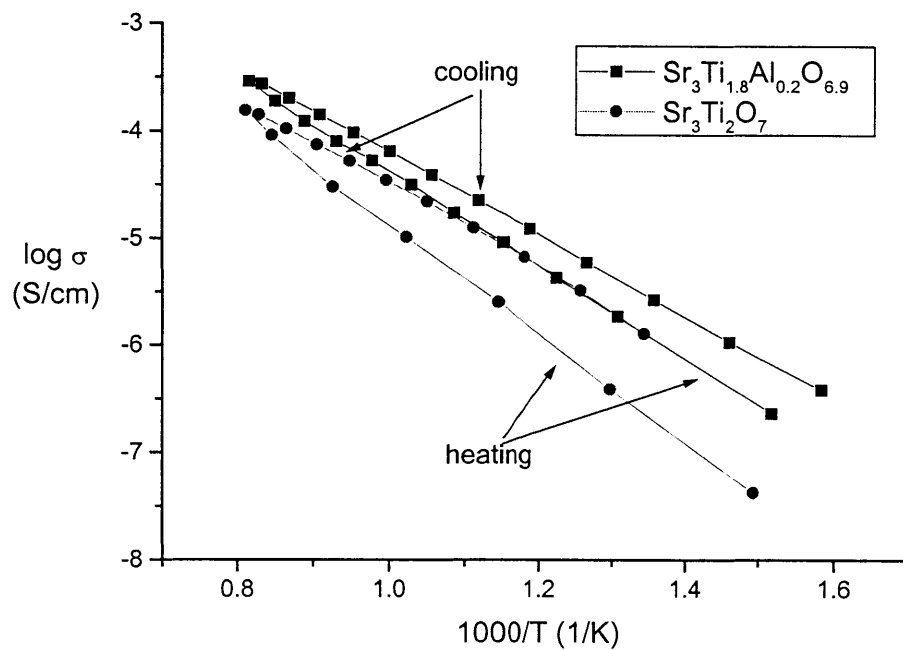y-axis: log σ (S/cm)

x-axis: 1000/T (1/K)
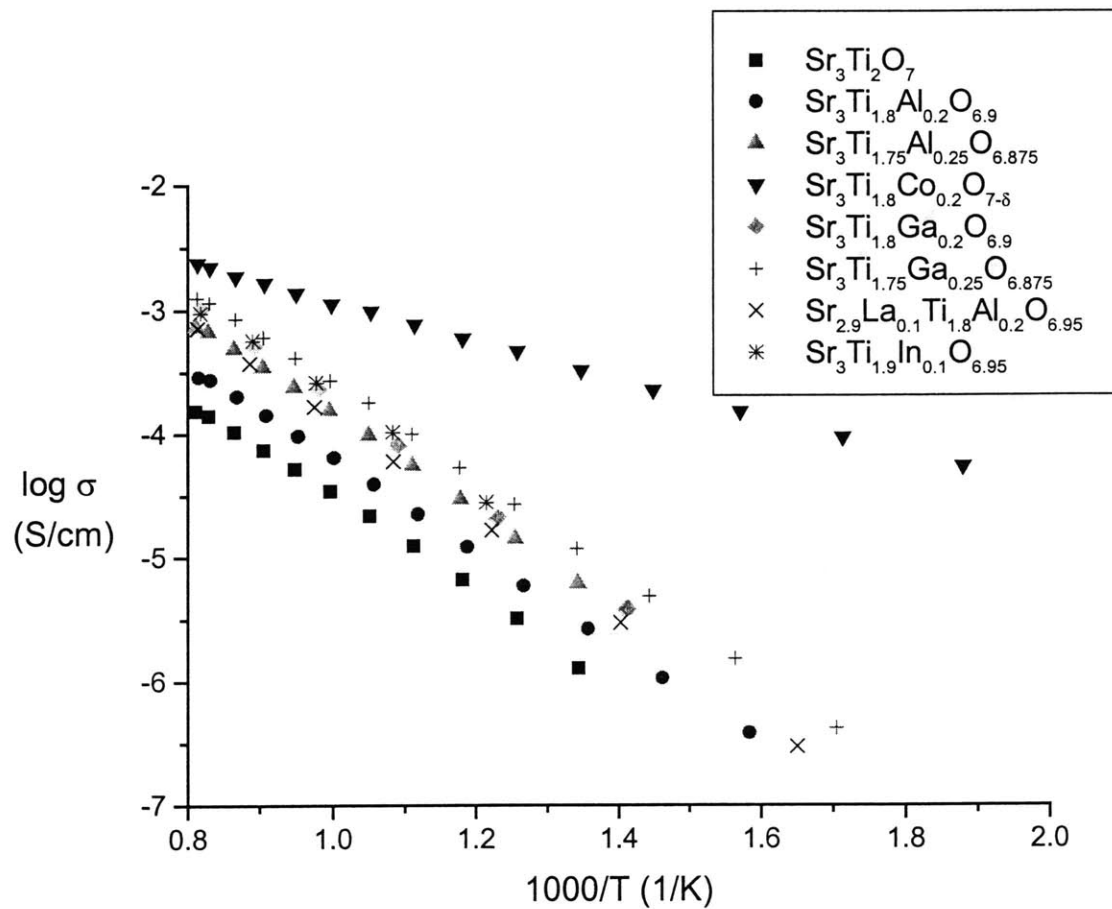
Figure 5.10. Conductivity as a function of temperature for some doped zirconate Ruddlesden-Popper phases
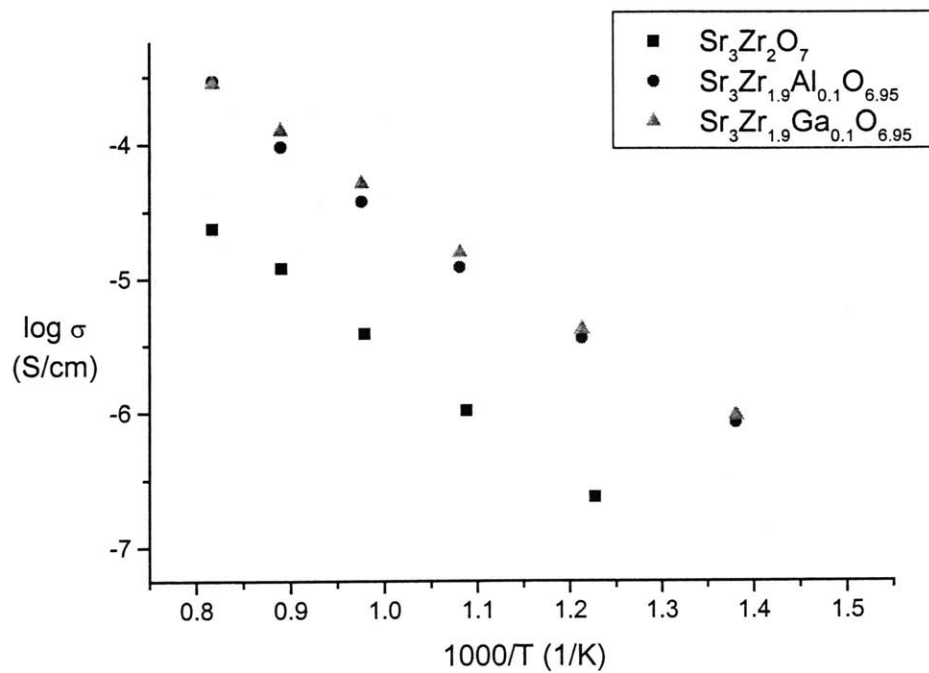
Figure 5.11. Conductivity as a function of oxygen partial pressure for some Al and Ga-doped Ruddlesden-Popper phases at 700 °C
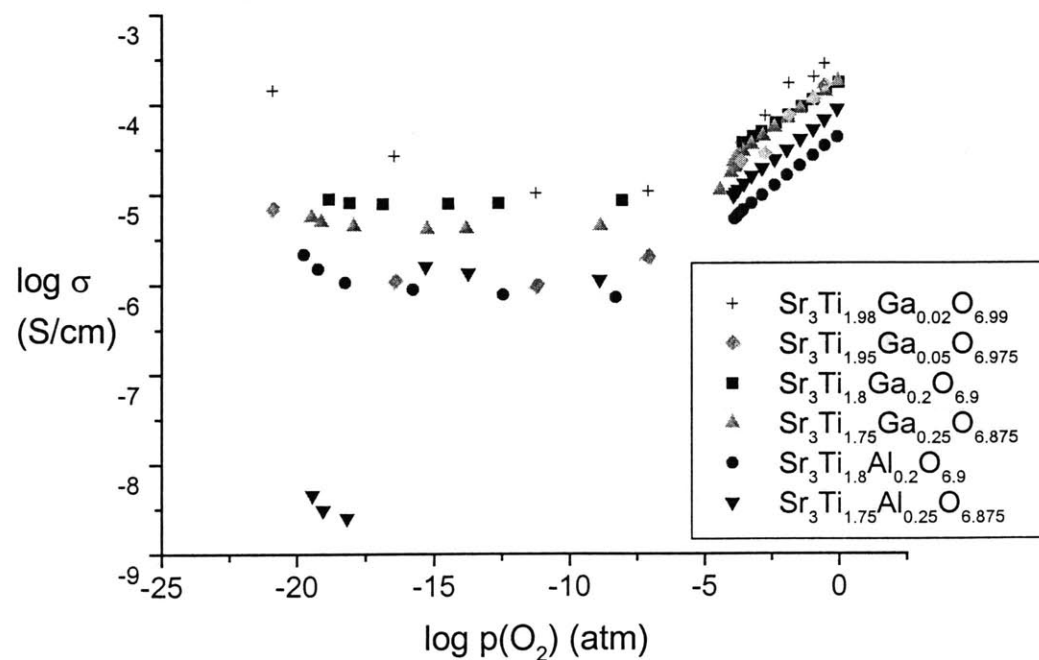
Figure 5.12. Conductivity of $Sr_3Ti_{1.98}Ga_{0.02}O_{6.99}$ as a function of oxygen partial pressure
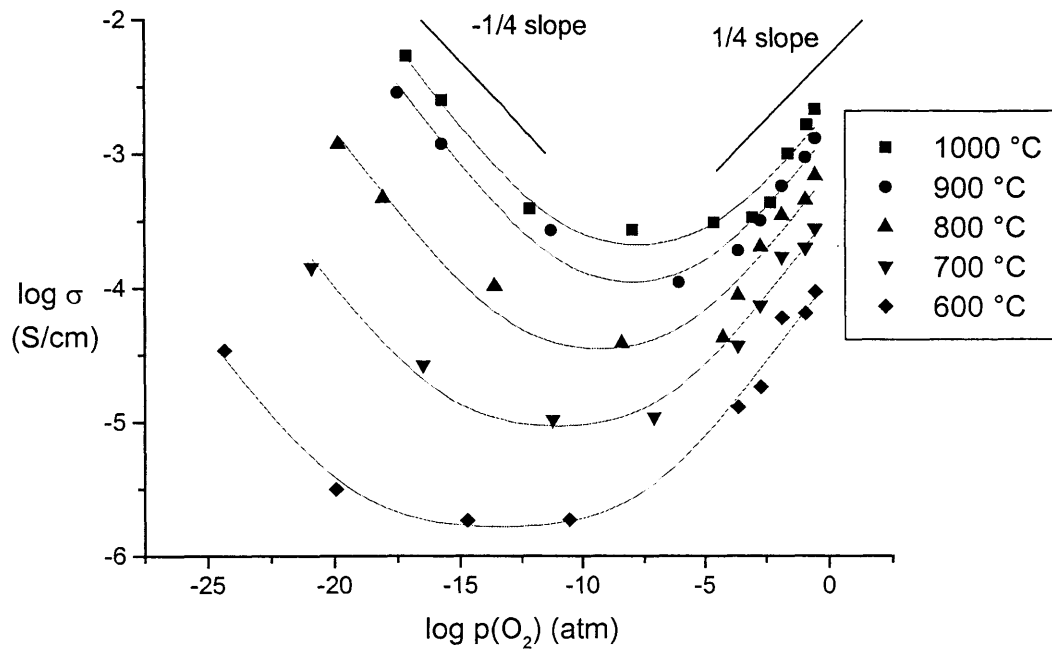
Figure 5.13. Conductivity of $Sr_3Ti_{1.95}Ga_{0.05}O_{6.975}$ as a function of oxygen partial pressure
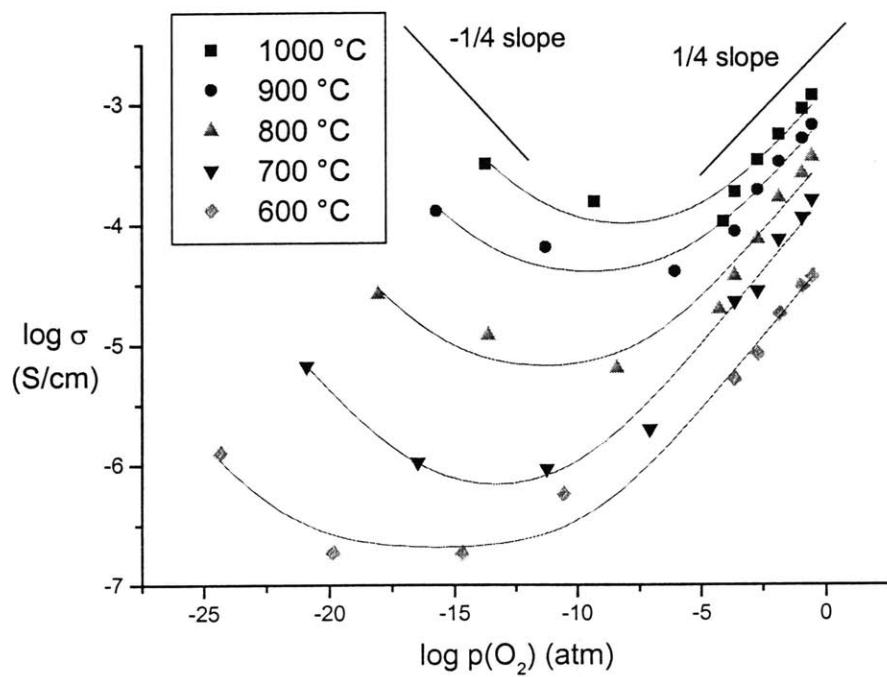
Figure 5.14. Conductivity as a function of oxygen partial pressure at different temperatures for $Sr_3Ti_{1.8}Ga_{0.2}O_{6.9}$
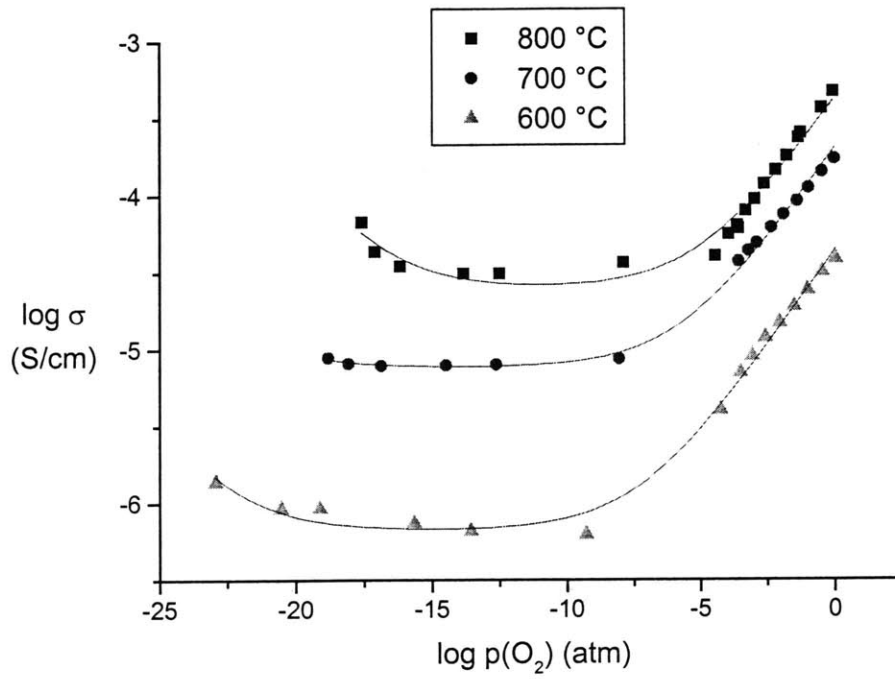
Figure 5.15. Conductivity as a function of oxygen partial pressure at different temperatures for $Sr_3Ti_{1.8}Al_{0.2}O_{6.9}$
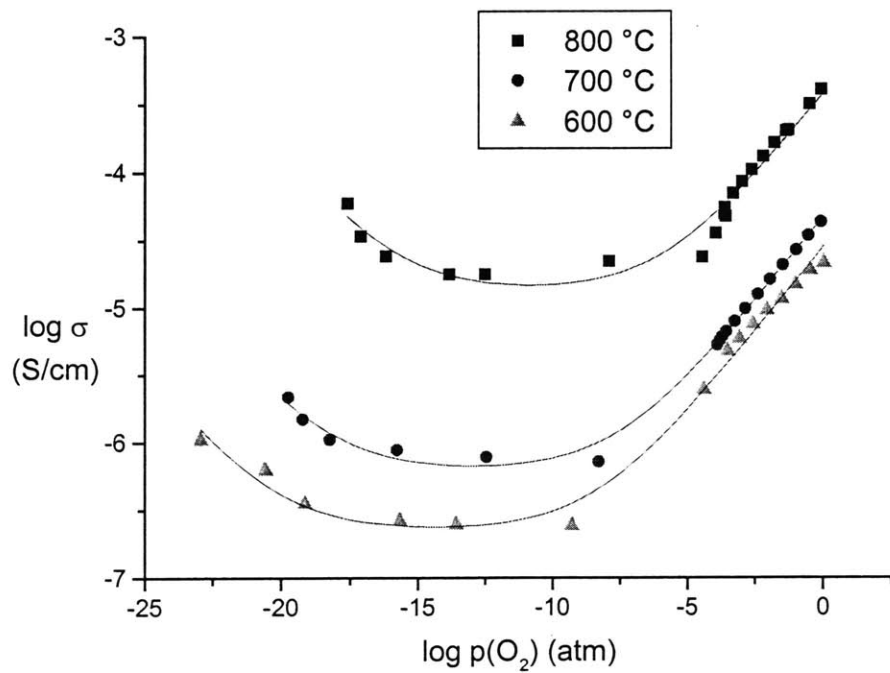
Figure 5.16. Conductivity as a function of oxygen partial pressure for

$Sr_{2.9}La_{0.1}Ti_{1.8}Al_{0.2}O_{6.95}$ at different temperatures
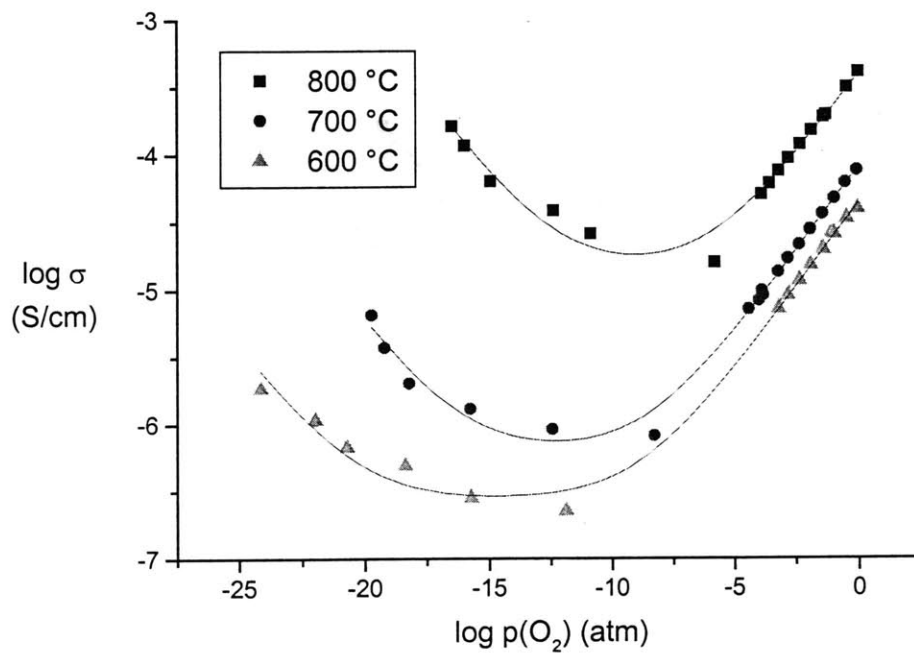
Figure 5.17. Conductivity of $Sr_3Ti_{1.98}Ga_{0.02}O_{6.99}$ as a function of oxygen partial pressure at 1000 °C, showing the fit to equation 3.26 and the sum of the contributions from hole, electron and ionic conductivities
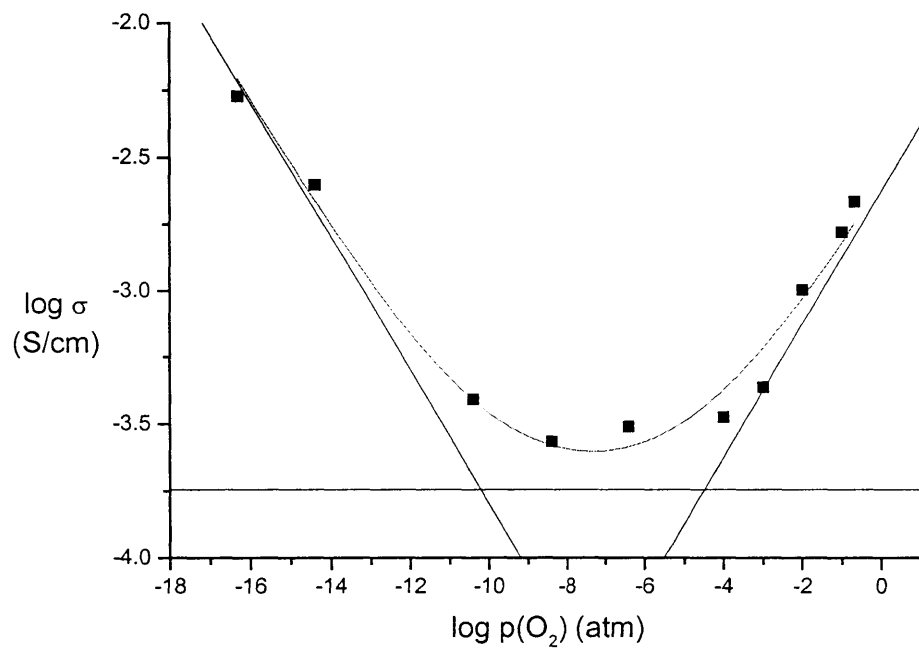
Figure 5.18. Dependence of ionic conductivity on dopant content in $Sr_3Ti_{2-x}M_xO_{7-\delta}$ at 700 °C
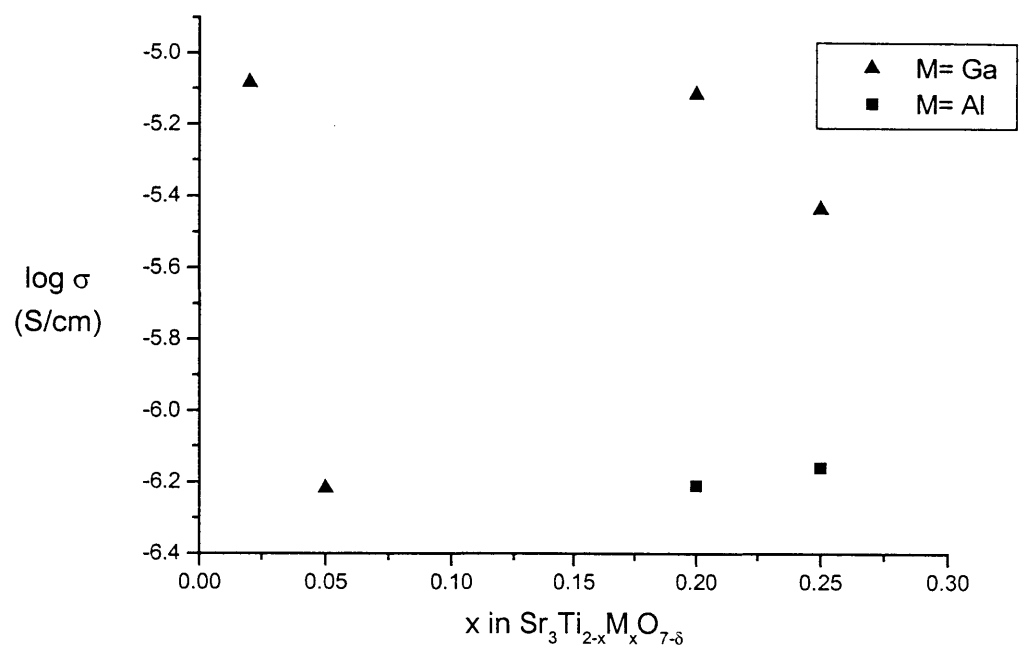
Figure 5.19. Conductivity as a function of oxygen partial pressure for $Sr_3Ti_{1.8}Co_{0.2}O_{7-y}$ at several temperatures

Figure 5.20. Conductivity as a function of oxygen partial pressure for $Sr_3Ti_{2-x}Co_xO_{7-y}$ at 700 °C
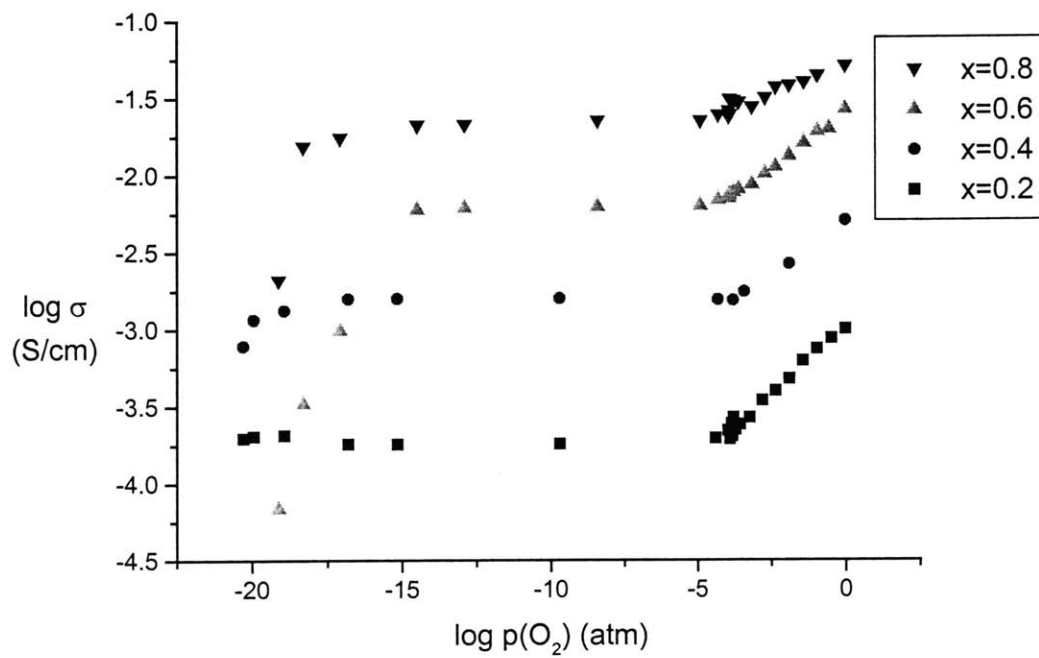
Figure 5.21. Ionic conductivity as a function of x in $Sr_3Ti_{2-x}Co_xO_{7-\delta}$ at 700 °C
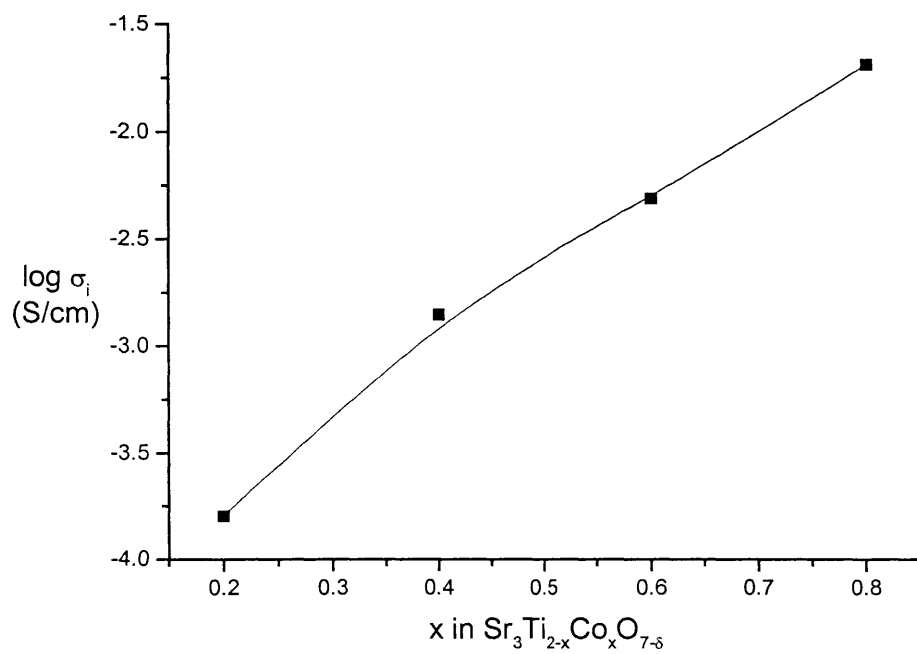
Table 5.6. List of activation energies (in eV units) for different compositions under various atmospheres.

Compound	Air		Electrolytic regime
	Heating	Cooling	
$Sr_3Ti_2O_7$	1.10	0.85	$-$
$Sr_3Ti_{1.8}Al_{0.2}O_{6.9}$	0.95	0.83	1.59
$Sr_3Ti_{1.75}Al_{0.25}O_{6.875}$	1.14	0.86	$-$
$Sr_3Ti_{1.98}Ga_{0.02}O_{6.99}$	$-$	0.85	1.23
$Sr_3Ti_{1.95}Ga_{0.05}O_{6.975}$	$-$	0.91	1.61
$Sr_3Ti_{1.8}Ga_{0.2}O_{6.9}$	1.11	0.90	1.47
$Sr_3Ti_{1.75}Ga_{0.25}O_{6.875}$	1.16	0.85	$-$
$Sr_{2.9}La_{0.1}Ti_{1.8}Al_{0.2}O_{6.95}$	1.08	0.88	1.50
$Sr_3Ti_{1.9}In_{0.1}O_{6.95}$	1.15	0.86	$-$
$Sr_3Zr_2O_7$	1.33	1.07	$-$
$Sr_3Zr_{1.9}Al_{0.1}O_{6.95}$	1.03	0.96	$-$
$Sr_3Zr_{1.9}Ga_{0.1}O_{6.95}$	1.02	0.96	$-$
$Sr_3Ti_{1.8}Co_{0.2}O_y$	0.52	0.38	0.64

Table 5.7. Oxidation and reduction enthalpies (E_{ox} and E_r) and thermal bandgap (E_g) for selected doped Ruddlesden-Popper phases (in eV units).

Compound	E_{ox}	E_r	E_g
$Sr_3Ti_{1.98}Ga_{0.02}O_{6.99}$	1.46	4.84	3.15
$Sr_3Ti_{1.95}Ga_{0.05}O_{6.975}$	1.52	5.78	3.65
$Sr_3Ti_{1.8}Ga_{0.2}O_{6.9}$	1.88	5.40	3.64
$Sr_3Ti_{1.8}Al_{0.2}O_{6.9}$	1.96	5.22	3.59
$Sr_{2.9}La_{0.1}Ti_{1.8}Al_{0.2}O_{6.95}$	1.58	6.24	3.91

Figure 5.22.Variation of oxidation and reduction enthalpies and thermal bandgap with Ga content in $Sr_3Ti_{2-x}Ga_xO_{7-\delta}$
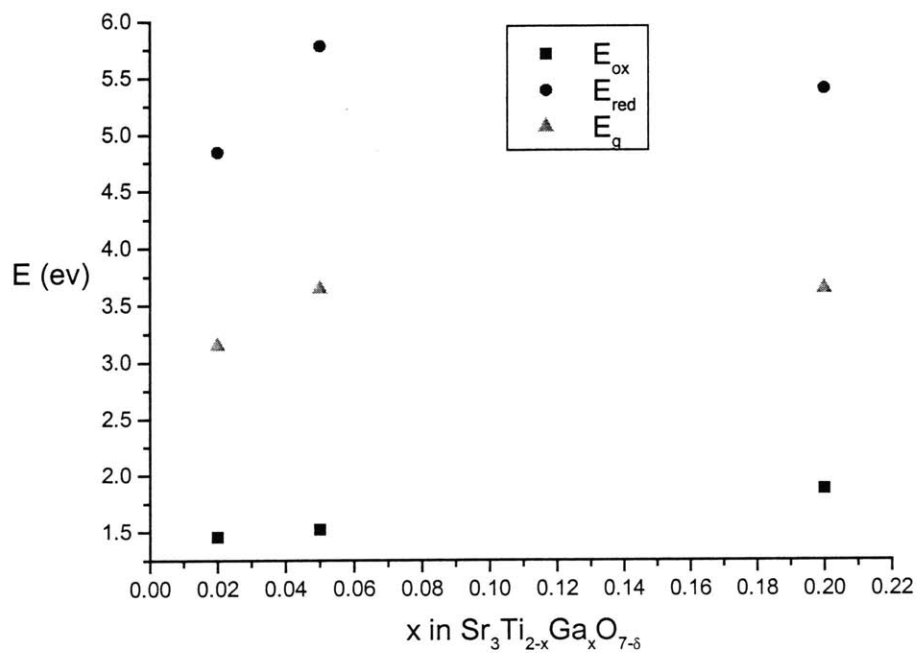
Figure 5.23. Conductivity as a function of oxygen partial pressure for $Sr_3Ti_{2-x}Fe_xO_{7-y}$ at 700 °C

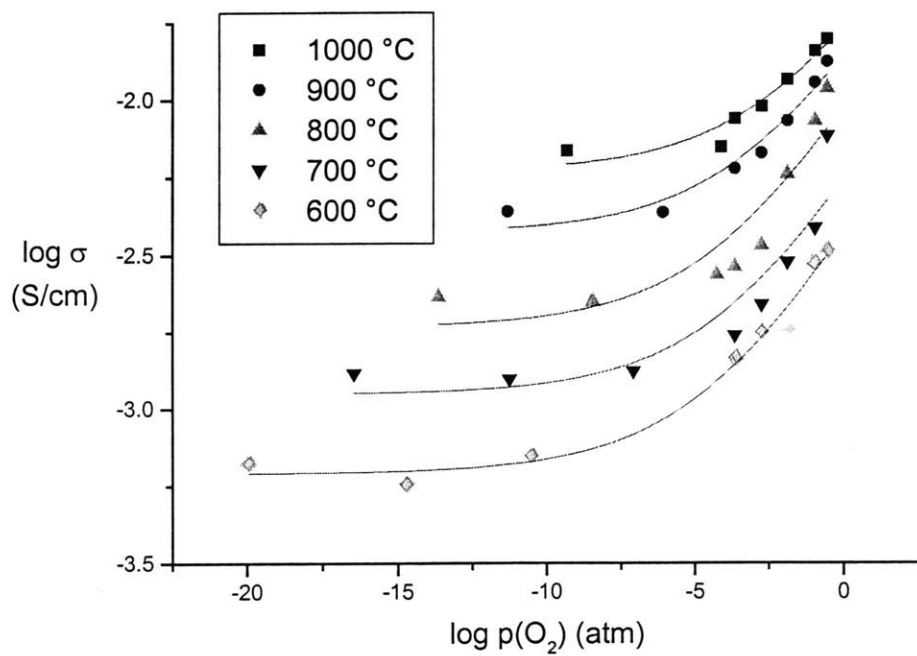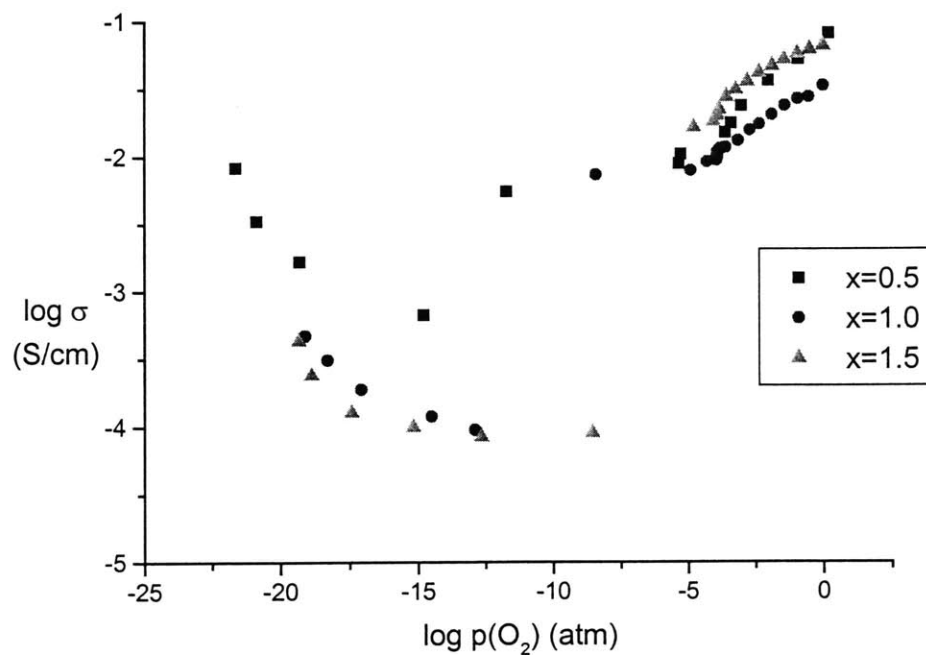**Figure 5.24. Conductivity as a function of oxygen partial pressure for $Sr_3Ti_{2-x}Mn_xO_{7-y}$ at 700 °C**
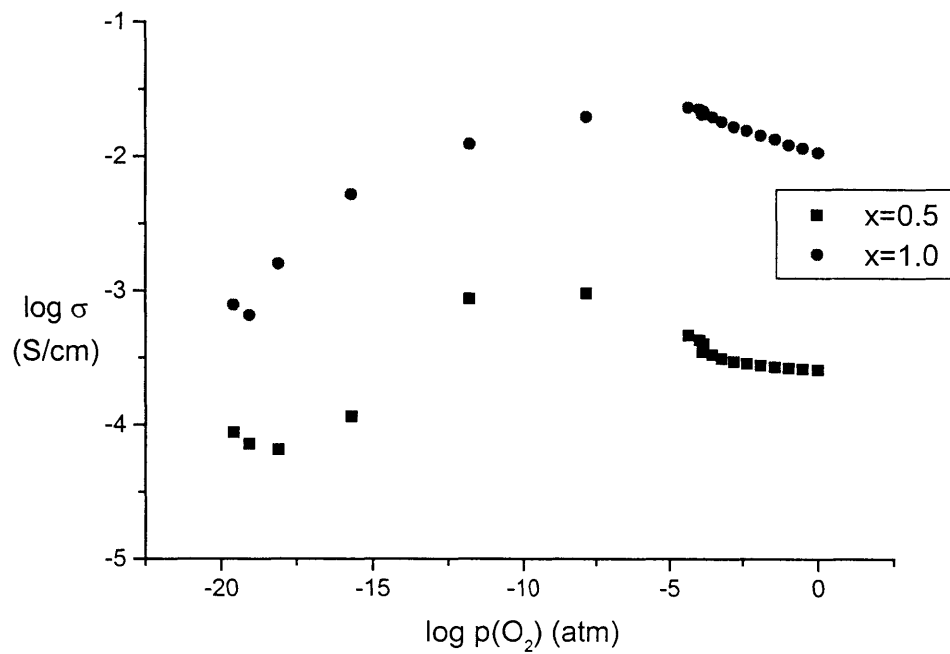
5.4. Oxygen nonstoichiometry

The oxygen nonstoichiometry was studied using the method of iodometric titration. When we were fine-tuning and standardizing the method, several Co-doped compositions, which had been synthesized in air and slowly cooled to room temperature, were used. The results consistently indicated the predominant presence of Co^{4+} in these samples.

More in-depth experiments were undertaken to determine the change of oxygen nonstoichiometry with respect to oxygen partial pressure. Quenched samples from 700 °C under various atmospheres were used for the experiments. The results for these experiments are shown in Figure 5.25. At the highest $p(O_2)$, the average valence of Co is 3.75. From there, the oxygen nonstoichiometry increases linearly following a slope of 1/6. It is important to note that the value of this slope (approximately +1/6) coincides with the slope of conductivity as a function of oxygen partial pressure data at high $p(O_2)$.

Figure 5.25. Oxygen nonstoichiometry of $Sr_3Ti_{1.2}Co_{0.8}O_{7-\delta}$ at 700 °C
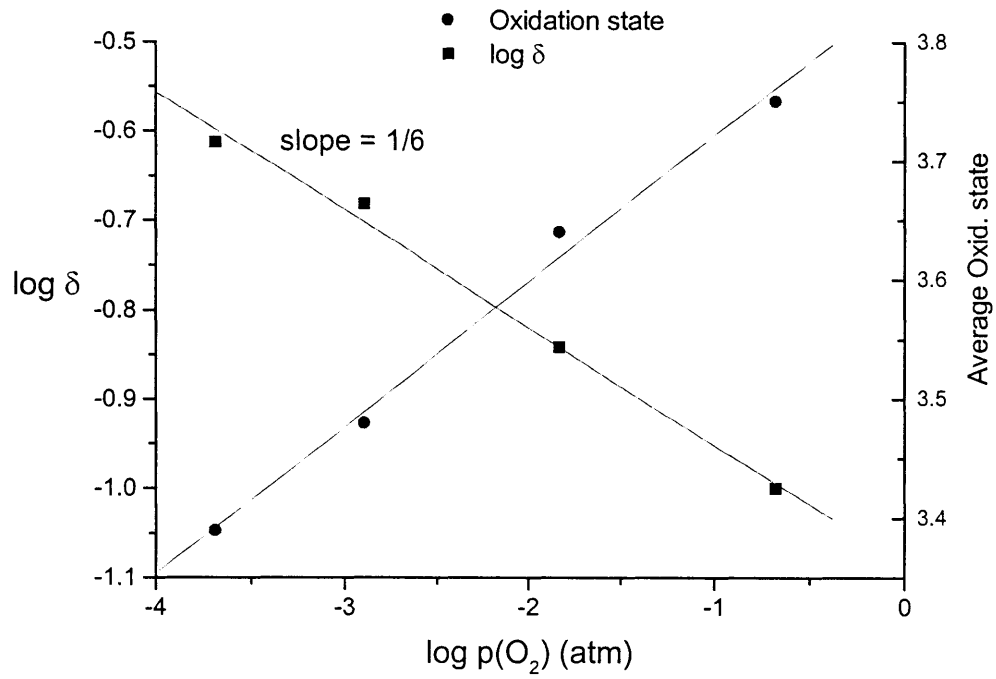
5.5. EMF measurements

Electromotive Force Measurements (EMF) were undertaken to determine the ionic

transference numbers as a function of oxygen partial pressure. After solving the problem with the

sealing material and settling for gold foil, we determined that an appropriate seal could be

formed at 700 or 800 °C. The presence of an appropriate seal was ascertained by noting that gas

flowing through one side of the cell did not result in any gas coming out of the other side. A

bubbler was used for this purpose.

One side of the sample was exposed to $10\%CO/CO_2$ as a reference, while the other side

was exposed to various gas mixtures in order to impose different gradients in oxygen potential.

The gas mixture on the non-reference side was changed going both from low to high $p(O_2)$'s and

vice versa. Before changing the gas on the non-reference side, we made sure we had attained

equilibrium.

A few minutes after imposing an oxygen gradient on both sides of the material, the

voltage across the cell increased rapidly up to a maximum value of approximately 20 mV, at

which point the voltage started slowly decreasing down to a value of about 0 mV (though it was

never exactly 0). For all gases used on the non-reference side, a voltage developed. In addition,

changing the identity of the gas mixture had little effect on the magnitude of the maximum

voltage developed across the cell. Since we suspected a leak in the cell, several attempts were

made to check whether this was the case or not, with no success. Furthermore, switching the

probes gave the same magnitude of the voltage with the opposite sign, as expected. The voltage

was monitored with the aid of a multimeter which could also be used to monitor the resistance

across the cell. In all cases, the magnitude of the resistance measured was in accordance with

what was expected according to the conductivity measurements carried out earlier on a separate

specimen of the same composition. The prolonged use of certain reducing gases (e.g. 10% CO/CO_2 and 1% CO/CO_2) did not result in decomposition of the sample, as determined by the constant value of the resistance measured across the cell.

Therefore, our inability to obtain a clear reading of an equilibrium voltage across the cell did not allow us to calculate ionic transference numbers.

5.6. Measurements of the chemical diffusion coefficient

The chemical diffusion coefficient of a material with composition $Sr_3Ti_{1.6}Co_{0.4}O_{7-\delta}$ was obtained by the relaxation method, as presented in Chapter 4. We were able to obtain a consistent and complete set of data when switching from air to 0.1% O_2/Ar. Consequently, our values for the chemical diffusion coefficient reflect only this set of data.

An example of the profile of the change of resistance with time is provided in Figure 5.26. The first few points (up to about 70-90 seconds) show the same value of resistance, which may be taken as the time it takes for the new gas to sweep out the old mixture. The first, steep part of the curve typically corresponds to gas exchange with the sample surface, whereas the latter part of the curve corresponds to bulk diffusion. The duration of the experiment can be seen as sufficient to achieve equilibrium, as evidenced by the plateau seen after long times.

The data thus obtained was used to obtain a plot of $\ln\left[(\sigma-\sigma_\infty)/(\sigma_0-\sigma_\infty)\right]$ vs. time (Figure 5.27). The first part of the graph is believed to correspond to surface exchange and the linear part (t > 1000 sec) to the diffusion process in the bulk. The slope of the linear portion is used to calculate the chemical diffusion coefficient, $\tilde{D}$, at the various temperatures of the experiments.

The scattering of the data after long times (t > 8000 sec) is due to the very small changes in resistance with time during final equilibration.

The chemical diffusion coefficients thus obtained are plotted as a function of temperature in Figure 5.28. In this figure $D_{chem} = \tilde{D}$, and the data is plotted in the more usual form of $\log \tilde{D}$ vs. 1/T instead of using $\ln \tilde{D}$. The chemical diffusion coefficient, by fitting the data, was determined to be:

$$\tilde{D} = (5.9 \pm 4.0) \times 10^{-3} \exp (-0.45 \pm 0.12 \ eV/kT) \ cm^2 sec^{-1}$$

These values may be translated into chemical diffusion coefficients of about $6.8 \times 10^{-6} \ cm^2 sec^{-1}$ at 700 °C and $1.13 \times 10^{-5} \ cm^2 sec^{-1}$ at 800 °C. Because we did not have the chance to collect more data, we obtained large error bars for both the pre-exponential term and the activation energy. This value may be compared to the activation energy obtained in the plateau region of

$Sr_3Ti_{1.8}Co_{0.2}O_{7-\delta}$ of 0.66 eV. If we assume that $\tilde{D} = D_i$ (see Chapter 3), the ionic conductivity may be calculated using equation 3.12, since we now have specific values for the concentration of oxygen vacancies (from nonstoichiometry measurements) and mobility of oxygen (from the diffusion coefficient). This calculation yields a value of about $\sigma = 0.03$ S/cm at 700 °C, or about an order of magnitude larger than that observed in the conductivity measurements. Conversely, we can work back and calculate the diffusion coefficient of the electrons, assuming that at $0.1\%O_2$ about 90% of the conductivity is due to electronic conduction, since we know the overall chemical diffusion coefficient. The chemical diffusion coefficient of oxygen may be calculated from the conductivity data in the plateau region, assuming it corresponds to ionic conductivity.

Thus, the chemical diffusion coefficient of oxygen is 6.4×10^{-7} cm^2sec^{-1}, while the diffusion coefficient of the electrons at 700 °C is calculated to be 6.22×10^{-5} cm^2sec^{-1}.

Figure 5.26. Plot of resistance as a function of time after a sudden change in oxygen partial

pressure
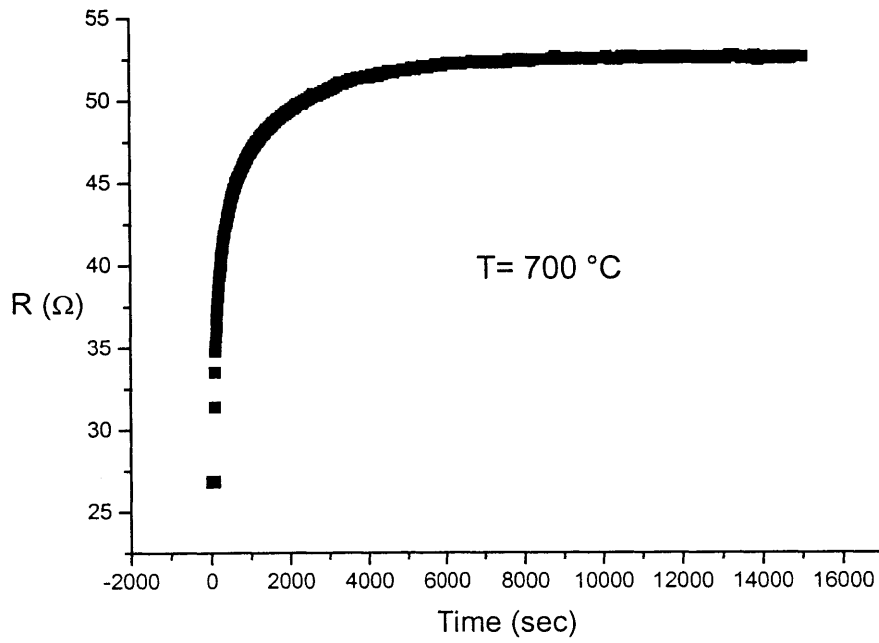
Figure 5.27. Plot of $\ln[(\sigma-\sigma_\infty)/(\sigma_0-\sigma_\infty)]$ vs. time derived from the same run shown in the previous figure
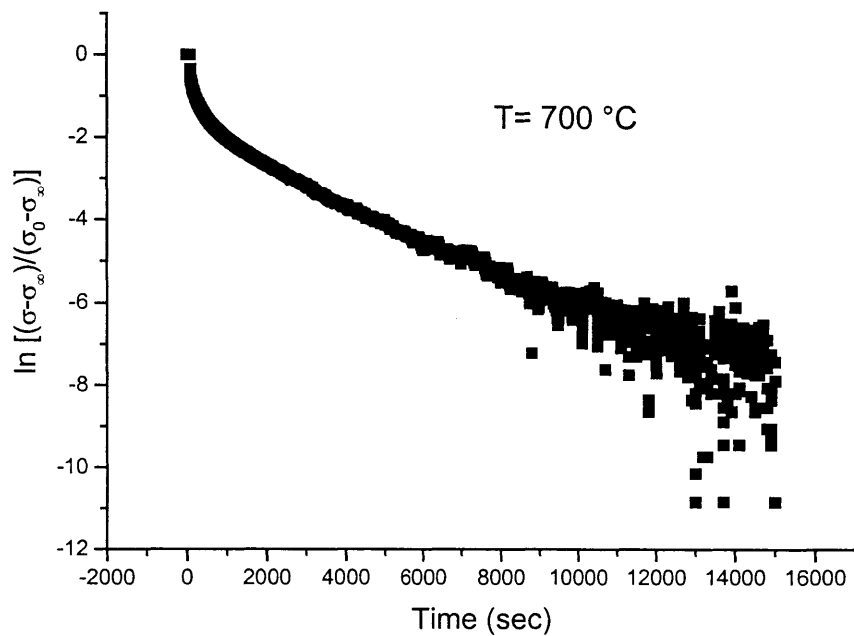
Figure 5.28. Dependence of the chemical diffusion coefficient on temperature
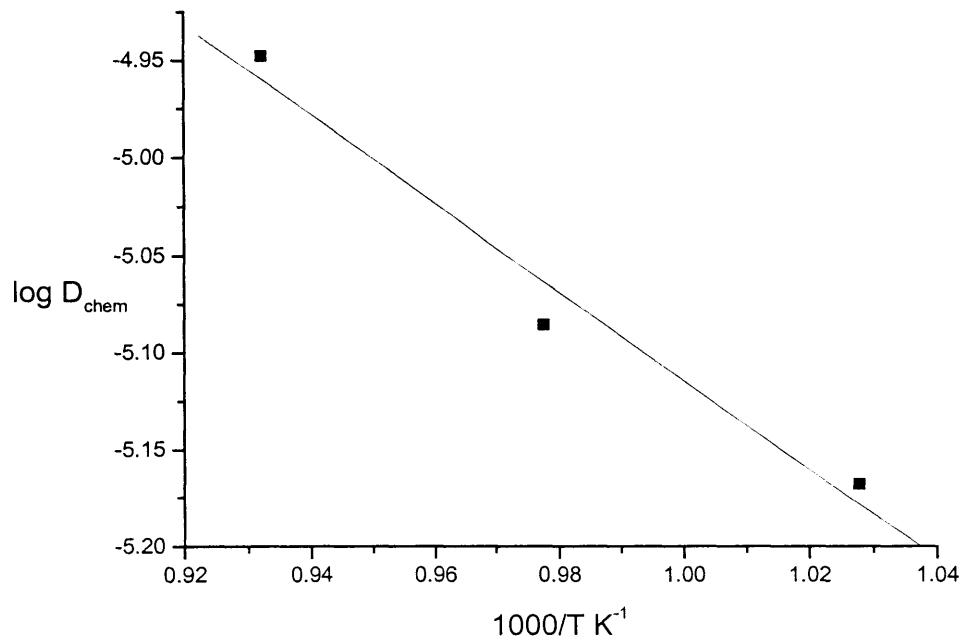
References

1. Ruddlesden, S. N. and Popper, P., *Acta Cryst.,* **1957**, *10*, 538-539.

2. Mizutani, *J. Chem. Soc. (Japan) Ind. Ed.,* **1970**, *73*, 1097-1103.

3. Dann, S. E. and Weller, M. T., *J. Solid State Chem.,* **1995**, *115*, 499-507.

4. Dann, S. E., Weller, M. T. and Currie, D. B., *J. Solid State Chem.,* **1992**, *97*, 179-185.

5. Ruddlesden, S. N. and Popper, P., *Acta Cryst.,* **1958**, *11*, 54-55.

6. Shannon, R. D., *Acta Cryst.,* **1976**, *A32*, 751-767.

7. Kendall, K. R., Thomas, J. K. and zur Loye, H. C., *Chem. Mater.,* **1995**, *7*, 50-57.

8. Kendall, K. R., Navas, C. and zur Loye, H.-C., *$Bi_2Sr_2M'_2M''O_{11.5}$ [(M' = Nb, Ta) and (M'' = Al, Ga)], Synthesis and Characterization of oxygen-deficient Aurivillius Phases*, G.-A. Nazri, J.-M. Tarascon and M. Armand, Eds., (MRS, Materials Research Society Symposium Proceedings: Solid State Ionics IV, Boston, MA, 1995), Vol. 369, pp. 355-360.

9. Goodenough, J. B., Ruiz-Diaz, J. E. and Zhen, Y. S., *Solid State Ionics,* **1990**, *44*, 21-31.

Chapter 6. Discussion

The previous chapter presented the data obtained for the doped Ruddlesden-Popper

phases examined in this study. These materials are intimately related to simple perovskites, and

specifically $La_{1-x}Sr_xMO_{3-\delta}$ (M= Ti, Co, Fe, Mn) compounds. In this chapter, we first discuss the

individual pieces of data, and then put them together to explain the structural and electrical

properties of the materials studied herein.

6.1. Synthesis and Structure

The synthesis of the modified Ruddlesden-Popper phases did not present many problems.

Standard solid state reaction methods in air were employed with success. Thus, grinding of the

starting metal oxides or carbonates and subsequent heating and mixing cycles were sufficient to

ensure that single-phase materials were obtained. As is shown in the XRD patterns, no second

phases were observed after the appropriate sequence of heating and grinding cycles.

All materials doped with fixed valent cations were brown in color, whereas transition

metal-doped materials were typically black. The difference in color is often taken as an indicator

of the increase in electronic conductivity in the materials upon substitution of transition metals

into the structure.

The structure of the Ruddlesden-Popper phases studied herein is made up of rock

salt-type sheets of SrO that separate two perovskite layers of general formula $SrMO_3$.[1] The

perovskite layers are made up of corner-shared MO_6 octahedra with the Sr atom sitting in a

12-coordinate site. Because of the difference in size between Sr^{2+} and the other cations,[2] it is

expected that the dopants will fully substitute exclusively in the Ti^{4+} site of the perovskite

structure. The structure of the parent phase, $Sr_3Ti_2O_7$, has been previously studied in detail.[3] It was reported that the octahedral site could be considered ideal, even though the cations were non-central, resulting in minor distortions. Other Ruddlesden-Popper phases in which two cations share the B-site have been reported. For example, $LaSr_2CuTiO_{6.5}$, another n = 2 material with ideal tetragonal symmetry and cell parameters a = 3.8816 Å and c = 20.296 Å, could be synthesized by standard solid state methods.[4] Surprisingly, no ordering in the B-site was observed, even though a large number of oxygen vacancies were present. One would expect the oxygen vacancies to concentrate on the coordination sphere of Cu^{2+}, a Jahn-Teller ion, but this was shown not to be the case. No electrical properties of this material were reported.

As was pointed out in Chapter 2, several $Sr_3Ti_2O_7$-type materials containing different cations in the B-site have been reported in the literature. Cations such as Co^{3+}, Fe^{3+}-Fe^{4+}, Mn^{4+}, Cu^{2+}, Cr^{4+}, Ir^{4+} and Ru^{4+}, besides Ti^{4+} and Zr^{4+},[5-10] may occupy the B site in the structure, attesting to the structural flexibility of the perovskite region. This feature should not come as a surprise, since the $SrMO_{3-\delta}$ oxides are also well known to accommodate a similar range of dopant cations.[11] Therefore, even though the number of layered perovskites studied does not compare with the number of perovskites, the ease in synthesizing novel phases based on the $Sr_3Ti_{2-x}M_xO_{7-\delta}$ solid solutions agrees with these studies. This characteristic also applies to a lesser degree to the fixed valent-doped materials. The maximum concentration of Al and Ga for which a single phase could be synthesized was about 1/8 or 12.5% in the B-site. Addition of greater concentrations resulted in formation of second phases.

It is of interest to realize that $Sr_3M_2O_6$ (M=Al, Ga) compounds do not have the layered perovskite structure, but a cubic structure with cell parameters a = 15.8440 Å and a = 16.095 Å.[12-14] In contrast, $Sr_3Co_2O_{6.06}$ and $Sr_3Fe_2O_6$ could be synthesized as a single phase with

the $Sr_3Ti_2O_7$ structure, as reported by Dann and Weller.[5, 6] At first, one would be tempted to reason that the difference lies in the cationic radii. However, the ionic radius for Ga^{3+} is 0.62 Å, whereas those of Co^{3+} and Fe^{3+} are 0.545 and 0.55 Å (low spin) or 0.61 and 0.645 Å (high spin), respectively. The answer may lie, instead, in the number of d electrons that both types of cations have. Whereas Co^{3+} has a d^6 valence shell configuration, the d orbitals in Ga^{3+} are full, so that the extra electrons provided must go into higher energy orbitals, thus destabilizing this cation in this particular structure.

The substitution of dopant cations for Ti^{4+} and Zr^{4+} in the structure results in the lowering of the cell parameters. This is due, in general, to the lower cationic radii of the dopants with respect to the host cations. The decrease in cell parameters was shown to be nearly linear in most cases, and suggests that the dopant cations indeed occupy the octahedral coordination. Regarding the fixed valent dopants, there is obviously no structural data available for the end members of the solid solutions, whereas the cell parameters obtained for our transition metal-doped compounds may be compared to those reported by other groups.

For example, $Sr_3Co_2O_{6.06}$ also has a tetragonal structure with cell parameters $a = 3.8321$ Å and $c = 20.0826$ Å. Extrapolating the data we obtained for our family of Co-doped materials, we get theoretical values of $a = 3.823$ Å and $c = 20.02$ Å (see Chapter 5). The difference in the values for the c parameters may be due, in part, to the quality of the fitted data. The other reason, which we believe is a more important factor, is due to the oxidation state of Co. The material reported by Dann and Weller may be characterized as a Co(III) compound, whereas our data is extrapolated from compounds which contain Co(IV) instead. This is supported by the nonstoichiometry data obtained by iodometric titration. On a quenched sample of composition $Sr_3Ti_{1.2}Co_{0.8}O_{7-\delta}$, the oxidation state of Co in air is 3.75. Other separate

173

measurements also confirm the predominance of Co(IV) in air on samples slowly cooled to room temperature. The oxidation state of the metal decreases with increasing temperature, which is consistent with observations in other oxides. Since Co(IV) is smaller than Co(III), we would expect our extrapolated XRD powder data to produce a theoretical end member of the solid solution with smaller cell parameters. We treat the significance of the predominance of Co(IV) in greater detail below.

Regarding the Fe-containing materials, the cell parameters reported for the $Sr_3Fe_2O_{7-\delta}$, $0<\delta<1$ series synthesized by Dann, Weller and Currie decrease linearly with increasing oxygen stoichiometry and iron oxidation state.[6] For $Sr_3Fe_2O_7$, the cell parameters given were $a = 3.853$ Å and $c = 20.151$ Å, which are close to our values of $a = 3.855$ Å and $c = 20.12$ Å. We should point out that the synthesis of this composition, as reported by these authors, requires high pressures of oxygen (500 atm). Our values for structural cell parameters suggest that the iron in our compounds is in a high oxidation state (Fe^{4+}). The confirmation of the presence of Co^{4+} also supports this conclusion, since this high oxidation state is commonly more stable in Fe than in Co.

Mizutani $et\ al.$ reported on the synthesis and XRD studies of $Sr_3Mn_2O_7$. The cell parameters obtained from their work were: $a = 3.801$ Å and $c = 20.06$ Å. These values also compare well with our cell parameters of $a = 3.804$ Å and $c = 20.10$ Å. Because the oxidation state of Co and Fe in the other doped Ruddlesden-Popper compounds is +4, we would also expect this to be the case for Mn, since the higher oxidation states are more stable in earlier transition metals.

The a parameter in the structure corresponds to the O-M-O distance in the MO_4 coordination sphere of the ab plane. It is not easy to draw conclusions from the a parameter in

the fixed valent-doped materials, given the lack of range of data points available to obtain metal-oxygen distances, such as Ga-O or Al-O, and compare them to other reported literature values. Also, the linearity of our data seems to deviate as we approach larger concentrations of dopant cations. However, the same is not true for the transition metal-doped materials. Both $SrFeO_3$ and $SrCoO_3$, with the cubic perovskite structure, have been synthesized previously.[15, 16] In the case of iron, the cell parameter and Fe-O distance are exactly the same as in our case (3.855 Å and 1.9275 Å, respectively). For the Co compound, the authors report a cell parameter of 3.835 Å, slightly larger than our extrapolated value of 3.823 Å. Their value has been confirmed by other independent studies[17, 18] and results in a Co-O distance of 1.9175 Å and a cationic radius of 0.517 Å for Co(IV) in the octahedral coordination of the perovskite structure, which may be compared to the distance Co-O = 1.9115 Å and a cationic radius of 0.512 Å in the Ruddlesden-Popper structure from our results. Furthermore, Greenblatt and coworkers reported on a series of chemically oxidized perovskite cobaltates, $La_{1-x}Sr_xCoO_{3-\delta}$, and listed the Co-O distance as 1.912 Å for x=0.9 with almost 70% Co(IV) in the structure. These values are not significantly different and serve as an independent confirmation that our compounds contain predominantly Co(IV). Shannon gives the cationic radius for Co(IV) as 0.53 Å in its high spin configuration, whereas the cobalt ion was reported to adopt a low spin configuration in $SrCoO_3$ ($t_{2g}^5 e_g^0$). In contrast, structural studies in the family of cubic perovskites $SrCo_{1-x}Ti_xO_{3-\delta}$ reported by Kharton *et al.* gives an average Co-O distance of 0.547 Å, which strongly indicates the presence of low spin Co^{3+}.[19, 20]

The predominance of the Co(IV) ion deserves special mention here. Materials which exhibit an average oxidation state of +4 for Co are not very common in the literature. Some examples are: $SrCoO_3$[16-18, 21] and $BaCoO_3$,[22] both of which are perovskite materials, Ba_2CoO_4 (a

175

layered perovskite)[23], Li_8CoO_6,[24] Cs_2CoO_3[25] and $K_6Co_2O_7$.[26] The most common synthetic

method to achieve high oxidation states is through the use of high oxygen pressures. Taguchi and

coworkers, for example, demonstrated the dependence of nonstoichiometry on oxygen partial

pressures and synthesis temperatures on $SrCoO_{3-\delta}$ samples.[17] Yet another approach was

demonstrated by Hagenmuller and coworkers;[16] they synthesized stoichiometric $SrCoO_3$ by

electrochemical oxidation of the oxygen-deficient brownmillerite (a perovskite with ordered

oxygen vacancies) with composition $SrCoO_{2.5}$ in alkaline media (1 M KOH) at room

temperature. Similarly, Greenblatt and coworkers have also been able to achieve an increase in

the oxidation state of Co in $La_{1-x}Sr_xCoO_{3-\delta}$ upon chemical oxidation at room temperature by

stirring in a 5 M NaOH solution to which Br_2 was added.[27] Using this method, a maximum of

70% Co (for x=0.9) was identified as Co(IV) by iodometric titration measurements. A lower

average oxidation state of Co (between 3 and 4) has been observed for a variety of compounds.

For example, $La_{1-x}Sr_xCoO_{3-\delta}$, attains a maximum oxidation state of 3.4 with x=0.4.[28, 29] As

mentioned above, $SrCoO_{3-\delta}$ can also be made to achieve a desired level of nonstoichiometry.

For the reasons previously mentioned, it is surprising that we obtained a Co-containing

compound where the oxidation state of the metal is +4. Our synthetic technique was not geared

towards obtaining a higher oxidation state, but rather to reproduce previous work (both on

$Sr_3Ti_2O_7$ and $Sr_3Co_2O_{7-\delta}$) with the aim of producing new phases containing Co^{3+}. In this manner,

we hoped to come up with nonstoichiometric materials with a varying range of oxygen vacancies

according to the dopant concentration used. Even though the perovskite structure has been shown

to accommodate transition metals with high oxidation states (such as Fe and Co),[18] the reported

synthesis of these materials was intended to produce these highly oxidized materials. That our

synthesis in air produced Co(IV) compounds at reduced temperatures starting from a mixed valent Co compound (Co_3O_4) is something for which we have no explanation.

We should also point out that Fe(IV) compounds are not very common either, although more examples are known than for Co, as would be expected. As an example, the $SrFeO_{3-\delta}$[15] and the $La_{1-x}Sr_xFeO_{3-\delta}$[30] systems have also been studied. Electrochemical methods have also been used to synthesize $SrFeO_3$ from $Sr_2Fe_2O_5$.[31] Likewise, the Mn analogs are well known.[32-34]

Since we would expect the earlier transition metal to achieve a higher oxidation state (e.g. Mn vs. Co), and we determined that Co was in the oxidation state of +4, we assume that both the Fe and Mn-containing materials also contain the transition metal in its oxidation state of +4. Furthermore, we measured the nonstoichiometry of the cobalt-containing compound with the highest dopant concentration. The results imply that the Co-doped compounds with a lower dopant concentration also contain the +4 oxidation state.

6.2. Nonstoichiometry

The main driving force behind the research presented in this thesis was to obtain novel oxygen-deficient phases. Since the concentration of oxygen vacancies is an important parameter in effecting oxygen ion conductivity, substitution of aliovalent dopant cations in the Ti^{4+} site were carried out in order to achieve various degrees of nonstoichiometry in the oxygen sublattice. Several other groups have used this approach on other perovskite-type materials (see several examples provided in Chapter 2).

The concentration of oxygen vacancies may be fixed by doping with fixed valent cations such as Al^{3+} and Ga^{3+}. About 1/8 of the Ti sites could be substituted by these cations, corresponding to a maximum concentration of oxygen vacancies equal to 1.8% of all oxygen

sites. As predicted in Chapter 3, and based on our conductivity results, the nominal level of nonstoichiometry is assumed to be maintained in the range of oxygen partial pressure used for the conductivity measurements.

In contrast, the transition metal-doped Ruddlesden-Popper phases display a range of nonstoichiometries due to the ability of elements such as Co, Fe and Mn to change valence with changing conditions of temperature and oxygen partial pressure. Iodometric titrations carried out on slowly cooled samples in air reveal that the Co is in the +4 oxidation state. This result implies that the concentration of oxygen vacancies is minimal. However, at 700 °C, oxygen vacancies are introduced into the structure via reduction of the transition metal down to an average oxidation state of 3.75. As the oxygen pressure is lowered, the oxidation state of Co decreases according to a slope of 1/6, as shown in Figure 5.25. The maximum measured concentration of oxygen vacancies is about 3.5% of all oxygen sites.

Dann and Weller reported a series of materials $Sr_3Co_2O_{7-\delta}$ with a range of stoichiometries $0.94 \leq \delta \leq 1.22$. Those values translate into a maximum of 17% of all oxygen sites vacant. That the tetragonal structure of the parent Ruddlesden-Popper phase is maintained with such a high level of oxygen vacancies is a testament to the flexibility and stability of the perovskite block within the structure. The iron analog, $Sr_3Fe_2O_{7-\delta}$, also displays a range of oxygen nonstoichiometries, $0 \leq \delta \leq 1.0$. Similarly, removal of oxygen from the same site results in a square-pyramidal coordination around the Fe atom. However, there are other systems that also tolerate high levels of oxygen deficiency, such as the layered cuprates. For example, Kinoshita *et al*. reported on the structure and superconducting properties of $La_{1.82}Ca_{1.18}Cu_2O_{6\pm\delta}$ (with $\delta \approx 0.01$), also a system derived from the $A_3B_2O_{7-\delta}$-type structure.[35]

Given the literature reports on transition metal containing Ruddlesden-Popper phases, we expected to synthesize and obtain solid solutions of general composition $Sr_3Ti_{2-x}M_xO_{7-\delta}$, (M=Co, Fe, Mn) where the transition metal would be in the +3 oxidation state and thus obtain large concentrations of oxygen vacancies. For instance, with all Co(III), a composition such as $Sr_3TiCoO_{6.5}$ would be possible, similar to the reported phase $Sr_2LaTiCuO_{6.5}$.[4] Furthermore, since the synthesis conditions were shown to determine the oxidation state in the iron compound, we could also use a similar approach as a tool for controlling the electrical properties (e.g. ionic and electronic conduction) in the $Sr_3Ti_{2-x}Fe_xO_{7-\delta}$ solid solution. However, our results are surprising in that our synthetic procedure (standard solid state reaction in ambient air) resulted in highly oxidized materials.

6.3. Electrical Conductivity

The electrical conductivity data was obtained from 2-probe AC impedance spectroscopy. The method has already been discussed in Chapter 4. Because, in general, only one arc was evident in our experiments, fitting this arc to its x-axis intercept produced the total (i.e. bulk plus grain boundary) conductivity of the material. The capacitance of this arc was typically around 10^{-11} Farads, suggesting that it was due to bulk transport. Interfacial processes typically display capacitances around 10^{-9} Farads.

6.3.1. Doping with fixed valent cations

Measurements of the electrical conductivity as a function of temperature in air reveal an increase in the magnitude of the conductivity with respect to the parent, stoichiometric phase, $Sr_3Ti_2O_7$ (Figure 5.9). However, in general, the increase in magnitude was relatively small, the

maximum being about 1 order of magnitude. The slope of the lines and, therefore, the activation

energies for all fixed-valent compounds, are very similar (Table 5.6). This feature suggests a

similar conduction mechanism taking place in this family of materials. The only other study we

are aware of is that of Steele and coworkers, who reported the synthesis and conductivity of a

number of oxide materials, among them $Sr_3Ti_{1.9}M_{0.1}O_{7-\delta}$, M=Al, Mg.[36] Conductivity values

measured in air were 1×10^{-5} S/cm and 4.2×10^{-7} S/cm for the Al and Mg-doped compounds,

respectively, at 500 °C, and the activation energies were about 1 eV for both materials. They

compare these compositions to the pure perovskite $SrTiO_3$ and attribute the increase in

conductivity to the increase in oxygen vacancy concentration, thus characterizing it as ionic in

nature. Our results indicate that the conductivity of $Sr_3Ti_2O_7$ at 500 °C is about 5×10^{-6} S/cm;

our activation energies for the parent phase, as well as for the doped compounds, show good

agreement with their results. To our knowledge, their report is the only attempt at characterizing

the electrical properties of $Sr_3Ti_2O_7$-doped compounds.

All materials studied exhibited a hysteresis in the heating vs. the cooling cycles. This

behavior has been observed in other compounds, such as $Ba_2In_2O_5$ and some Aurivillius phases

previously studied in the zur Loye group.[37, 38] It is usually ascribed to an order-disorder

transition, whereby the oxygens in the anionic sublattice become increasingly disordered with

increasing temperature and stay disordered when the material is cooled due to a kinetic effect.

It is clear that there is not a strong dependence of the total conductivity on the dopant

concentration from the measurements in air. As can be seen in Figure 5.9, the values of the

conductivity for $Sr_3Ti_{1.8}Ga_{0.2}O_{6.9}$ and $Sr_3Ti_{1.75}Ga_{0.25}O_{6.875}$ are not very different, although they

are larger for the more highly doped sample.

The lack of a strong effect in the conductivity in air upon doping of these materials may be due to one of two factors. If the increase observed were due to ionic conductivity alone, we would expect the introduction of such high dopant concentrations to have a larger effect due to the creation of oxygen vacancies, unless the parent phase itself already presents a significant degree of disorder in its oxygen sublattice. This type of intrinsic Frenkel disorder is considered to be critical, for example, in the ionic conductivity displayed by the pyrochlore materials studied in the Tuller group.[39-41] The introduction of dopants would have a smaller impact on the total concentration of oxygen vacancies, thus accounting for the small increases in conductivity. However, there are no reports in the literature of such a high degree of disorder in stoichiometric perovskite materials such as $Sr_3Ti_2O_7$ or the more studied $SrTiO_3$. On the contrary, a detailed structural study of the $(Ca, Sr)_3Ti_2O_7$ system by Hawkins and White using high resolution electron microscopy, revealed no disorder in the oxygen sublattice to form such kinds of superstructures.[42] The other explanation, which we later prove to be the case, invokes the increase in conductivity being due to electronic charge carriers.

We also studied a system of doped zirconates, of general formula $Sr_3Zr_{1.9}M_{0.1}O_{6.95}$, M=Al, Ga. In this case, the conductivity of the doped materials also increased by about an order of magnitude with respect to the parent phase. However, the magnitudes of the total conductivity are significantly lower than in the titanate system. Unlike the $Gd_2(Ti, Zr)_2O_7$ system, where an increase in Zr concentration was accompanied by an increase in disorder within the oxygen sublattice, we did not observe any such phenomena. We point out that the pyrochlore structure is oxygen-deficient in nature, since 7 out of 8 crystallographic oxygen sites are statistically occupied, whereas the layered perovskite structure that forms the basis of our studies exhibits no such oxygen deficiency in its anionic sublattice.

Introduction of large cations has been suggested to improve oxygen ion conductivity.[43] Instead, the zirconate materials we have studied show a disappointingly low magnitude of total conductivity. As we see below, the conductivity of the titanate materials in air is due to electronic charge carriers, and we have no reason to believe that it is any different in the zirconates. Because of these reasons, we did not study these materials any further, and concentrated on the titanate-based series.

As explained above, our preliminary conductivity data in air seems to indicate that the nature of the conduction process is electronic, rather than ionic, in nature. In chapter 3, we outlined existing defect models that may be used to deconvolute the various components of the electrical conductivity. These models are based on the effect of the surrounding atmospheric conditions (temperature and oxygen partial pressure) on the concentrations of the various defects in the structure. Consequently, conductivity data as a function of oxygen partial pressure were collected for a large number of samples.

Figure 5.11 shows the plot of log σ vs. log $p(O_2)$ at 700 °C for some Al and Ga-doped materials. Three different, distinct regions are observed. If we compare this profile with that predicted by the defect model (Figure 3.2), we can easily assign each of these regions to a particular regime, each dominated by a specific charge carrier. The first region can then be assigned to p-type conductivity, which agrees with our previous results in air. The second, $p(O_2)$-independent region is assigned to ionic conductivity and the last region is due to n-type conductivity.

The electrolytic regime exhibits, in general, low ionic conductivities when compared to other known electrolytes. Our results indicate that ionic conductivities for the Ga-doped materials are about 10^{-6} S/cm at 700 °C, about 3 orders of magnitude lower than that of YSZ at that

temperature. Furthermore, we see that the ionic conductivities are somewhat higher for the Ga-doped than the Al-doped materials. On the other hand, regarding the Ga-doped materials, due to the scatter in the data, there is no clear dependence of the magnitude of the conductivity on the dopant concentration in the electrolytic regime. The largest ionic conductivity is observed for the compound with the lowest dopant concentration. The activation energy appears to show an increase with dopant concentration, though the trend is not completely clear, and in going from Ga to Al. Due to this trend in the activation energy, we believe that the scatter in the conductivity data may hide a trend of decreasing ionic conductivity with increasing dopant concentration. This trend is similar to that observed in the case of yttria-stabilized ceria.[44] With increasing addition of Y^{3+}, the conductivity increases while the activation energy decreases. This trend continues up to a concentration of 8%mol Y_2O_3, whereupon the magnitude of the ionic conductivity reaches a maximum value and then decreases while the activation energy increases. This effect is due to the association of vacancies with the dopants, resulting in an additional energy required for ionic motion. The same effect could be responsible for the trend observed in our Ga-doped samples. Further pointing to this explanation is the fact that the highest conductivity is observed for the lowest dopant concentration. Thus, the conductivity goes through a maximum at very low doping levels and what we observe is the downturn in conductivity accompanied by the increase in activation energy with increasing Ga concentration.

Data of conductivity as a function of oxygen partial pressure for various fixed valent-doped compounds at temperatures between 600-1000 °C are shown in Figures 5.11-5.17. At higher temperatures, the n-type domain at low $p(O_2)$'s becomes more clearly visible, and displays a slope of $-1/4$, which further confirms our hypothesis about this region. Using equation 3.26, the data points could be fitted in a satisfactory manner, as shown by the superimposed

curves, confirming the identification of the three distinct regimes. The fit at low $p(O_2)$ was not as good because of the fewer number of points available.

Using the defect model outlined in Chapter 3 and fitting the conductivity data accordingly yields values for the oxidation and reduction enthalpies, as well as the thermal bandgap (Table 5.7). Similar values for other titanate materials, such as $SrTiO_3$ and $Gd_2(Ti, Zr)_2O_7$, are also available in the literature.[45, 46] Moon studied the pyrochlore system and calculated the reduction enthalpy to be increasing from 4.8 to 7.2 eV with increasing Zr concentration. This phenomenon was ascribed to the fact that it is harder to reduce Zr^{4+} than Ti^{4+}. Bandgap energies were in the 3.9-4.6 eV range. Choi and Tuller reported oxidation and reduction enthalpies of 1.30 and 5.2 eV, respectively, for $SrTiO_3$. The bandgap energy in this material was calculated to be 3.35 eV. We point out that in both of these systems, Ti^{4+} is in an octahedral coordination surrounded by six oxygens. While the data obtained for the doped Ruddlesden-Popper phases is somewhat scattered, our values are reasonable in light of the other related systems. This agreement supports validity of our data.

The difference in the magnitudes of the conductivities between Ga and Al-doped materials may be due to the closer ionic radius of Ga^{3+} to that of Ti^{4+}, when compared to Al^{3+}. Substitution of a cation with a lower valence than that of the host cation introduces oxygen vacancies. The closer the guest cation is to the host in size, the less "disturbed" the structure will be, and the weaker is the association between dopants and oxygen vacancies. For example, this effect has been observed in CeO_2-based systems.[47] Furthermore, the structure contracts more with a smaller dopant cation, as evidenced by the decrease in cell parameters, which may lead to an increased strain for oxygen ion migration.

The substitution of fixed valent dopant cations such as Al^{3+} or Ga^{3+} for Ti^{4+} did not lead to a great improvement of the electrical properties. An ionic domain is observed at intermediate oxygen partial pressures, characterized by low conductivities and relatively high activation energies when compared to other ionic conductors (e.g. for YSZ, $E_a = 0.8$ eV).[48] The best oxide ion conductor is $Sr_3Ti_{1.98}Ga_{0.02}O_{6.99}$, which displays an ionic conductivity of 2×10^{-4} S/cm at 1000 °C and an activation energy of 1.23 eV. In air, the conductivity is predominantly p-type, whereas at very low $p(O_2)$, n-type can be observed in these compounds.

Although the introduction of aliovalent dopants increased the nominal concentration of oxygen vacancies, we suspect that the concentration of mobile ionic species is somewhat lower. The difference between the heating and cooling cycles shown in Figure 5.8 leads us to believe that there is a certain degree of ordering in the structure, presumably in the oxygen sublattice. Dopant-vacancy associations are also known (see e.g. Chapter 2, in reference to YSZ) which result in a decrease of the concentration of mobile oxygen vacancies. These associations may also be responsible, in part, for the low levels of ionic conduction. Furthermore, because of the two-dimensional structure, anisotropic effects are probably an important reason why these materials do not exhibit good levels of oxygen ion conductivity. The conductivity is expected to be higher in the *ab* plane than in the *c* direction due to the SrO rock-salt layer which separates the perovskite layers.

The small increase in the hole conductivity in air may also be explained by the defect association invoked above. Through equations 3.18 and 3.19, an increase in the concentration of oxygen vacancies by a factor of 100 is accompanied by a concomitant increase in the concentration of holes by a factor of 10. Since the increase in ionic conductivity leads us to

believe that defect association plays an important role in these materials, the increase in concentration of mobile oxygen vacancies is less than expected, and so is that of holes.

Our discussion so far has centered on the effect that doping with cations with a fixed valence, such as Al^{3+} or Ga^{3+}, in place of Ti^{4+}, has on the electrical properties. We now turn our attention to the electrical properties of Ruddlesden-Popper phases which contain a transition metal in the B site of the perovskite structure.

6.3.2. Doping with transition metal cations

6.3.2.1. Solid solutions with Co

The dependence of the conductivity in air for $Sr_3Ti_{1.8}Co_{0.2}O_{7-\delta}$ is shown in Figure 5.9, compared to other Ruddlesden-Popper materials doped with other fixed valent cations. The two major differences are the magnitude of the total conductivity (higher in the Co-doped sample) and the activation energy (lower in the Co-doped sample). Comparing the Ga and Co-containing systems, the host material and the dopant concentration employed are the same, the only difference being the identity of the dopant cation. The introduction of Co is expected to lead to an increase in the electronic conductivity, given the presence of d electrons. Hence, it is unlikely that the measured improvement in electrical properties (increase in conductivity and decrease in activation energy) in the Co-doped system is due to ionic conductivity. This hypothesis is discussed below.

As laid out in Chapter 3, it is useful to study the conductivity of the transition metal-doped materials as a function of oxygen partial pressure. These measurements at various temperatures are shown in Figure 5.19 for $Sr_3Ti_{1.8}Co_{0.2}O_{7-\delta}$. To deconvolute the data and extract the different components, we make use of Figure 3.3 and equation 3.36. The fits of the model to

the data in the figure are shown as superimposed lines. The regime at high $p(O_2)$'s is clearly due

to p-type conductivity, though the assignment of the $p(O_2)$-independent regime is not as clear-cut.

If the p-type regime corresponds to region I, then the plateau region that follows is also due to

p-type conduction. The low activation energy obtained in this regime (0.64 eV) relative to that of

the Ga-doped system seems to support this conclusion. The other possibility corresponds to the

case where the p-type regime at high $p(O_2)$ is assigned to region III; in that case, the following

regime would correspond to ionic conductivity, since the oxygen vacancies are the only

charge-carrying defects which show no dependence on $p(O_2)$ in region IV.

The electroneutrality equation in regions III and IV is $2[V_o^{\cdot\cdot}] = [N_{Ti}^{'}]$. On closer inspection,

we observe that the transition between regions III and IV is accompanied by a 1-electron

reduction and consequent change in the dopant valence. Hence, the total concentration of the

transition metal dopant is defined in region III as $N_{Ti}^{x} = N_{tot}$ and changes in region IV

to $N_{Ti}^{'} = N_{tot}$. This reduction process may be monitored through the use of iodometric titration.

The results shown in Figure 5.25 for $Sr_3Ti_{1.2}Co_{0.8}O_{7-\delta}$ reveal a decrease of the average

oxidation state of Co from +4 to +3 with decreasing $p(O_2)$. On a log scale, the slope of the line is

about 1/6, which corresponds to that observed in the conductivity dependence on $p(O_2)$. This

result implies that the transition observed in the conductivity corresponds to regions III and IV,

and therefore from p-type to ionic conduction. Consequently, the activation energy observed in

this regime (0.64 eV for $Sr_3Ti_{1.2}Co_{0.8}O_{7-\delta}$) corresponds to the activation energy for ionic motion.

Our value for the activation energy for the ionic conductivity is comparable to that of YSZ (0.8

eV) or other perovskite-related materials such as $SrFeCo_{0.5}O_x$ (0.63 eV), and the ranges found in

$La_{1-x}Sr_xCoO_{3-\delta}$ (from 1.7 eV for x=0.2 to 0.84 eV for x=0.6).[49]

The wide ranges in activation energies for oxygen ion migration in perovskite-related materials is known; from the relatively high values reported for $La_{0.8}Sr_{0.2}CoO_{3-\delta}$ to those found in $CaCe_{0.8}M_{0.1}O_{3-\delta}$, M=Gd, Er (0.36 and 0.54 eV, respectively).[50] We have found in our studies that for three compounds with similar composition, e.g. $Sr_3Ti_{1.8}M_{0.2}O_{7-\delta}$, M=Ga, Al, Co, the activation energies range from 1.59 and 1.47 eV for M=Al and Ga, respectively, to 0.64 eV for M=Co. Furthermore, in the regime at which the activation energies are measured, all dopant cations are in the oxidation state of +3. Since the concentration of oxygen vacancies is, therefore, nominally equal, the implication is that the mobility of the oxygen anion is substantially different in both cases.

Assuming that the identity of the cation has little or no influence on the presence of ordered vacancies, the possible explanation lies in the bonding energy between the cation and oxygen in the lattice. The M-O bond has to be broken before the O^{2-} ion can hop to another vacant site. The stronger the bond between them, the higher the energy needed for breaking the bond. In our specific case, the difference is between the Ga-O and Co-O bond energies. We would expect Ga^{3+} to have a higher electronegativity, thereby making the bond more covalent than with Co^{3+}, and resulting in a higher energy for the O^{2-} to break the bond and move. To support this idea, we can look at the cell parameters to get an idea of bond distances, which serve as a measure of the M-O bond energy. The cell parameters for the materials in air are virtually identical; however, we should take into account that these bond distances are between Ga^{3+}-O^{2-} and Co^{4+}-O^{2-}, since in this regime Co is still very highly oxidized, and is not in the +3 oxidation state yet. Therefore, it is expected that at lower $p(O_2)$ the Co^{3+}-O^{2-} bond distance would significantly increase, purely based on electrostatic arguments, since the bonding in the

perovskite structure is generally considered to be ionic. This argument may explain in part why the activation energy in the Ga-doped compound is higher than in the Co-doped compound.

The data fit shown in Figure 5.19 may be used to extract the energy required to ionize Co^{4+} to Co^{3+}, E_{Co}, as outlined in Chapter 3. We showed in Chapter 5 that $E_{Co} = 3.61$ eV. Our calculated value assumes that E_g and E_{ox} in the Co-containing material are similar to those in the fixed valent-doped phases, and those values were used to calculate E_{Co}. We already discussed sources of error for E_g and E_{ox}, which will influence the calculated value of E_{Co}. Since the bandgap energy is about 3.6 eV as well, this result seems to indicate that the Co^{4+} level lies just above the top of the valence band.

In order to confirm the presence of the electrolytic regime at intermediate partial pressures of oxygen, we attempted to carry out concentration cell (EMF) measurements. However, we were not successful in obtaining ionic transference numbers.

The behavior of the sample during the concentration cell measurements may be attributed to one of two reasons. If our previous hypothesis is wrong and for some reason the $p(O_2)$-independent regime is due to electronic instead of ionic conductivity, then no voltage should develop across the cell because of shorting through the electronic conductor. However, this hypothesis does not explain why we observed a voltage developing a few minutes after changing the gas mixture. Another explanation invokes the presence of a very small leak in the seal, so that we do not have a true seal. If this is the case, the voltage increases due to the imposition of the oxygen potential through the ionic conductor. Due to oxygen leakage across the cell, the voltage does not to reach the value given by the Nernst equation and then decreases with time. The main point is that, even though we could not directly measure ionic transference

numbers, we did observe some indication that the migration of oxygen ions makes a contribution to the overall transport process in the material.

In order to obtain an additional, indirect measure of the ionic conductivity, we carried out measurements of the chemical diffusion coefficient of the material. In Chapter 3, we laid out how these data could be used to determine the presence of ionic conductivity. If we assume that the chemical diffusion coefficient (6.8×10^{-6} cm^2sec^{-1} at 700 °C) is equal to the diffusion coefficient of oxygen ions, we obtain a value for the ionic conductivity (0.03 S/cm) which is about an order of magnitude higher than that measured using the AC impedance method.

The above calculation assumes that the concentration of oxygen vacancies is equal to the concentration of mobile ionic charge carriers. This is true if there is no vacancy-dopant association and the oxygen vacancies are disordered. Otherwise, the true mobile oxygen vacancy concentration will be less than that given by the nonstoichiometry data and the conductivity will also be smaller. Examples of ordering of oxygen vacancies in perovskite-related structures are known.[11]

Another possible source of error involves the diffusion length. The assumption made in the derivation of the chemical diffusion coefficient in Chapter 3 is that the diffusion length is one half the shortest dimension of the sample, implying that the sample is fully dense. Introduction of pores results in a decrease of the diffusion length, which is related to the chemical diffusion coefficient by

$$x = \sqrt{\tilde{D}t} \qquad (6.1)$$

where x represents the diffusion length and t is time. We note that a decrease by an order of magnitude in x results in a decrease of two orders of magnitude in the chemical diffusion coefficient.

A number of factors should be considered regarding the diffusion coefficient of oxygen ions. The quantity directly measured through our measurements is the chemical diffusion coefficient of the material as a whole. We recall that, if we assume that holes and oxygen ions are the primary conducting species, which we infer from the region at high $p(O_2)$ in Figures 5.19 and 5.20 and the defect theory derived in Chapter 3, then the chemical diffusion coefficient can be expressed as:

$$\tilde{D} = t_e\, D_i + t_i\, D_e \tag{6.2}$$

i.e. a combination of the transport processes of holes and oxygen ions. If one of them is sufficiently slower than the other, then the slower species will be limiting the diffusion process for the whole material and will be the one whose coefficient is represented. Since the gas is changed from air to 0.1% O_2/Ar, we are in the regime dominated by p-type conductivity. If we make the assumption that $t_e \gg t_i$, equation 6.2 reduces to:

$$\tilde{D} = D_i \tag{6.3}$$

We now have to ask ourselves whether the above assumptions are correct or not. If the plateau is due to ionic conductivity, the answer is probably no. The electrolytic regime starts at about 10^{-5} atm; if we take this point as the boundary between regions III and IV, the vacancies show a $-1/6$ dependence with respect to log $p(O_2)$ in region III, so that we can estimate the ionic and electronic conductivities under 0.1% O_2/Ar (10^{-3} atm). Assuming, in the worst-case scenario, that at 10^{-5} atm the value of the conductivity is taken as the starting point for both conductivities, a

quick calculation reveals that at 10^{-3} atm, the ionic transference number is about 0.2. This results means that our measured chemical diffusion coefficient is largely due to the diffusion of oxygen ions, albeit with a significant contribution from the diffusion of holes. This explains why our calculated ionic conductivities are too high; the chemical diffusion coefficient of oxygen ions is somewhat lower than the chemical diffusion coefficient of the material as a whole under our conditions of temperature and oxygen partial pressures. These deviations also help explain in part the difference in activation energies observed between those obtained from the temperature dependence of the chemical diffusion coefficient and the electrical conductivity.

If the plateau at intermediate $p(O_2)$ is due to electronic conductivity, then the assumption that $t_e \gg t_i$ is true and equation 6.3 remains valid. In this case, the only way to explain the large value of the calculated ionic conductivity is to invoke a very large degree of vacancy-dopant association, which would decrease the number of charge carriers, and consequently the ionic conductivity, by orders of magnitude in the range of our measurements.

Assuming that the plateau regime corresponds to ionic conductivity, the chemical diffusion coefficient of oxygen ions may be calculated to be about 6.4×10^{-7} cm^{2}sec^{-1} at 700 °C, or about an order of magnitude lower than what we measured experimentally for $Sr_3Ti_{1.6}Co_{0.4}O_{7-\delta}$. This calculated value may be compared to those of related perovskite materials. For example, the chemical diffusion coefficients of the $La_{1-x}Sr_xBO_{3-\delta}$ (B=Co, Fe, Mn, Cr) system have been reported in the literature.[34, 51-53] Typical values for the diffusion coefficients are in the order of 10^{-6} cm^{2}sec^{-1} with, in general, very little dependence on the identity of the transition metal. These values can be considered to be in the same ballpark figure as our Co-containing materials. Assuming that the chemical diffusion coefficient of oxygen is 6.4×10^{-7} cm^{2}sec^{-1} at 700 °C and taking $t_e = 0.9$, D_e may be calculated to be 6.224×10^{-5} cm^{2}sec^{-1} at 700 °C.

The chemical diffusion coefficient of Fe-doped $SrTiO_3$ has also been investigated by Maier and coworkers and calculated to be about 5×10^{-5} cm^2sec^{-1} at about 700 °C.[54-56] That constitutes a difference of about 2 orders of magnitude with respect to our calculated value in the Co-containing system. The defect structure of the material is obviously an important factor in the chemical diffusion coefficient and may explain the difference in the above values. Another reason behind this difference may lie behind the dimensionality of the two structures. While $SrTiO_3$ is a 3-dimensional structure, the Ruddlesden-Popper structure contains a layer of SrO rock salt-type layer which probably impedes conduction along the c axis. Hence, anisotropic effects are likely to be important in the layered perovskites.

6.3.2.2. Solid solutions with Fe

The Fe-doped compound shows a similar profile to that shown by the Co-doped series. The width of the $p(O_2)$-independent regime decreases with increasing dopant concentration. However, the total magnitude of the conductivity does not increase with increasing x. By comparison with the Co-doped system and using Figure 3.3, we can assign the high $p(O_2)$ regime to p-type conductivity. It is reasonable to assume that Fe^{4+} is being reduced as the oxygen partial pressure is being decreased, making the $p(O_2)$-independent regime ionic in nature, by analogy to the Co-containing system. The identification of an ionic regime in the $MTi_{1-x}Fe_xO_{3-\delta}$ (M=Ca, Sr) system at intermediate $p(O_2)$'s has been reported in the literature.[57, 58] The explanation given by the authors is similar to what we have previously described based on simple defect models that take into account reduction of Fe^{4+} to Fe^{3+}. Furthermore, their data fits their model quite well even for x=0.8, implying that defect band formation is not an important factor in explaining the conductivity dependence.

193

It is also of interest to note that as the dopant concentration is increased, the $p(O_2)$ at which we start observing decomposition increases. This is clearly the trend in the Fe-doped system, and in general also holds true for the Co-doped system, although for x=0.6 and x=0.8 the trend seems to be reversed. This effect may be due to a continued reduction process. Even though our defect model (Figure 3.3) predicts that region IV is dominated by the presence of the transition metal in its 3+ oxidation state (i.e. $N'_{Ti} = N_{tot}$), it only means that this oxidation state predominates, not that it is the only oxidation state present. As $p(O_2)$ is further decreased, the reduction continues, and therefore the average oxidation state of Co is decreasing. Presumably, at some point, enough Co^{2+} is produced to cause Co to become unstable in the structure and come out of solution, causing the partial decomposition that we observe in XRD after measurements at reduced oxygen partial pressure.

6.3.2.3. Solid solutions with Mn

We have seen that the conductivities of solid solutions of Ruddlesden-Popper phases containing Fe and Co present similar profiles in their dependence with oxygen partial pressure. The Mn-containing phases present a significantly different profile, as shown in Figure 5.24. In light of the other systems studied up to now, the maximum in conductivity at 10^{-5}-10^{-8} atm is surprising. This type of profile, while not common, has been observed before in ZrO_2-CeO_2-Y_2O_3 solid solutions by Cales and Baumard,[59, 60] and in Mn-doped $Gd_2Ti_2O_7$.[61] The latter study took into account the formation of a defect band, namely that of the Mn d orbitals, so that the total conductivity could be modeled as:

$$\sigma_{tot} = 2[V_o^{\cdot\cdot}]q\mu_{V_o^{\cdot\cdot}} + nq\mu_e + pq\mu_h + \frac{[Mn'_{Ti}]\cdot[Mn^x_{Ti}]}{[Mn_{Ti}]_{tot}}q\mu_{e(Mn)} \qquad (6.4)$$

accounting for ionic conductivity, electron and hole conductivity in the conduction and valence

bands, respectively, and electron conductivity in the Mn band, assumed to be of the hopping type.

This situation is schematically shown in Figure 6.1, where the quantity c(1-c) represents the

concentration of electronic charge carriers [e.g. $c = \dfrac{[Mn_{Ti}^{'}]}{[Mn_{Ti}]_{tot}}$.; $1-c = \dfrac{[Mn_{Ti}^{x}]}{[Mn_{Ti}]_{tot}}$]. In equation 6.4,

the term $\mu_{e(Mn)}$, as is typically defined, contains the term (1-c), i.e.[62]

$$\mu = \frac{(1-c)ea^2 v_o}{kT} \exp(^{-E_H}\!/_{kT}) \qquad (6.5)$$

where e is the electronic charge, a is the lattice parameter, v_o is the attempt frequency and E_H is

the activation energy for hopping. We redefine the mobility without the (1-c) term, since it is

already included in equation 6.4. It should be noted that this electronic conductivity reaches a

maximum at the point at which $[Mn_{Ti}^{'}] = [Mn_{Ti}^{x}]$ or, in other words, when the average oxidation

state of Mn is 3.5.[61] At this point the term $\dfrac{[Mn_{Ti}^{'}] \cdot [Mn_{Ti}^{x}]}{[Mn_{Ti}]_{tot}}$ reaches its maximum. Since the

concentrations of Mn^{3+} and Mn^{4+} are equal to $A \cdot p(O_2)^{-1/6}$ and $B \cdot p(O_2)^{1/6}$, it is possible to model

the conductivity as a function of $p(O_2)$ and extract the mobility of the electrons in the Mn

conduction band.

The study of the $(ZrO_2\text{-}CeO_2)_{0.9}\text{-}(Y_2O_3)_{0.1}$ system also showed the presence of an ionic

plateau at high oxygen partial pressures, the width of which decreased with increasing

concentration of Ce and increasing temperature. Furthermore, with increasing Ce content, the

researchers also observed a slight increase in conductivity as $p(O_2)$ was decreased, the rate of

increase becoming larger for higher Ce content. This behavior is similar to what we observed in

our Mn-doped Ruddlesden-Popper phases. Their explanation can also be derived from equation

6.4, taking into account that Y_2O_3-doped ZrO_2 operates, in general, in an electrolytic regime. With increasing Ce content, a defect band forms, accounting for the electronic conductivity, the magnitude of which is dependent on the Ce^{3+}-Ce^{4+} equilibrium content. Therefore, the total conductivity shows a slight increase, as given by the sum of both the ionic component and the electronic component from the Ce band. The magnitude of the ionic conductivity was taken to be constant and fixed by the concentration of Y^{3+}.

A similar behavior was observed by Rotman and Tuller in their studies of the electrical properties of YIG-YAG ($Y_3Fe_5O_{12}$-$Y_3Al_5O_{12}$) solid solutions.[63] For low iron contents ($\approx 1\%$), a p-type regime at high $p(O_2)$ was observed, followed by a plateau which was identified as ionic in nature with high activation energies (*ca.* 2 eV). Heavily doped YAG (10%) showed radically different dependencies on oxygen partial pressures. They observed that the conductivity went through a maximum with decreasing partial pressure, similar to our results in the $Sr_3Ti_{2-x}Mn_xO_{7-\delta}$ system. The maximum shifted to higher $p(O_2)$ with increasing temperature. The behavior was attributed to the formation of an iron defect band. The transition metal was being reduced from +4 to +3 with decreasing oxygen partial pressure, and the maximum in conductivity was assigned to the point at which the oxidation state of iron was 3.5.

With the above examples in mind, it is hard to imagine that the plateau we observe at high $p(O_2)$'s in the Mn-doped system is due to ionic conductivity, since, unlike the case of the $(ZrO_2$-$CeO_2)_{0.9}$-$(Y_2O_3)_{0.1}$ solid solution, the concentration of oxygen vacancies is not fixed by an additional dopant. Furthermore, if we assign the maximum in conductivity to the point where the average oxidation state of Mn is 3.5, then the concentration of defects is governed by the dependencies of region III in Figure 3.3. Therefore, region IV, where the concentration of oxygen vacancies is constant, cannot correspond to the nearly $p(O_2)$-independent regime. Instead, it could

correspond to region II, where the concentration of holes is constant. The slight increase in conductivity as oxygen partial pressure is decreased may be due to the formation of a Mn defect band, its contribution to the conductivity being given by the number of charge carriers in the band. As previously explained, this conductivity reaches a maximum at the point where the concentrations of Mn^{4+} and Mn^{3+} are equal. Figure 6.2 shows this model as the sum of contributions of holes and electrons (from the Mn band), which result in the profile exhibited by our Mn-doped materials. The fit of the model to the data is also shown in the figure. The data for $Sr_3Ti_{1.5}Mn_{0.5}O_{7-\delta}$ gives a better fit to the model than that for $Sr_3TiMnO_{7-\delta}$. While carrying out the fitting process, we noticed that it was hard to fit the region at high $p(O_2)$ successfully, especially for $Sr_3TiMnO_{7-\delta}$. This questions the origin of the contribution of the hole conductivity while, at the same time, the fit is worse without this contribution. The mobilities in the conduction band were 7.5×10^{-6} and 8.7×10^{-5} cm^2/Vs for $Sr_3Ti_{1.5}Mn_{0.5}O_{7-\delta}$ and $Sr_3TiMnO_{7-\delta}$, respectively. These values are close to those obtained in the heavily Fe-doped YAG (10%) system.

Figure 6.1. Dependence of hopping conductivity in a defect band on the oxidation state of

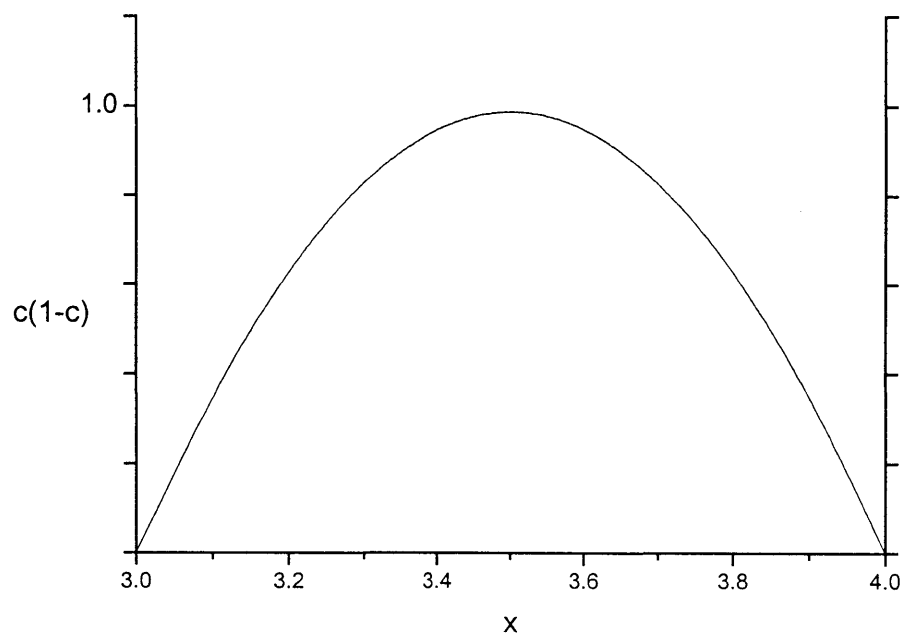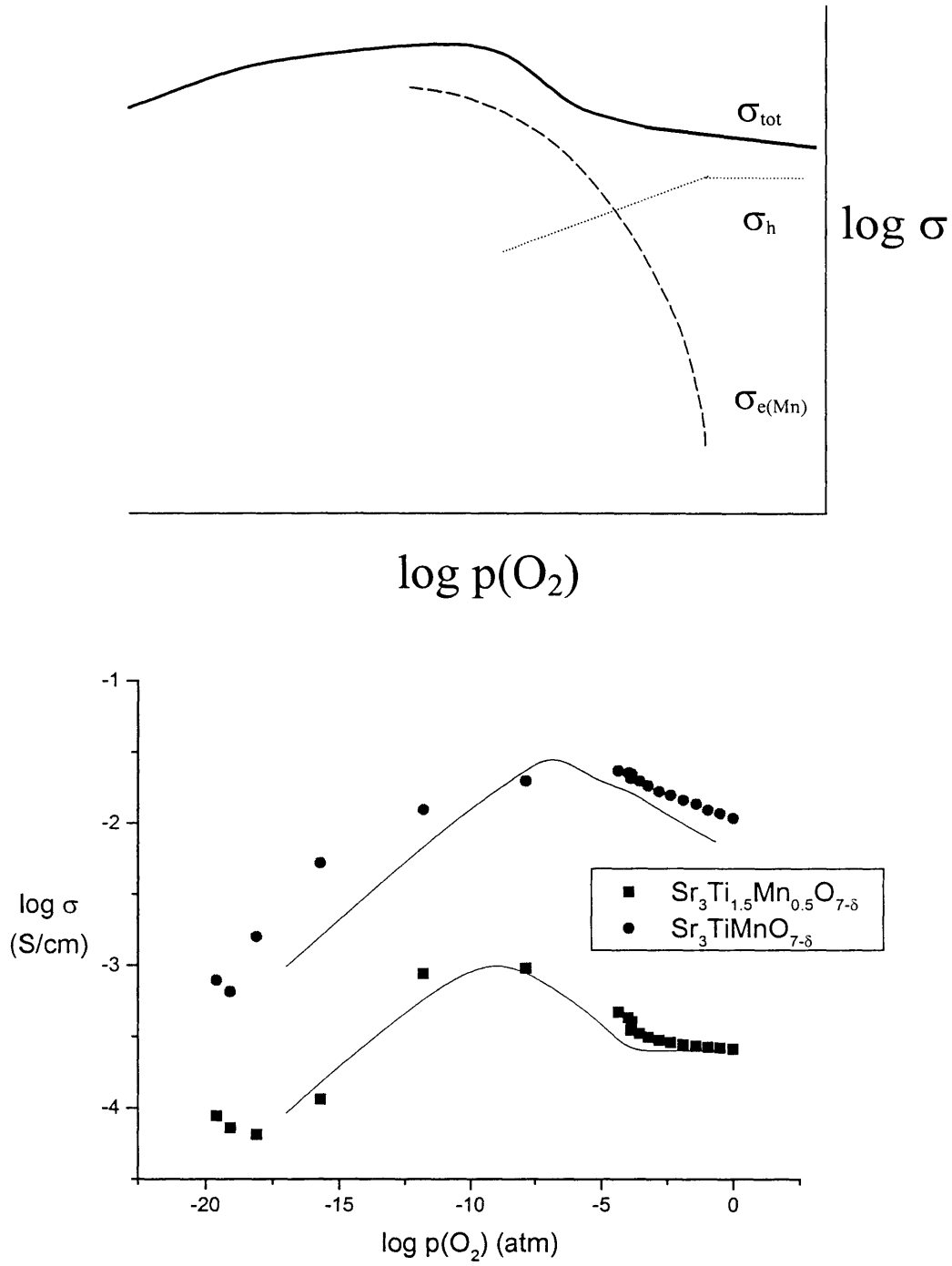$\mathbf{M^{x+}}$

Figure 6.2. Model for the dependence of conductivity of the $Sr_3Ti_{2-x}Mn_xO_{7-\delta}$ solid solutions on $p(O_2)$ (above); fit of the model to the data (below)

6.4. Modeling of the electrical conductivity in $Sr_3Ti_{2-x}M_xO_{7-\delta}$ (M=Al, Ga, Co, Fe, Mn) solid solutions

The dependence of conductivity on oxygen partial pressure in the $Sr_3Ti_{2-x}M_xO_{7-\delta}$ (M=Co, Fe, Mn) solid solution systems offers very different profiles depending on the identity of the dopant cation. When M= Al, Ga, Co and Fe, a p-type region of decreasing conductivity with decreasing $p(O_2)$ is followed by a plateau, which we believe is due to ionic conductivity. Good levels of ionic conductivity (3.3×10^{-2} S/cm at 700 °C for $Sr_3Ti_{1.2}Co_{0.8}O_{7-\delta}$) and ionic activation energy (0.64 eV for $Sr_3Ti_{1.8}Co_{0.2}O_{7-\delta}$) are observed for the transition metal systems. In the case of Mn, however, the conductivity increases slightly as the oxygen partial pressure decreases, reaches a maximum and then decreases again.

In all cases, except that of Mn, the defect models derived in Chapter 3 are very effective in deconvoluting the electrical conductivity data, identifying the charge carriers that predominate in each of the observed regimes and explaining most of the trends. We should recall that these models assume that the various defects present within the material are isolated and, for the most part, do not form defect bands. This assumption implies that the p-type and n-type electronic conduction processes take place in the valence and conduction bands, respectively. The origin of these conduction processes is shown in Figures 6.3-6.6 for fixed and variable valent dopants in different electroneutrality regimes.

We first discuss the cases involving a fixed valent dopant. The origin of the oxidation and reduction processes that give rise to p-type and n-type conductivity are shown, respectively, in Figures 6.3-6.4. At high $p(O_2)$, the oxidation reduction may be written as

$$\tfrac{1}{2}O_2(g) + V_O^{\cdot\cdot} \leftrightarrow O_o^x + 2h^\cdot \tag{6.6}$$

which implies that the insertion of oxygen ions into the lattice produces holes. Depletion of oxygen vacancies has to be accompanied by an increase in oxygen interstitials, according to the Frenkel equilibrium

$$O_o^x \leftrightarrow O_i'' + V_o^{\cdot\cdot} \tag{6.7}$$

while the increase in hole concentration is offset by a concomitant decrease in electron concentration given by

$$0 \leftrightarrow e' + h^{\cdot} \tag{6.8}$$

Taking these equilibria into account, equation 6.5 may be rewritten as

$$\frac{1}{2}O_2(g) \leftrightarrow O_i'' + 2h^{\cdot} \tag{6.9}$$

which is the form shown in Figure 6.3. Consequently, the promotion of electrons from the top of the valence band to form interstitials results in the formation of positive holes, which account for the predominant conduction process. At lower p(O_2)'s, the reduction process may be expressed by

$$O_o^x \leftrightarrow V_o^{\cdot\cdot} + \frac{1}{2}O_2(g) + 2e' \tag{6.10}$$

which implies that electrons are donated or promoted from the oxygen vacancies to the conduction band. The transport of these electrons corresponds to the n-type conductivity observed under reducing conditions (Figure 6.4).

The situation in which a transition metal dopant is introduced into the host structure is depicted in Figures 6.5-6.6. We assume that the energy levels of the d orbitals (the low-energy t_{2g} set) are within the band gap. We would expect this to be the case, since the effective nuclear charge in Co^{4+} is higher than in Ti^{4+} and will cause electrons to be more tightly held, as evidenced by their respective ionic radii. Co then acts as an acceptor, being able to undergo

201

reduction. The beginning of this process is depicted in Figure 6.5, which shows how electrons from the top of the valence band are promoted to the Co energy levels. As in the oxidation process depicted previously, holes are left behind in the valence band and are responsible for the p-type conductivity observed. This is the situation in region III, the main assumption being that $[Co_{tot}] = [Co_{Ti}^x]$, i.e. most of the Co ions remain in the +4 oxidation state.

In contrast, the reduction process continues in region IV via a different mechanism, shown in Figure 6.6. Continued reduction of Co from +4 to +3 is accompanied by the formation of oxygen vacancies. Thus, the electroneutrality equation of interest here is $2[V_o^{\cdot\cdot}] = [Co_{Ti}']$, and $[Co_{tot}] = [Co_{Ti}']$, i.e. most of the Co ions are in the +3 oxidation state. Again, it is critical to note that, in this case, the Co d orbitals are assumed to be isolated, thus not allowing transport processes, such as hopping-type electronic conduction, to take place.

The case of Mn, however, is significantly different from the rest. As was demonstrated earlier, the conductivity is explained by taking into account the formation of a Mn defect band within the bandgap of $Sr_3Ti_2O_7$. The situation is depicted in more detail in Figure 6.7. Presumably, at very low concentrations of Mn, the energy levels are isolated; as this concentration is increased, band formation ensues. Promotion of electrons to this band from the reduction process lead to the electronic conduction process which was observed in our studies.

What we then have is a system of solid solutions, $Sr_3Ti_{2-x}M_xO_{7-\delta}$, M=Co, Fe, Mn, where the identity of the transition metal has a drastic effect on the electrical conductivity of the material. Our studies suggest that, for the cases of Co and Fe, the interaction between cation d orbitals is insufficient to form impurity bands; however, addition of Mn necessitates invoking the presence of a defect band in order to assign the conductivity data.

In general, electron localization increases in the first row transition metals from left to right, and the trend in conductivity agrees with this generalization. This is due to the increase in effective nuclear charge in later first row transition metals, which causes electrons to be more tightly held and ionic radii to increase for a given oxidation state. On the other hand, the Mn-containing system displays the lowest cell parameters, indicating smaller M-O bond distances and suggesting the opposite trend. One way to justify this observation is to reason that at high temperatures, and as the oxygen partial pressure decreases, the oxidation states of the transition metals used herein are decreasing, whereas the structural data obtained at room temperature were obtained for slow cooled samples in air. This circumstance increases the chances of obtaining more highly oxidized cations. In this respect, we point out that ionic radii data for the +3 oxidation state in the octahedral coordination of the perovskite structure follow the expected trend, i.e.

$$r(Mn^{3+}) > r(Fe^{3+}) > r(Co^{3+})$$

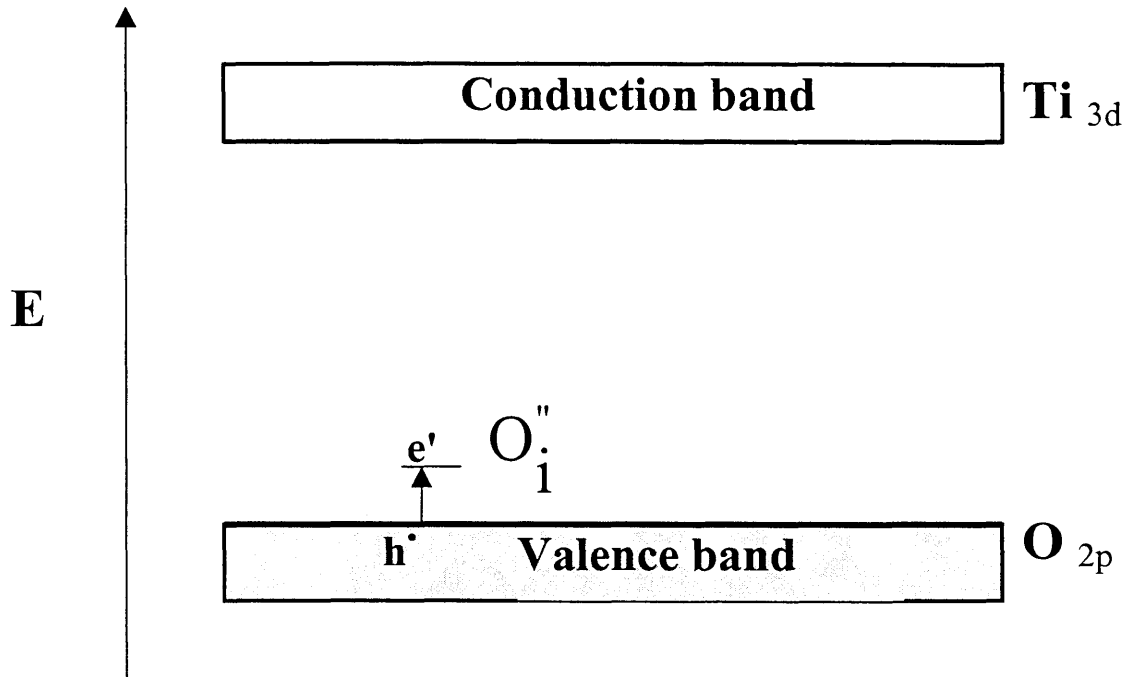$$0.58 \text{ Å} > 0.55 \text{ Å} > 0.545 \text{ Å}$$

assuming low spin states for all cations.[2] In air, at elevated temperatures, we know from the titration measurements that Co has an average oxidation state of 3.75. Since Co^{4+} should reduce more readily than Fe^{4+}, we would expect the Fe-containing system to exhibit an oxidation state between 3.75 and 4 under the same conditions. For Mn, this trend should be more pronounced. Supporting this idea is the fact that Mn does not achieve an oxidation state of 3.5 until 10^{-5}-10^{-7} atm, whereas Co achieves this at about 10^{-3} atm (see Figures 5.23 and 5.25). Presumably, the $p(O_2)$ at which Fe attains this midpoint in reduction is somewhere in between. Hence, while partial reduction of the transition metal cations at high temperatures may account for a slight increase in ionic radii, this reduction process will be more dominant in Co than in Fe than in Mn,

so that the trend in ionic radii seen above is not followed under the same conditions of temperature and oxygen partial pressure. Consequently, the differences in ionic size between these cations should be minimal. Thus, it seems surprising that such a small difference in size results in the formation of a defect band in the Mn compounds whereas Co and Fe compounds do not exhibit such a degree of orbital overlap. A final point that should be made here is that ionic radii data, as reported by Shannon and Prewitt, are entirely empirical, and should therefore be used with caution. Hence, if we did not have such data available, we probably would predict a higher localization of d electrons in the latter first row transition metal cations, which agrees with our results.

Inconsistencies in trends of this kind have been reported for other related perovskites of general formula $La_{1-x}Sr_xMO_{3-\delta}$, M=Cr, Mn, Fe, Co.[64] For M=Cr, Fe, an isolated point defect scheme proved successful in explaining the conductivity data. In the case of Fe, for example, a p-type region of decreasing conductivity with decreasing partial pressure at high $p(O_2)$ was followed by an n-type regime of increasing conductivity. The transition between these two regions moved towards more oxidizing atmospheres as the temperature was increased. The equilibrium of Fe between its oxidation state of +4 to +3 was also taken into account.[30] However, for M=Mn, Co, the use of such a model was less satisfactory. In the case of Co, high levels of electronic conductivity were observed, attributed to itinerant behavior of the electronic charge carriers. The metallic type behavior in this compound leads to an empirical model which, besides considering the normal defect equilibria, also accounts for defect band formation.[29, 64] The high levels of electronic conductivity found in the case of M = Mn have also been explained on a similar basis.[34]

Even though an empirical model has been shown to successfully interpret the electrical conductivity and nonstoichiometry data, the question of why Mn and Co behave in one manner while Fe and Cr behave in a different way, remains largely unanswered. Where one would normally expect to see a trend in terms of the degree of localization of the d electrons across the first row of the transition metals, that has not necessarily been the case in these perovskite materials.

Figure 6.3. Schematic energy diagram in the case of a fixed valent dopant at high p(O$_2$)

$$E$$

Conduction band	**Ti** $_{3d}$

$$\underset{1}{O_i''} \quad \underline{e'}$$

h$^\bullet$ **Valence band**	**O** $_{2p}$

Equilibrium:

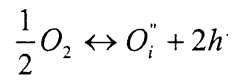$$\frac{1}{2}O_2 \leftrightarrow O_i'' + 2h^\bullet$$

Figure 6.4. Schematic energy diagram in the case of fixed valent dopant at low p(O$_2$)

Equilibrium:

$$O_o^x \leftrightarrow \frac{1}{2}O_2 + V_o^{\cdot\cdot} + 2e'$$
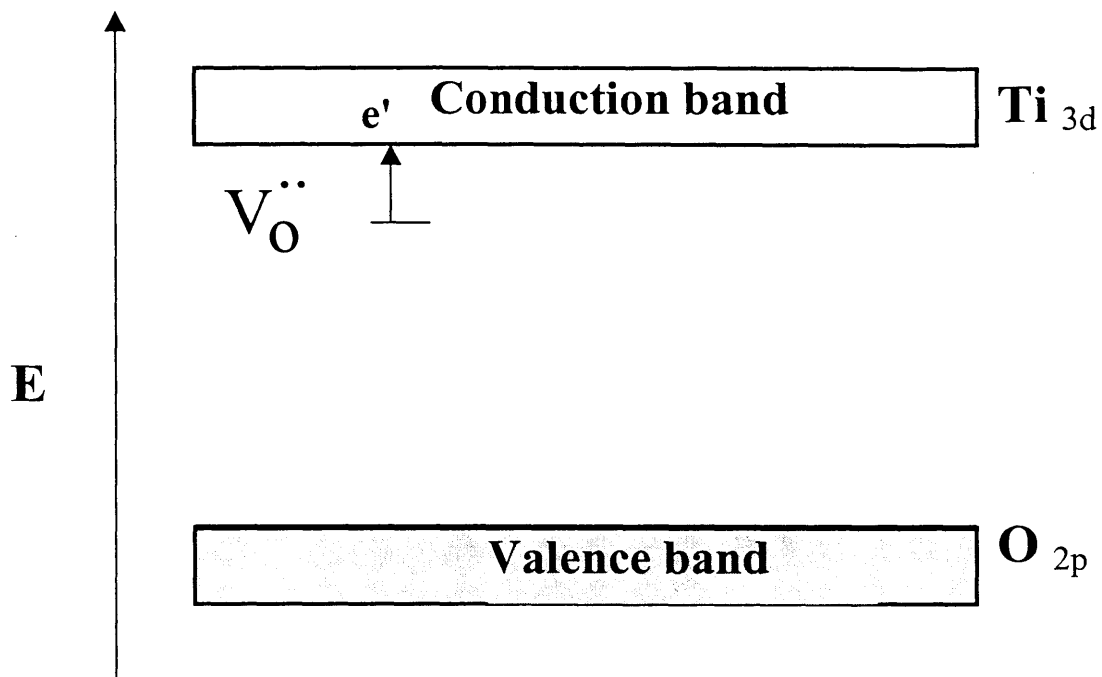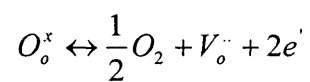
Figure 6.5. Schematic energy diagram in the case of fixed valent dopants such as Co, Fe at high p(O₂)
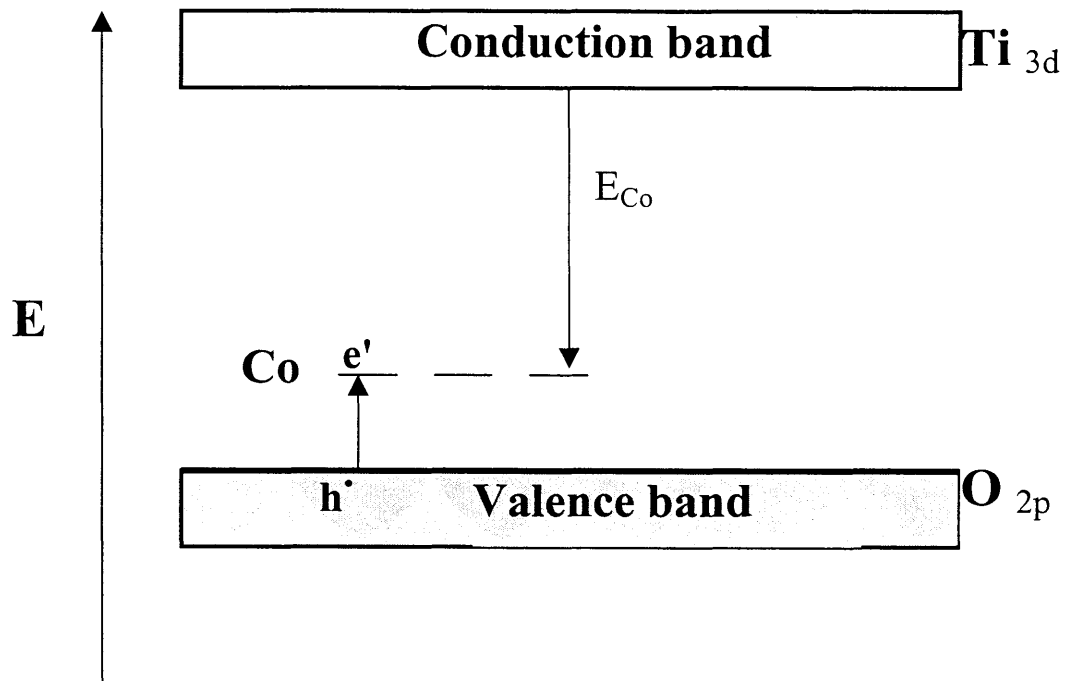
Region III

$$p = [Co'_{Ti}]$$

$$[Co_{tot}] = [Co^x_{Ti}]$$

Figure 6.6. Schematic energy diagram in the case of fixed valent dopants such as Co, Fe at intermediate $p(O_2)$
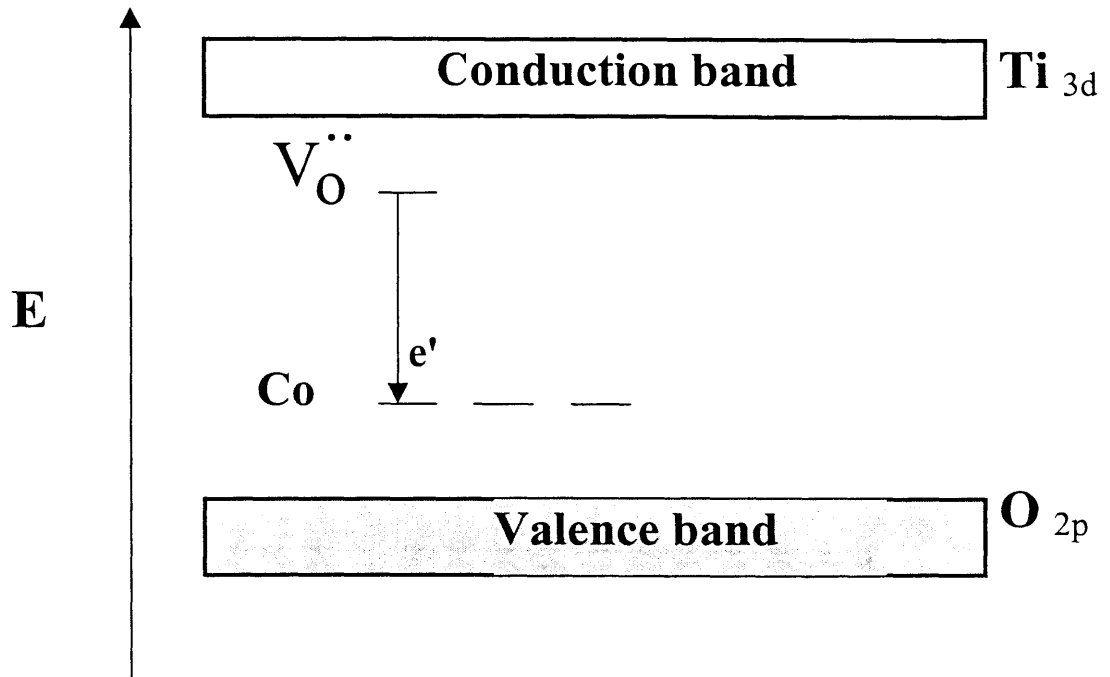
Region IV

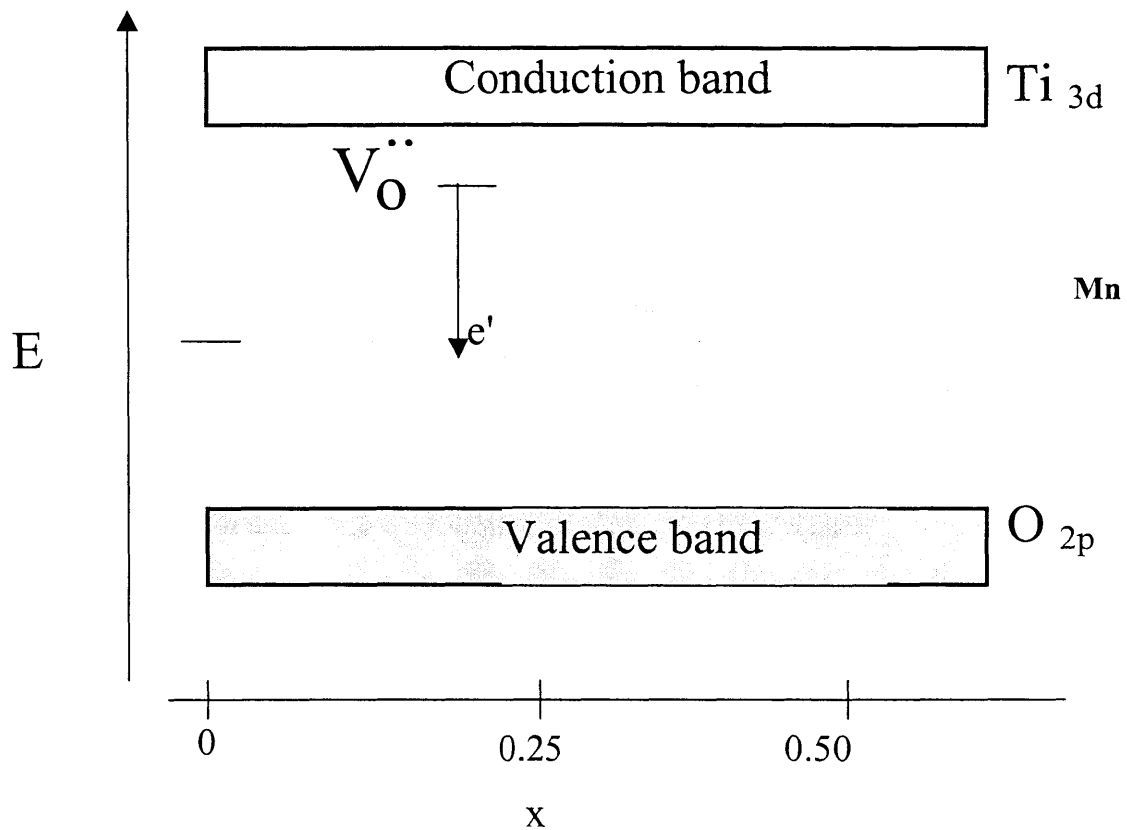$$2[V_o^{\cdot\cdot}] = [Co_{Ti}^{'}]$$

$$[Co_{tot}] = [Co_{Ti}^{'}]$$

Figure 6.7. Schematic band diagram in the $Sr_3Ti_{2-x}Mn_xO_{7-\delta}$ solid solution. Redrawn after

Sprague[65]

References

1. Ruddlesden, S. N. and Popper, P., *Acta Cryst.*, **1958**, *11*, 54-55.

2. Shannon, R. D., *Acta Cryst.*, **1976**, *A32*, 751-767.

3. Elcombe, M. M., Kisi, E. H., Hawkins, K. D., White, T. J., Goodman, P. and Matheson, S., *Acta Cryst. B*, **1991**, *47*, 305-314.

4. Sarjeant, G. M., Greenwood, K. B., Poeppelmeier, K. R., Zhang, H., Salvador, P. A., Mason, T. O. and Marks, L. D., *Chem. Mater.*, **1996**, *8*, 2792-2798.

5. Dann, S. E. and Weller, M. T., *J. Solid State Chem.*, **1995**, *115*, 499-507.

6. Dann, S. E., Weller, M. T. and Currie, D. B., *J. Solid State Chem.*, **1992**, *97*, 179-185.

7. Mizutani, N., Kitazawa, A., Okuma, N. and Kato, M., *J. Chem. Soc. (Japan) Ind. Ed.*, **1970**, *73*, 1097-1103.

8. Kafalas and Longo, *J. Solid State Chem.*, **1972**, *4*, 55.

9. Subramanian, M. A., Crawford, M. K. and Harlow, R. L., *Mater. Res. Bull.*, **1994**, *29*, 645-650.

10. Cao, G., McCall, S. and Crow, J. E., *Phys. Rev. B*, **1997**, *55*, R672-675.

11. Anderson, M. T., Vaughey, J. T. and Poeppelmeier, K. R., *Chem. Mater.*, **1993**, *5*, 151-165.

12. Sirazhidinov, A., *Russ. J. Inorg. Chem. (Engl. Transl.)*, **1971**, *16*, 40.

13. *Nat. Bureau Standards Mono.*, **1972**, *25*, 52.

14. Brisi and Montorsi, *Atti Accad. Scienze Torino*, **1966-67**, *101*, 391.

15. Takeda, Y., Kanno, K., Takada, T., Yamamoto, O., Takano, M., Nakayama, N. and Bando, Y., *J. Solid State Chem.,* **1986**, *63*, 237-249.

16. Bezdicka, P., Wattiaux, A., Grenier, J. C., Pouchard, M. and Hagenmuller, P., *Z. anorg. allg. Chem.,* **1993**, *619*, 7-12.

17. Taguchi, H., Shimada, M. and Koizumi, M., *J. Solid State Chem.,* **1979**, *29*, 221-225.

18. Yoshiasa, A., Inoue, Y., Kanamaru, F. and Koto, K., *J. Solid State Chem.,* **1990**, *86*, 75-81.

19. Kharton, V. V., Shuangbao, L., Kovalevsky, A. V. and Naumovich, E. N., *Solid State Ionics,* **1997**, *96*, 141-151.

20. Kharton, V. V., Shuangbao, L., Kovalevsky, A. V., Viskup, A. P., Naumovich, E. N. and Tonoyan, A. A., *Mater. Chem. Phys.,* **1998**, *53*, 6-12.

21. Shaplygin, I. S. and Lazarev, V. B., *Russ. J. Inorg. Chem.,* **1985**, *30*, 1828-1829.

22. Taguchi, H., Takeda, Y., Janamaru, F., Shimada, M. and Koizumi, M., *Acta Cryst.,* **1977**, *B33*, 1299-1301.

23. Mattausch, v. H. and Muller-Buschaum, H., *Z. anorg. allg. Chem.,* **1971**, *386*, 1-14.

24. Jansen, V. M. and Hoppe, R., *Z. Anorg. Allg. Chem.,* **1973**, *398*, 54-62.

25. Jansen, V. M. and Hoppe, R., *Z. Anorg. Allg. Chem.,* **1974**, *408*, 75-82.

26. Jansen, V. M. and Hoppe, R., *Z. Anorg. Allg. Chem.,* **1974**, *409*, 152-162.

27. Sunstrom, J. E. I., Ramanujachary, K. V., Greenblatt, M. and Croft, M., *J. Solid State Chem.,* **1998**, *139*, 388-397.

28. Petrov, A. N., Kononchuk, O. F., Andreev, A. V., Cherepanov, V. A. and Kofstad, P., *Solid State Ionics,* **1995**, *80*, 189-199.

29. Mizusaki, J., Mima, Y., Yamauchi, S., Fueki, K. and Tagawa, H., *J. Solid State Chem.,* **1989**, *80*, 102-111.

30. Mizusaki, J., Sasamoto, T., Cannon, W. R. and Bowen, H. K., *J. Amer. Ceram. Soc.,* **1983**, *66*, 247-252.

31. Wattiaux, A., Fournes, L., Demourgues, A., Bernaben, N., Grenier, J. C. and Pouchard, M., *Solid State Commun.,* **1991**, *77*, 489.

32. Negas, T. and Roth, R. S., *J. Solid State Chem.,* **1970**, *1*, 409-418.

33. Mizusaki, J., Tagawa, H., Naraya, K. and Sasamoto, T., *Solid State Ionics,* **1991**, *49*, 111-118.

34. Yasuda, I. and Hishinuma, M., *J. Solid State Chem.,* **1996**, *123*, 382-390.

35. Kinoshita, K., Izumi, F., Yamada, T. and Asano, H., *Phys. Rev.,* **1992**, *B45*, 5558-5562.

36. Turrillas, X., Sellars, A. P. and Steele, B. C. H., *Solid State Ionics,* **1988**, *28-30*, 465-469.

37. Goodenough, J. B., Ruiz-Diaz, J. E. and Zhen, Y. S., *Solid State Ionics,* **1990**, *44*, 21-31.

38. Kendall, K. R., Thomas, J. K. and zur Loye, H. C., *Chem. Mater.,* **1995**, *7*, 50-57.

39. Tuller, H. L., *Solid State Ionics,* **1992**, *52*, 135-146.

40. Spears, M. A. and Tuller, H. L., *Application of defect modeling to materials design*, (Materials Research Society, Boston, 1995), Vol. 369, pp. 271-288.

41. Moon, P. K. and Tuller, H. L., *Solid State Ionics,* **1988**, *28-30*, 470-474.

42. Hawkins, K. and White, T. J., *Trans. R. Soc. London,* **1991**, *A336*, 541-569.

43. Kilner, J. A., *The role of dopant size in determining oxygen ion conductivity in the fluorite structure oxides*, R. Metselaar, H. J. M. Heijligers and J. Schoonman, Eds., (Elsevier Scientific Publishing Company, Studies in Inorganic Chemistry, Veldhoven, The Netherlands, 1982), Vol. 3, pp. 189-192.

44. Wang, D. Y., Park, D. S., Griffith, J. and Nowick, A. S., *Solid State Ionics,* **1981**, *2*, 95-105.

45. Choi, G. M. and Tuller, H. L., *J. Am. Ceram. Soc.,* **1988**, *71*, 201-205.

46. Moon, P. K., Ph.D. Thesis, Massachusetts Institute of Technology, 1988

47. Kudo, T. and Fueki, K., in *Solid State Ionics,* Eds. (VCH and Kondansha, 1990), pp. 133.

48. Etsell, T. H. and Flengas, S. N., *Chem. Rev.,* **1970**, *70*, 339-376.

49. Van Doorn, R. H. E., Kruidorf, H., Bouwmeester, H. J. M. and Burggraaf, A. J., *Oxygen permeability of strontium-doped LaCoO$_{3-\delta}$ perovskites*, G.-A. Nazri, J.-M. Tarascon and M. S. Schreiber, Eds., (Materials Research Society, Solid State Ionics IV, Boston, 1995), Vol. 369, pp. 377-382.

50. Sammells, A. F., Cook, R. L., White, J. H. and Osborne, J. J., *Solid State Ionics,* **1992**, *52*, 111-123.

51. Kilner, J. A., *Bol. Soc. Esp. Ceram. Vidrio,* **1998**, *37*, 247-255.

52. Mizusaki, J., *Solid State Ionics,* **1992**, *52*, 79-91.

53. Yasuda, I. and Hikita, T., *J. Electrochem. Soc.,* **1994**, *141*, 1268-1273.

54. Denk, I., Munch, W. and Maier, J., *J. Am. Ceram. Soc.,* **1995**, *78*, 3265-3272.

55. Denk, I., Claus, J. and Maier, J., *J. Electrochem. Soc.,* **1997**, *144*, 3526-3536.

56. Denk, I., Noll, F. and Maier, J., *J. Am. Ceram. Soc.,* **1997**, *80*, 279-285.

57. Steinsvik, S., Bugge, R., Gjonnes, J., Tafto, J. and Norby, T., *J. Phys. Chem. Solids,* **1997**, *58*, 969-976.

58. Sutija, D. P., Norby, T., Osborg, P. A. and Kofstad, P., *AC van der Pauw measurements of the electrical conductivity of iron-doped calcium titanate,* S. C. Singhal, Eds., (The Electrochemical Society, 3rd International Symposium on Solid Oxide Fuel Cells, 1993), Vol. 93-4, pp. 552-561.

59. Cales, B. and Baumard, J. F., *Rev. Int. Hautes Temper. Refract.,* **1980**, *17*, 137-147.

60. Cales, B. and Baumard, J. F., *J. Electrochem. Soc.,* **1984**, *131*, 2407-2413.

61. Porat, O., Spears, M. A., Heremans, C., Kosacki, I. and Tuller, H. L., *Solid State Ionics,* **1996**, *86-88*, 285-288.

62. Tuller, H. L. and Nowick, A. s., *J. Phys. Chem. Solids,* **1977**, *38*, 859-867.

63. Rotman, S. R. and Tuller, H. L., *J. Electroceram.,* **1998**, *2*, 95-104.

64. Bouwmeester, H. J. M. and Burggraaf, A. J., Dense ceramic membranes for oxygen separation, in *The CRC Handbook of Solid State Electrochemistry,* P. J. Gellings and H. J. M. Bouwmeester, Eds. (CRC Press, Boca Raton, 1997), pp. 481-553.

65. Sprague, J. J., Ph.D. Thesis, Massachusetts Institute of Technology, 1999, p. 211.

Chapter 7. Conclusions

We have synthesized, studied and characterized the electrical properties of a new series of doped layered perovskites, of general formula $Sr_3Ti_{2-x}M_xO_{7-\delta}$, M= Al, Ga, In, Co, Fe, Mn. These novel compounds were synthesized in order to investigate the effect of doping on the magnitude of the ionic and electronic conductivity as well as to evaluate their potential use in applications such Solid Oxide Fuel Cells and oxygen sensors.

7.1. Doping with fixed valent cations

Substitution of fixed valent cations such as Ga^{3+}, Al^{3+} and In^{3+} reaches a solubility limit at about 1/8 of the Ti sites in the perovskite regions of the structure. Measurements of the total electrical conductivity as a function of temperature in air reveal an increase of about one order of magnitude with respect to the parent stoichiometric phase. Additional measurements of the conductivity as a function of oxygen partial pressure show that, at high $p(O_2)$'s, the conductivity is predominantly p-type with activation energies of about 0.9 eV. At $p(O_2) < 10^{-5}$ atm, an electrolytic regime independent of partial pressure is observed, characterized by a relatively low magnitude of conductivity (*ca.* 10^{-6} S/cm at 700 °C) and high ionic migration energies (*ca.* 1.5 eV). At very low partial pressures of oxygen, a regime of increasing conductivity with decreasing $p(O_2)$ indicates n-type electronic conductivity. The width of the electrolytic regime shrinks with increasing temperature. This behavior may be explained by a simple defect model defined by the electroneutrality equation $2[V_o^{\cdot\cdot}] = [N_{Ti}']$. The model allows us to extract the enthalpies of

oxidation (1.5-2.0 eV) and reduction (4.8-6.2 eV), as well as the thermal bandgap (3.2-3.9 eV). Our values are in good agreement with those found for other titanate systems.

The electrical properties of these materials indicate that doping with fixed valent cations results in new materials which show a small improvement of the ionic conductivity over that of the undoped material. Consequently, this family of Ruddlesden-Popper phases shows little promise for use in industrial applications such as Solid Oxide Fuel Cells or oxygen sensors.

7.2. Doping with transition metal cations

The electrical conductivity was also studied as a function of oxygen partial pressure and, for M=Co, Fe, presented a similar profile to that shown by the fixed valent-doped materials. At $p(O_2) > 10^{-5}$ atm, a region of p-type conductivity is observed, followed by an apparent electrolytic regime at lower $p(O_2)$'s, which displays high conductivities ($>10^{-2}$ S/cm at 700 °C for $Sr_3Ti_{1.2}Co_{0.8}O_{7-\delta}$) and low activation energies (0.66 eV for $Sr_3Ti_{1.8}Co_{0.2}O_{7-\delta}$). With increasing Co content, the conductivity shows a significant increase, while the thermodynamic stability of the materials at reduced $p(O_2)$ appears to decrease. Iodometric titration measurements appear to confirm the identity of the electrolytic regime by comparison with an isolated defect model. Independent measurements of the chemical diffusion coefficient in a Co-doped sample (*ca.* 10^{-6} cm^2sec^{-1} at 700 °C) also suggest that this domain is indeed ionic in nature. For M= Fe, an increase in Fe content is not accompanied by an increase in conductivity. However, because of the similarity in profiles, the same assignments for the different conductivity regimes are attributed to the Fe-containing materials.

The Co-containing system was shown to be highly oxidized, with Co showing an average oxidation state of 3.75 in air at 700 °C, while Co(IV) was predominant at room temperature. This result is somewhat surprising in light of our synthetic procedure in air; other Co(IV)-containing materials are typically synthesized under more oxidizing conditions.

The electrical conductivity of the $Sr_3Ti_{2-x}M_xO_{7-\delta}$, M=Co, Fe, system was explained with a simple defect model assuming isolated defects, and no defect band formation. In contrast, such a defect band formation was shown to play an important factor in explaining the electrical conductivity of the $Sr_3Ti_{2-x}Mn_xO_{7-\delta}$ solid solution. With decreasing $p(O_2)$, the conductivity first shows an increase, reaches a maximum and then slowly decreases.

The behavior of the $Sr_3Ti_{2-x}M_xO_{7-\delta}$, M=Co, Fe, solid solution shows a significant enhancement of what is believed to be ionic conductivity with respect to the fixed valent-doped compounds. High levels of oxygen ion conductivity at intermediate $p(O_2)$'s are observed, while the materials are shown to be mixed ionic and electronic conductors in air. Further studies are needed to determine conclusively the identity of the ionic domain and the feasibility of these materials in an actual application, although it is expected that their behavior will not be superior to that exhibited by their three-dimensional perovskite counterparts.

In this respect, one aspect that could be of importance is the stability of the Co-doped materials. While their electrical properties deserve further attention, our results show that improved performance may be possible at higher Co concentrations. Assuming that the levels of ionic and electronic conduction become appropriate, if these materials show good compatibility with respect to other SOFC components (i.e. electrolyte), the possibility exists for these materials to play an important role in these devices.

In this respect, we recall that current state-of-the-art SOFCs use YSZ as the electrolyte. Both $La_{1-x}Sr_xCoO_{3-\delta}$ and $La_{1-x}Sr_xMnO_{3-\delta}$ have been shown to react with YSZ, although the reaction is more facile with the cobaltite material. Therefore, $La_{1-x}Sr_xMnO_{3-\delta}$ is the material of choice in current SOFCs, even though the magnitude of the ionic conductivity is not as high. In order for the Ruddlesden-Popper phases to replace this material, they should therefore show appropriate thermal expansion coefficients and no detrimental side reactions with respect to the electrolyte with which it would be in contact at the temperature of operation.

Chapter 8. Future Work

The research which we have presented in this thesis was pursued in order to improve our understanding of the basic properties of these materials, such as electrical conductivity and nonstoichiometry, and how they affect each other. In this respect, our investigations have produced interesting results. The use of fixed valent cations as dopants was shown to result in materials with low magnitudes of conductivity, and our studies indicate that improving these properties should not be a priority in the future. On the other hand, substitution of transition metals into the Ti^{4+} site has been shown to greatly improve the electrical properties, achieving good levels of ionic conductivity and intermediate partial pressures of oxygen. We believe that this family of materials deserves further attention, and suggest the following areas:

1) Further study of the $Sr_3Ti_{2-x}Co_xO_{7-\delta}$ solid solution. Given the observed trend in conductivity with increasing Co concentration, materials with higher values of x should be synthesized and the electrical conductivity of the resulting compounds studied. Because of the levels of conductivity already measured, it is anticipated that 4-probe techniques will be needed. The existence of both $Sr_3Co_2O_y$ ($y\approx6$) and $Sr_3Ti_{1.2}Co_{0.8}O_7$ in air has been reported. With increasing values of x, we expect to see at some point that Co will take on oxidation states between 3 and 4, while the concentration of oxygen vacancies should increase. This shift in the compensation mechanism should result in an increase in the oxygen ion conductivity of these materials. In order to monitor the oxygen nonstoichiometry, the method of iodometric titration has proved successful and should be used in the future.

221

2) Along the same lines, the presence of the electrolytic regime at intermediate $p(O_2)$ in the $Sr_3Ti_{2-x}Co_xO_{7-\delta}$ solid solution should be confirmed through independent measurements. Other ways to measure the chemical diffusion coefficient are available, and would serve to confirm the result obtained through our experiments.

3) Provided that the $Sr_3Ti_{2-x}Co_xO_{7-\delta}$ system is shown to exhibit good levels of ionic and mixed ionic and electronic conductivity, the materials should be tested as a SOFC electrode in an actual cell and their performance evaluated. Likewise, the feasibility of these materials for use in partial oxidation membranes should be studied.

4) The presence of Co(IV) in air should be pursued through magnetic studies. To begin with, and as pointed out in previous chapters, Co(IV) compounds are rare. The study of the magnetic properties in layered compounds, where one may vary the concentration of Co(IV) (at least up to 40% of the sites), is of interest. Assuming an electronic configuration of $t_{2g}^5 e_g^0$, an unpaired electron exists in the degenerate low-energy orbital set. Since the Co-Co distance is too large for direct bonding, any exchange must take place through the O_{2p} orbitals. Given that in the ideal perovskite structure the Co-O-Co angle is 180°, the exchange is expected to be antiferromagnetic in nature. The strength of the interaction is expected to increase with increasing cobalt concentration, as the number of nearest Co neighbors increases. Because the concentration of Co may be altered in this manner, the system may be induced to shift from a 1-D to a 2-D -type behavior.

5) While we have restricted ourselves to $n=2$ Ruddlesden-Popper phases, other values of n should also be explored. As we mentioned before, solid solutions between the titanates and the other transition metals should be explored, while introduction of cations such as Ga^{3+} and Al^{3+} may not be worthwhile. We suggest the study of $n= 1, 3, \infty$ systems in order to elucidate

222

the effect of the SrO layers on the electrical properties of the materials. Furthermore, the presence of highly oxidized cations (Co^{4+}, Fe^{4+}) after synthesis in air may be correlated to this structural factor, since perovskite ($n=\infty$) materials necessitate special synthetic procedures in order to exhibit highly oxidized transition metal cations.

6) Another subject that should be further studied is that of defect band formation in the Mn-containing solid solutions. At a basic level, it is of importance to understand the origin of electron delocalization in compounds which contain transition metal cations, as well as what factors are important in decreasing such a delocalization when the identity of the transition metal cation is altered. With this knowledge, it becomes easier for the researcher to alter the electrical properties of such materials, which is ultimately our goal.